

Frequency-Selective Surfaces for Microwave and Terahertz Spectra

by

Xiaojing LV

B. Sc. (Electronic Information Science and Technology),
Xidian University, China, 2010
M. Eng. (Signal and Information Processing),
The University of Adelaide, Australia, 2013

Thesis submitted for the degree of

Doctor of Philosophy

in

School of Electrical & Electronic Engineering
Faculty of Engineering, Computer & Mathematical Sciences
The University of Adelaide

2021

Supervisors:

Prof. Christophe Fumeaux, School of Electrical & Electronic Engineering

A.Prof. Withawat Withayachumnankul, School of Electrical & Electronic Engineering

To my beloved parents and grandparents.

Contents

Contents	v
Abstract	ix
Originality Declaration	xi
Acknowledgments	xiii
Thesis Conventions	xv
Abbreviation	xvii
List of Figures	xix
List of Tables	xxiii
Chapter 1. Introduction	1
1.1 Introduction	2
1.1.1 Frequency-Selective Surfaces: Definition and Applications	2
1.1.2 Research Motivations and Thesis Objectives	3
1.2 Statement of Original Contributions	6
1.3 Thesis Structure	8
Chapter 2. Background of Frequency Selective Surfaces	11
2.1 Introduction	12
2.2 Fundamental Theories and Techniques	12
2.2.1 Babinet’s Principle for Complementary FSSs	12
2.2.2 Scalability: from Physical Dimensions to Frequency Response	14
2.2.3 Equivalent Circuit Modeling of a Unit-Cell Geometry	14
2.2.4 Transmission Line Approach for Multilayer Structures	16
2.3 FSS-Inspired Circuit Analog Absorbers	22

2.3.1	Embedding Surface Resistance	23
2.3.2	Evaluation Criteria	25
2.3.3	Experimental Setup for Frequency Response Measurement	26
2.4	FSS-Inspired Reconfigurable Filters	29
2.5	Summary	34

Chapter 3. Single-FSS-Layer Absorber Adopting Impedance Matching Superstrate 37

3.1	Introduction	38
3.2	Absorber Design with Dielectric Superstrate	39
3.2.1	Equivalent Circuit Modeling and Full-wave Simulation	40
3.2.2	Impedance Matching Analysis	42
3.3	Experimental Validation and Comparison	45
3.4	Conclusion	50

Chapter 4. Fast Semi-Analytical Design Approach for Circuit-Analog Absorbers 51

4.1	Introduction	52
4.2	Semi-Analytical Design Approach	54
4.2.1	Equivalent Circuit Elements for Lossless FSS Patterns	55
4.2.2	Impact of Dielectric Substrate on Reactive Components	59
4.2.3	Impact of the Sheet Resistance	62
4.2.4	Absorber Assembly and Algorithm Validation	64
4.3	Global Optimization and Evaluation Criterion	65
4.4	Experimental Validation	68
4.4.1	Wideband Single-FSS-Layer Absorber Design	68
4.4.2	Fabrication and Measurement	69
4.5	Conclusion	72

Chapter 5. Terahertz Absorber with Sub-Skin-Depth Metal 75

5.1	Introduction	76
5.2	Metallic FSS-Based Terahertz Absorber	77
5.2.1	Equivalent Circuit Analysis and Synthesis	77

5.2.2	Surface Impedance of Sub-Skin-Depth Metals	79
5.2.3	Reliability Evaluation	80
5.3	Conclusion and Validation Progress	81
 Chapter 6. Mechanically Reconfigurable Terahertz Bandpass Filter		85
6.1	Introduction	86
6.2	Frequency Reconfigurable Bandpass Filter Design	87
6.3	Insights into Selectivity and Reconfigurability	90
6.3.1	Fabry-Perot Resonance Cavity	90
6.3.2	Impedance Matching with Smith Chart	92
6.4	Robustness and Reliability	95
6.4.1	Misalignment of Unit-Cell Patterns	95
6.4.2	Stability to Oblique Impinging Waves	97
6.5	Experimental Validation	97
6.5.1	FSS Fabrication and Filter Assembly	97
6.5.2	Equipment Setup and Measurement	100
6.6	Conclusion	102
 Chapter 7. Summary and Outlook		103
7.1	Circuit Analog Microwave Absorbers	104
7.1.1	Chapter 3: Absorber Adopting Impedance Matching Superstrate	104
7.1.2	Chapter 4: Design Approach for Circuit-Analog Absorbers	105
7.2	FSS-Based Structures for Terahertz Applications	106
7.2.1	Chapter 5: Terahertz Absorbers with Sub-Skin-Depth Metal . . .	106
7.2.2	Chapter 6: Mechanically Reconfigurable Terahertz Bandpass Filter	107
7.3	Concluding Remark	108
 Bibliography		111

Abstract

FREQUENCYselective surfaces (FSSs) made of subwavelength periodic structures have been broadly applied in various electromagnetic applications. Their main function is to tailor the frequency response to incident waves, or to obtain electromagnetic (EM) properties that do not exist in homogeneous natural materials. When increasing the design complexity to enhance performance, however, the computation cost hikes dramatically in analysis and synthesis as additional design variables are introduced. In contrast to such complexity increase, this thesis aims at systematically developing effective and efficient design and optimization approaches for FSS-based structures adopting fundamental unit-cell patterns, such as rectangular patches, rings and grids. Additionally, impedance matching to free space is thoroughly investigated and adapted as a means towards performance improvement in both absorbers and filters. Hereby, multiple designs are demonstrated with realizations from the microwave to the terahertz (THz) frequency spectrum. In spite of their simplicity, the proposed designs outperform the state-of-the-art counterparts in the literature by fully exhausting the potentials of their spatial structures and material attributes.

Specifically, Chapter 3 challenges a common belief that adding an impedance matching superstrate to an absorber will broaden its operation bandwidth at the cost of increased total thickness profile. This Chapter proves that it is possible to increase the bandwidth-to-thickness ratio. The concept is firstly demonstrated at the circuit level, and then verified by full-wave simulations. The optimization process can be illustrated with an admittance Smith chart. The distinctive performance of the proposed single-FSS-layer absorber is justified with a figure of merit (FoM) which comprehensively involves the relative bandwidth, the normalized thickness and the level of reflectivity.

In Chapter 4, a semi-analytical approach for absorber design is developed by systematically combining analytical, empirical and numerical techniques. The optimization space can be simplified from millions of exhaustive search cases to merely a few hundreds of seed simulations, by exploiting insights into the linearity, scalability and independence regarding the major components of an absorber. For any specified level of absorption and operation bandwidth, the obtained semi-analytical algorithm enables fast synthesis of an absorber with a minimal thickness. Both absorbers proposed in the

above chapters have been realized using patterned resistive layers and experimentally validated under oblique angles of incidence for transverse-electric (TE) and transverse-magnetic (TM) modes. The design methods can be readily expanded for structures of multiple FSS layers.

In the terahertz frequency range, common microfabrication technologies do not accommodate those resistive inks used for silk-printing lossy FSS patterns. As an alternative, a sub-skin-depth metal layer with nanoscale thickness is proposed in Chapter 5 to meet this requirement. The Drude model is adopted to simulate the ultra-thin metallic FSS, as it satisfactorily describes the frequency dependent properties of noble metals. The proposed absorber is robust to dimensional tolerance in fabrication and attains a stable absorption bandwidth under oblique impinging waves.

In Chapter 6, a frequency reconfigurable terahertz bandpass filter is proposed and experimentally verified. It includes two identical double-layer FSSs separated by an air spacer which can be mechanically tuned. The filter allows a highly selective transmission sweeping across a wide spectrum. The underlying mechanism can be explained from two perspectives, namely through interpretation as Fabry-Perot resonant cavity and through consideration of the admittance Smith chart. The designed device is insensitive to fabrication tolerances and stable to oblique angle of incidence. The fabricated filter confirms a 40% tuning range and less than 1 dB insertion loss. This design is among the first few practical reconfigurable terahertz bandpass filters reported in the literature.

Overall, the research outcomes suggest that developing complicated FSS patterns with a large number of degrees of freedom is unnecessary in many cases if the potential of fundamental geometries is fully exploited through rigorous algorithmic optimization methods. The design approaches illustrated in this thesis are generic to all FSS-based structures and can potentially be extended to multi-FSS layers and impedance surfaces, to satisfy performance requirements in specific applications.

Originality Declaration

I certify that this work contains no material which has been accepted for the award of any other degree or diploma in my name, in any university or other tertiary institution and, to the best of my knowledge and belief, contains no material previously published or written by another person, except where due reference has been made in the text. In addition, I certify that no part of this work will, in the future, be used in a submission in my name, for any other degree or diploma in any university or other tertiary institution without the prior approval of the University of Adelaide and where applicable, any partner institution responsible for the joint-award of this degree.

I acknowledge that copyright of published works contained within this thesis resides with the copyright holder(s) of those works.

I also give permission for the digital version of my thesis to be made available on the web, via the University's digital research repository, the Library Search and also through web search engines, unless permission has been granted by the University to restrict access for a period of time.

I acknowledge the support I have received for my research through the provision of an Australian Government Research Training Program Scholarship.

Signed

06/04/2021

Date

Acknowledgments

First and foremost, I would like to express my deep gratitude to my supervisors Prof. Christophe Fumeaux and A.Prof. Withawat Withayachumnankul for their thoughtful guidance and comprehensive support throughout my candidature. Both of them are very supportive, approachable and responsible scholars who help me with their extensive knowledge and experience in electromagnetic field. Their high standard and rigorous attitudes towards research are impressive to everyone not only in our school of electrical and electronic engineering, but also among IEEE communities throughout the world. Without those inspiring discussions with Prof. Christophe Fumeaux and A.Prof. Withawat Withayachumnankul, my understanding would be superficial whilst my design approach would be less strategic. Under their enthusiastic supervision, I have been enjoying designing and validating products of satisfying performance. More importantly, I sincerely appreciate the systematic research methodology that I developed with their aid. They have been making my candidature marvelous and invaluable, and this acknowledgment is limited in length to show my gratitude.

I also wish to express my appreciation to Dr. Shengjian Jammy Chen. As one of my best friends, he suggested me to develop this Ph.D degree, and introduced me to Prof. Christophe. Dr. Jammy has spent so much time with me in discussing those interesting research ideas, and encouraged me when I was experiencing difficulties. He is a reliable colleague in the workplace, and a terrific friend in daily life.

My endless gratitude goes to my father and mother who always endow me with continuous love, infinite support, and unconditional trust. They are my spiritual Great Wall inside, as always.

Xiaojing LV

April 2021

Adelaide, Australia

Thesis Conventions

The following conventions have been adopted in this Thesis:

Typesetting

This document was compiled using L^AT_EX2e. TeXstudio is used as text editor interfaced to L^AT_EX2e. Inkscape was used to produce schematic diagrams and other drawings.

Referencing

The referencing and citation style adopted in this thesis are based on the Institute of Electrical and Electronics Engineers (IEEE) Transaction style.

System of units

The units comply with the international system of units recommended in an Australian Standard: AS ISO 1000–1998 (Standards Australia Committee ME/71, Quantities, Units and Conversions 1998).

Spelling

American English spelling is adopted in this thesis.

Abbreviation

2D	Two-Dimensional
3D	Three-Dimensional
BWR	Bandwidth Ratio
CA	Circuit Analog
CEM	Computational Electromagnetics
COC	Cyclic Olefin Copolymer
DoF	Degrees of Freedom
EBG	Electromagnetic Band-Gap
EM	Electromagnetic
EMC	Electromagnetic Compatibility
EMI	Electromagnetic Interference
FDTD	Finite-Difference Time-Domain
FEM	Finite-Element Method
FIT	Finite-Integration Technique
FSS	Frequency-Selective Surface
FWHM	Full-Width at Half Maximum
GA	Genetic Algorithm
MoM	Method of Moments
PCM	Phase-Change Material
PEC	Perfect Electrical Conductor
PET	Polyethylene Terephthalate
PRS	Partially Reflecting Surface
RCS	Radar Cross Section
RF	Radio Frequency
RFID	Radio-Frequency Identification
THz	Terahertz
TL	Transmission Line
VO₂	Vanadium Dioxide

List of Figures

1.1	Fundamental unit-cell patterns arranged in groups	3
1.2	Thesis outline	9
<hr/>		
2.1	Babinet’s principle for a pair of complementary unit-cell patterns	13
2.2	Empirical observation of scalability	15
2.3	Equivalent circuit modeling for a free-standing lossless FSS	16
2.4	Balanced trade-off between accuracy and complexity when modeling staggered Jerusalem cross FSS	17
2.5	Equivalent circuits for multilayer structures	18
2.6	Theory of small reflections	19
2.7	Single-layer CA absorber under oblique angle of incidence	21
2.8	Frequency responses when building up a Jaumann absorber in the Smith chart	22
2.9	Synthesis for surface resistances with high-frequency lumped resistors	23
2.10	Introducing surface resistance by silk-printing with silver nanoparticle ink	24
2.11	Absorber performance at specified absorption levels	26
2.12	Bistatic measurement	27
2.13	Monostatic measurement	28
2.14	Design schematic and experimental configuration of high-selectivity terahertz filter	30
2.15	Spring geometry and frequency tunability	31
2.16	FSS-based varactor-tunable bandpass filter	32
2.17	Passband reconfiguration and insertion loss of a varactor-based FSS spatial filter	32
2.18	Bandpass and bandstop FSSs using phase-change materials with integrated meander loop heater	33

List of Figures

2.19	Frequency responses for reconfigurable bandstop and bandpass filters	34
<hr/>		
3.1	Schematics of a single-FSS-layer absorber with dielectric matching cover	40
3.2	Equivalent circuit model of a single-layer CA absorber	41
3.3	Bandwidth-thickness relationship for GA optimized topologies without and with dielectric superstrate	42
3.4	Optimization aiming at -10 dB level of reflection for single-layer CA absorbers without and with dielectric superstrate	43
3.5	Admittance Smith chart for wideband impedance matching manipulation	44
3.6	Reflection coefficients for the proposed design accounting for material availability	46
3.7	Equipment for the proposed absorber validation	46
3.8	Exploded view of the fabricated absorber	47
3.9	Experimental setup for absorption performance measurement	47
3.10	Measured and simulated reflection coefficients	48
<hr/>		
4.1	Overview of the semi-analytical design approach	54
4.2	Dielectric-supported lossless single-layer FSS	55
4.3	Full-wave simulated S -parameters for fundamental unit-cell patterns	57
4.4	Impact of dielectric substrate on equivalent reactive components for a reference square patch FSS	61
4.5	Equivalent circuit models for unit-cell FSS adopting a patterned resistive layer	63
4.6	Reflection coefficients for random designs in four different absorber topologies	66
4.7	Optimized bandwidth-thickness curves for different topologies as illustrated in Fig. 4.6	67
4.8	Absorption performance for designs during steps of the synthesizing process	69
4.9	Optimized bandwidth-thickness curves for single-FSS-layer absorbers with performance margin included for fabrication tolerances	70

4.10	Fabricated single-FSS-layer absorber	71
4.11	Simulated and measured reflection coefficients for near-normal incidence	71
4.12	Proposed absorber under oblique incidences for (a) TE and (b) TM modes	72
<hr/>		
5.1	Unit-cell schematic of a square ring based single-FSS-layer absorber . . .	78
5.2	Simulated and calculated reflection coefficients for the proposed design	80
5.3	Frequency-dependent relative permittivity and bulk conductivity of silver (Ag)	81
5.4	Comparison between simulated reflection coefficient for the proposed design adopting different resistive materials for the FSS	82
5.5	Simulated reflection coefficients for geometric imperfections	82
5.6	Simulated reflection coefficients	83
<hr/>		
6.1	Proposed FSS-based frequency reconfigurable bandpass filter	88
6.2	Power transmission of the proposed tunable FSS	89
6.3	Modified equivalent circuit including lossy transmission line sections and <i>RLC</i> branches	90
6.4	Mutiple-beam interference in the proposed Fabry-Perot resonance cavity	91
6.5	Non-linear relationship between the air spacer thickness and the operation frequency	92
6.6	Power reflection of the double-layer FSS and finesse of the reconfigurable filter	93
6.7	Admittance Smith charts for narrowband perfect impedance matching manipulation	94
6.8	Frequency reconfiguration demonstrated with admittance Smith chart .	95
6.9	Filter assembly with random misalignment of FSSs	96
6.10	Impact of unit-cell misalignment on reconfigurable bandpass filtering .	96
6.11	Power transmission for TE and TM modes under oblique incidence . . .	98
6.12	Observations under the optical microscope during FSS fabrication process	99
6.13	Reconfigurable bandpass filter assembly on a mechanically tunable holder	99

List of Figures

6.14	Setup for experimental verification of the proposed design	100
6.15	Measured power transmission of the proposed reconfigurable bandpass filter	101

List of Tables

3.1	Equivalent RLC values and transmission line attributes for both topologies	42
3.2	Dimensions and material parameters for both topologies	43
3.3	Comparison of the notable fabricated single-FSS absorbers	49
4.1	Dimensions and material attributes for schematics in Fig. 4.6	64
4.2	Equivalent circuit components (two decimals) for lossy FSSs in Fig. 4.6 .	64
5.1	Equivalent circuit and transmission line characteristics	79
5.2	Structural dimensions and material attributes	79
6.1	Comparison with other frequency reconfigurable filters	102

Chapter 1

Introduction

THIS introductory chapter briefly presents an overview of the frequency-selective surfaces (FSSs) and discusses their electromagnetic (EM) characteristics in association with geometric features. The motivation and objectives of the research work are highlighted together with the original contributions. The structural organization of the thesis is outlined at the end of this chapter.

1.1 Introduction

1.1.1 Frequency-Selective Surfaces: Definition and Applications

A frequency-selective surface (FSS), in essence, is a thin periodic array that interacts with electromagnetic (EM) waves at specific frequencies. It enables improved EM performances that cannot be easily or economically obtained by layered structures adopting homogeneous natural materials. A typical two-dimensional (2D) FSS periodically assembles identical unit-cells with subwavelength spacings [1].

A considerable number of research projects have been focusing on exploration of FSS unit-cell patterns [2–7], the study of which facilitates the acquisition of empirical design principles for FSS-based structures. Figure 1.1 illustrates four groups of typical unit-cell patterns which are categorized based on the similarities in their geometric features. This structural resemblance translates into similarity in the electromagnetic characteristics including resonating modes, polarization response, bandwidth control and sensitivity to angle of incidence [1]. For additional degrees of freedom (DoFs) in controlling the response, the fundamental FSS shape may evolve into more sophisticated geometries [5–12], adopt 3D-printed materials of non-negligible thickness [13–15], or incorporate varactor diodes for reconfigurability [16, 17].

There exists a variety of FSS-based applications. Resonance is the most common phenomenon of an FSS under excitation. Therefore an FSS can be employed as a spatial bandpass or bandstop filter for wireless communications [7, 13, 16]. Modern airborne radomes adopt FSS as a shield to reduce the radar cross section (RCS) in an increased frequency range [1, 15]. Further reduction in the RCS can be achieved by involving surface resistance for circuit analog (CA) absorbers and rasorbers in stealth technology [2, 3, 6, 8–12, 14]. A metallic FSS over a thin grounded dielectric slab can be regarded as a subwavelength cavity. Its “total reflection” and “total absorption” states encode the “0” and “1” bit thus can be adapted for chipless radio-frequency identification (RFID) tags [18]. When designing a partially reflecting surface (PRS) antenna for high directivity, low profile and simple configuration, the planar PRS material can be realized with a similar method used to design an FSS [17]. Other applications include but are not limited to meanderline polarizers [1], reflectarrays [4, 5, 17], and energy harvesters [19].

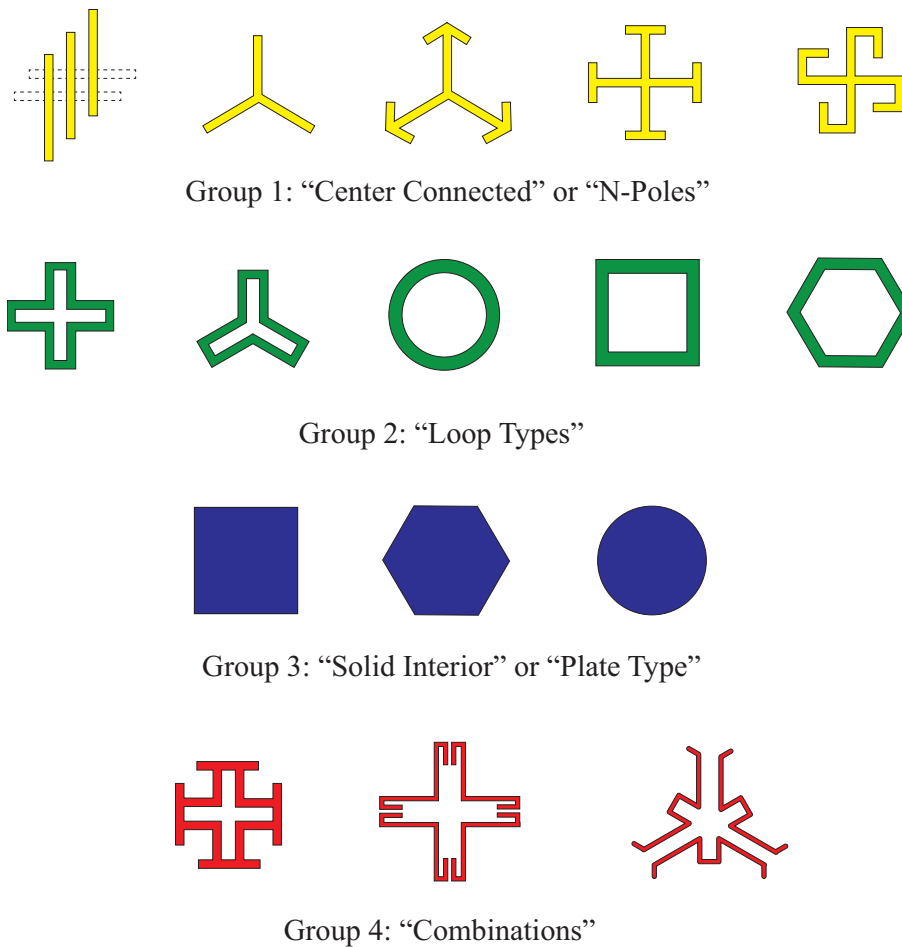


Figure 1.1. Fundamental unit-cell patterns arranged in groups. The categorization is based on the geometric features and EM characteristics. Adapted from [1].

1.1.2 Research Motivations and Thesis Objectives

Although design principles for the fundamental unit-cell patterns have been empirically developed as mentioned earlier, a more reliable approach with sufficient accuracy and broad versatility is required. The finite-elements method (FEM), the finite-difference time-domain (FDTD) method, Finite-Integration Technique (FIT) and the method of moments (MoM) are suitable candidates for full-wave simulation from computational electromagnetics (CEM). Momentum™ is a typical MoM simulator element of ADS platform, which is notably weak when handling losses in heterogeneous geometries. The FEM based simulator HFSS™ and FIT based simulator CST™ have been well acknowledged for their capacity and reliability regarding any FSS shapes with lossy supporting dielectrics. However, as the DoF increases with additional geometric

1.1 Introduction

features in the unit-cell, these full-wave simulations quickly become computationally prohibitive in terms of hardware resources or simulation time.

With a physical insight into the unit-cell geometry, an FSS layer can be alternatively regarded as a shunt equivalent circuit branch in a transmission line (TL) formalism [20]. In response to the electrical field of an impinging wave, a disconnection can be represented by an equivalent capacitor whilst a strip can be modeled as an equivalent inductor. Sheet resistance can be presented as lumped resistors depending on the unit-cell geometry, and their values are inversely related to the effective area relative to the unit-cell size [21, 22]. The performance of an FSS can be then described by the Maxwell's equations and corresponding analytical formulas from TL theory [1, 23]. The Smith chart enhances perception in analysis and synthesis via circuit modeling software such as Keysight ADS™.

On such a basis, it is firstly worth investigating whether the TL techniques have been extensively utilized when designing an FSS-based structure. Considering the CA absorber for example, impedance matching to free space not only can be improved by exploring increasingly sophisticated FSS [8–12, 24], but also by considering the transmission line topology as a whole [1, 22, 25]. There are drawbacks in building an equivalent circuit model. For a specified unit-cell pattern, a simple *RLC* in series is unlikely to reproduce the wideband performance accurately except for a square patch FSS. Furthermore, existing analytical expressions that link the geometrical dimensions to equivalent circuit configurations are often complicated, and their accuracy does not satisfy practical needs [26–29]. Thus, circuit models are mainly used as an analysis tool rather than for synthesis purpose.

So far, the theories and realizations of FSSs have concentrated on the microwave domain. However, most conclusions in the microwave spectrum can be applied directly to the neighboring terahertz range. There are however aspects that need to be specifically adapted or taken into account:

- Material attributes. Low-loss dielectrics in the microwave range can be significantly lossy in the terahertz range, which can restrict the choice of available materials for a desired permittivity [30].
- Fabrication techniques. Unit-cell patterning is restricted by the current microfabrication technology. It is also impractical to obtain reconfigurability via voltage

varactors, because the THz components are much lossier due to decreased capacitance and hence decreased capacitor's cross-section and thus increasing resistance in series.

- **Adaptability.** The resistive surface is a necessity when designing planar CA absorbers. Accessible printed resistive surfaces for microwave designs cannot be treated as infinitely thin in the terahertz domain, because their thicknesses become comparable to the operation wavelength. The design approach from the microwave spectrum can only be adapted with a readily available technique in fabricating suitable resistive sheets.
- **Evaluation criteria.** The total thickness of the dielectric layers, for example, is critical for the microwave absorber designs but not practically necessary in the terahertz spectrum. The benefit in miniaturization may not well offset the increased difficulty and reduced robustness in microfabrication.

In response to the earlier background findings, the major objectives of this thesis are listed as follows:

1. Revisit simple and readily available techniques based on the transmission line theory to design microwave CA absorbers. Based on this investigation, a systematic approach for global optimization will be proposed. The design algorithm aims for acceptable accuracy in comparison to full-wave simulators while dramatically reducing the time consumption so as to maximize the potential of a chosen FSS shape. This approach should be generic, and its effectiveness needs be verified by comparing the standardized performance, namely accepted Figure of Merit (FoM), to any other single-FSS-layer designs in the literature. The fabricated absorbers should consider the limitation in materials and accommodate fabrication tolerances.
2. Within the state-of-the-art microfabrication technology, extend the design approach for CA absorbers from the microwave spectrum to the terahertz regime without violating the presumptions. Explore FSS-based resonant structure and propose a highly selective and mechanically reconfigurable bandpass filter that operates in a wide frequency range.

1.2 Statement of Original Contributions

A number of original contributions to the field of FSS are included in this thesis, which can be grouped into four major parts.

- **Single-FSS-Layer Absorber Adopting Impedance Matching Superstrate for Improved Bandwidth-Thickness**

Electromagnetic absorption can be regarded as an impedance matching problem to free space. A dielectric cover as impedance transformer has been known to enhance the bandwidth and absorption level at the cost of increased total thickness. In Chapter 3, this common belief is challenged by demonstrating that improved absorption performance and lower thickness profile can be achieved simultaneously. The proof involves an optimized equivalent circuit which is then verified by the full-wave simulation. It also can be inferred that air spacer is an ideal substrate for wideband absorber design. For fair comparison, an appropriate FoM is evaluated by considering how close the thickness of an absorber is to the theoretical optimum for the obtained absorption performance [31]. The fabricated design outperforms other experimentally validated polarization-independent counterparts adopting single-layer FSS in the literature. This design has been reported in *IEEE Antennas and Wireless Propagation Letters* under the title of "Single-FSS-Layer Absorber With Improved Bandwidth-Thickness Tradeoff Adopting Impedance-Matching Superstrate" [22].

- **Semi-Analytical Method for Fast Global Optimization**

Despite the fact that equivalent circuit models have been widely used when designing CA absorbers, there are no sufficiently accurate analytical expressions linking the geometric dimensions with equivalent circuit parameters. In this case, the potential of fundamental FSS patterns cannot be fully exhausted, and such non-global optimization leads to additional efforts in exploring unnecessarily complicated unit-cell geometries. In Chapter 4, a few sets of multi-regression functions for square patch and ring are obtained by systematically integrating analytical, empirical and numerical techniques. Executing only a limited number of seed simulations, the proposed semi-analytical algorithm can effectively and efficiently search the entire solution space with acceptable accuracy. Embedding a genetic algorithm (GA) in this design approach enables fast optimization for any specified absorption performance within a feasible range. The performance

margins for proposed absorber topologies can be generated for comparison purpose. It is found that an optimized square ring absorber can have a lower profile for specified absorption performance compared to other more complex single-FSS-layer absorbers in the open literature. The fabricated absorber takes into account material availability and fabrication tolerance. This work has been published in *IEEE Open Journal of Antennas and Propagation* under the title of "Fast Semi-Analytical Design for Single-FSS-Layer Circuit-Analog Absorbers" [32].

- **Terahertz Absorber with Metallic FSS in Sub-Skin-Depth Thickness**

Considering the current capability and reliability in microfabrication technologies, the resistive sheets commonly used in the microwave spectrum (e.g., printed conductive polymer) are no more suitable for terahertz FSS designs, since a precise control of the geometric dimensions and sheet resistance becomes unfeasible. To apply the design techniques developed in the previous chapters, Chapter 5 presents an approach to determine surface resistance of FSS with patterned noble metal layers of sub-skin-depth thickness, which satisfies the readily available microfabrication techniques. The Drude model is adopted for calculation of the metal properties because of its frequency-dependent feature in the terahertz range. This design was presented at *IEEE Asia-Pacific Microwave Conference (APMC), 2019* under the title of "Terahertz Absorber Design Adopting Metallic FSS in Sub-Skin-Depth Thickness" [33].

- **Mechanically Reconfigurable Terahertz Bandpass Filter of High Selectivity and Wide Tuning Range**

The complimentary shape of a "Center Connected" or "Loop" FSS resonator performs as a bandpass filter according to the Babinet's principle [1]. However, filters of this type usually come with strong spurious transmission, poor selectivity and low transmission efficiency. Due to the fabrication complexity at the micrometer scale, the realization of tuning structures becomes challenging for terahertz applications. It has been proposed in the literature that reconfigurability can be realized by adopting phase-change materials with a heating source [34]. In Chapter 6, a mechanical reconfigurable bandpass filter operating in the frequency range from 220 GHz to 330 GHz is proposed. The filter is composed of multiple FSS-layers and can be regarded as a Fabry–Perot cavity where the operation frequency can be tuned by changing the thickness of the air spacer. The

1.3 Thesis Structure

filter attains high transmission of over 80% in power whilst remaining high selectivity throughout the tuning range. This research work has concluded and will be submitted to *IEEE Transactions on Terahertz Science and Technology* for peer review.

The research work in this dissertation mainly concentrates on optimizing CA absorbers and reconfigurable bandpass filters. However the proposed design approach can be adapted for analyzing and synthesizing any other FSS-based multilayer structures.

1.3 Thesis Structure

As illustrated in Fig. 1.2, this thesis starts with introduction and literature review in the first two chapters and ends up with conclusion and outlook in the last chapter. The chapters in-between detail the major contributions, including impedance matching superstrate for CA absorber, fast semi-analytical optimization, metallic FSS in sub-skin-depth and reconfigurable bandpass filter.

I Introduction (Chapters 1 & 2)

The first part of the thesis includes this introductory chapter and Chapter 2 where the fundamentals and the background information for the whole dissertation are provided. The second chapter contains a literature review on the FSS-based structures with related background theories and a few preliminary designs to gain some insight into the CA absorber and spatial filter.

II Systematic Design Approach and Evaluation Criteria for Microwave Absorbers (Chapters 3 & 4)

Chapter 3 encompasses a simple but effective approach to improving the bandwidth-thickness trade-off of an absorber without seeking for complicated FSS shapes. The demonstration challenges the common perspective on using a dielectric transformer, and the fabricated sample outperforms its single-FSS-layer counterparts. Chapter 4 adopts the impedance matching superstrate and realizes a semi-analytical algorithm that systematically integrates available formulas, empirical observations and statistical tools. The proposed fast computation capacity allows true global optimization thus an absorber with fundamental FSS shape can be fully exploited for a better bandwidth-thickness ratio compared to designs of more complicated patterns.

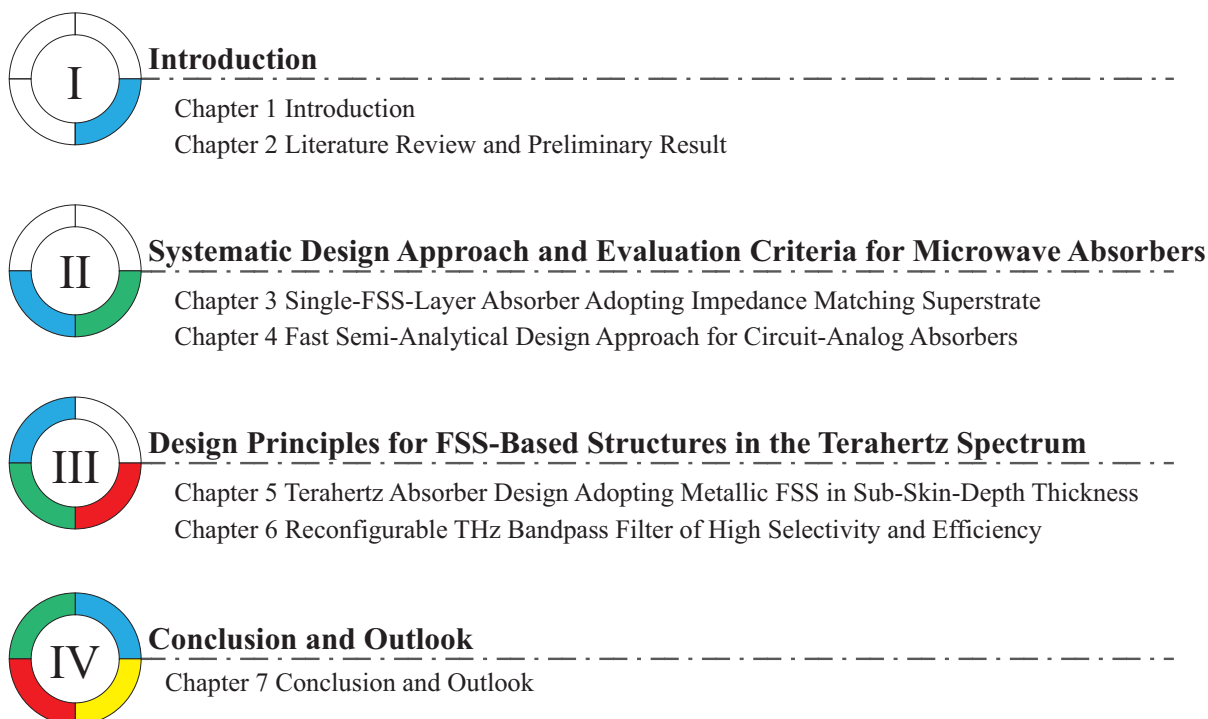


Figure 1.2. Thesis outline. The first two chapters include introduction and literature review while the last chapter concludes the dissertation with future work. The chapters in-between detail the original contributions of the dissertation.

III Design Principles for FSS-Based Structures in the Terahertz Spectrum (Chapters 5 & 6)

Chapter 5 explores the property of sub-skin-depth metal using the Drude model at terahertz frequencies. It allows a CA absorber design embedding an electrically thin FSS so that the majority conclusions from the microwave spectrum can be reused. Chapter 6 shows a reconfigurable terahertz bandpass filter operating in the frequency range from 220 to 330 GHz. The mechanism is based on the Fabry-Pérot cavity and the performance is compared to the state-of-the-art designs in the literature.

IV Conclusion and Outlook (Chapter 7)

The last chapter concludes all the projects presented in this thesis, and also discusses an outlook into this field.

Chapter 2

Background of Frequency Selective Surfaces

FREQUENCY selective surfaces (FSSs) have been widely used in wireless systems to create spatial filters and in stealth technology to realize thin absorbers. The patterning of a unit-cell effectively shapes the electromagnetic performance in terms of bandwidth, selectivity or efficiency. This chapter firstly systematically covers a series of fundamental theories and techniques for FSS-based structure design. Then the fabrication techniques, evaluation criteria and typical experimental setups for circuit analog (CA) absorbers are briefly discussed. The possibility of adding reconfigurability to FSS filters is also reviewed at the end of this chapter.

2.1 Introduction

FSS-based planar structures have attracted increasing attention because of their broad operation bandwidth, low thickness profile and flexibility of material realizations. The analysis and synthesis of an FSS in full-wave simulations, however, tend to be complicated. Thus, more efficient design approaches are always preferred.

This chapter begins with a number of existing design principles and techniques for FSS modeling. Then, a brief literature review of the state-of-the-art CA absorbers and bandpass filters will be presented from the perspective of equivalent circuit models and transmission line topologies. A focus will be placed on the research challenges of obtaining outstanding performance by exhausting the potentials of simple geometries made of widely available materials and readily accessible fabrication technologies.

2.2 Fundamental Theories and Techniques

Although modern full-wave electromagnetic simulators are capable of predicting accurate frequency response for an FSS-based structure, a global optimization becomes unrealistically time-demanding when adding more geometric features to a fundamental unit-cell pattern or when stacking multiple FSS layers. Before applying optimization tools such as the genetic algorithm (GA), it is advantageous to reduce the number of full-wave simulations by involving relevant physical laws, empirical rules and modeling techniques.

2.2.1 Babinet's Principle for Complementary FSSs

A pair of periodic arrays or FSSs are said to be complementary when the unit cell metallic pattern of one can be exactly filled up by the other. According to the Babinet's principle, the reflection coefficient for a free-standing lossless FSS equals the transmission coefficient of its complementary [1]. Taking the example of a square ring FSS and a central-loaded grid FSS, the $|S_{11}|$ of the former and the $|S_{21}|$ of the latter match closely as demonstrated in Fig. 2.1.

On this basis, the number of full-wave simulations can be reduced to a half when exploring unit-cell geometries. It should be noted that, however, there exist a few restrictions [1]:

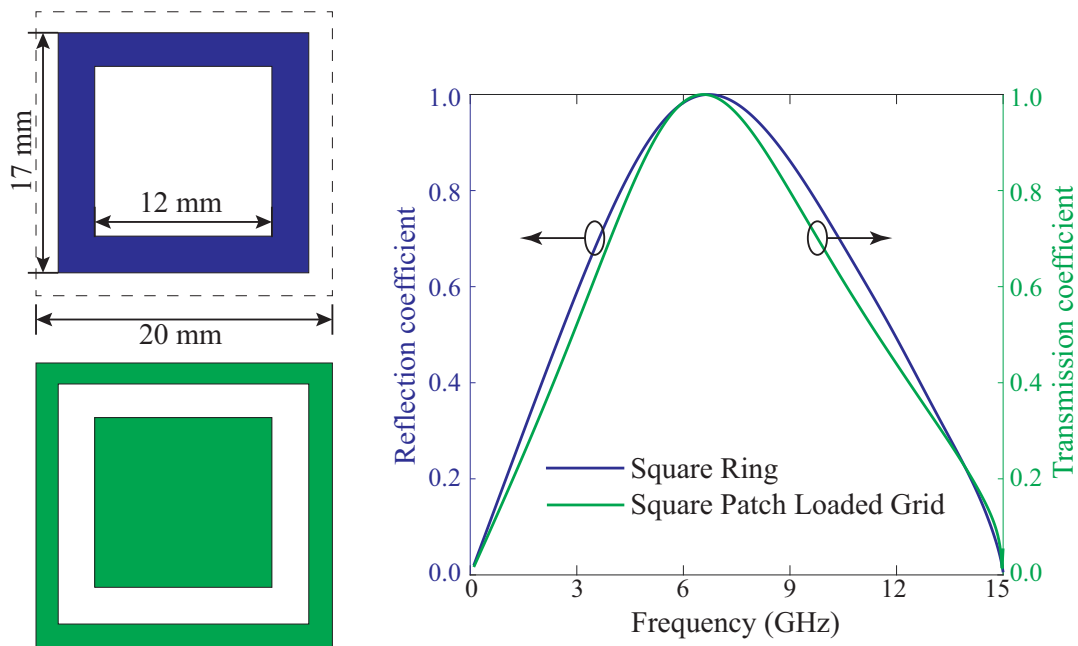


Figure 2.1. Babinet's principle for a pair of complementary unit-cell patterns. Both square ring and square patch loaded grid FSSs are lossless and free-standing. The periodicity is 20 mm, and the other dimensional parameters are randomly picked for demonstration purpose.

Zero surface impedance. To ensure a good matching in paired S -parameters, the complementary FSSs must be made of near perfect electrical conductors (PECs), and near infinitely thin i.e., less than $1/1000$ of the wavelength at the highest operation frequency λ_H .

Free-standing array. A supporting dielectric substrate thinner than a quarter of λ_H equally lowers the resonance frequency for both complementary FSSs, but the mismatching of paired S -parameters in a broader frequency range becomes significant as they are no longer complementary with the dielectric layers. In practice, a PF4 ($\epsilon_t = 1.06$, $\tan\delta = 0.0001$) foam spacer or 100 μm polyester (PET) film can be used for mechanical supporting purpose without significantly breaching the requirements for complementary FSSs in the microwave spectrum.

Single layer. Stacking multiple FSS layers can improve performance in terms of increased operation bandwidth, more consistent in-band response and steeper fall-off edges. However, this renders the Babinet's principle invalid. To maintain validity of this principle, the overall frequency response has to be calculated from the transmission line topology and the frequency response of each FSS.

2.2.2 Scalability: from Physical Dimensions to Frequency Response

Resizing an FSS-based structure with a three-dimensional scaling factor ζ will proportionally relocate the transmission and reflection coefficients by $1/\zeta$ in the frequency spectrum. In contrast to the Babinet's principle, scalability has less restrictions if the properties of metals and dielectrics remain constant across the frequency range of interest.

Scalability remains valid for an FSS of any surface impedance, on any supporting dielectric substrate, and when cascaded to any other FSSs. As illustrated in Fig. 2.2, an example design adopts an annulus and a patch loaded grid as the unit cell. The physical dimensions, dielectric spacer and surface resistance are all randomly picked. Rescaling the structure with $\zeta = 50\%$ precisely stretches the reflection coefficient curve by a factor of 2 in the spectrum.

When optimizing FSS-based structures, the bandwidth is always evaluated on a relative basis because of the scalability. The periodicity can then adopt a constant value and thus the number of design variables will be readily reduced by 1. The scaling factor applies on the physical dimensions excluding the thickness of the FSS which determines its surface resistance.

2.2.3 Equivalent Circuit Modeling of a Unit-Cell Geometry

Similarly to the analysis of microstrip lines or electromagnetic band-gap (EBG) structures, an appropriate equivalent circuit model provides in-depth understanding that may enable full exploitation of the potentials of an FSS topology. Typically, a strip that allows current flow can be modeled as an inductor, whilst a gap that stores electric charges can be modeled as a capacitor.

When synthesizing the unit-cell geometry as shown in Fig. 2.3 (a), an explicit circuit model illustrated at the left of Fig. 2.3 (b) allows precise analysis of the S -parameters and fine tuning. Although at a specific frequency this high-order circuit configuration can be simplified into an RLC in series, such over-simplification is invalid for non-fundamental FSS patterns across a broad spectrum. Figure. 2.3 (c) indicates a close fitting of the results from the explicit circuit calculation to the full-wave simulation, while the over-simplified model fails in matching the wideband S -parameters.

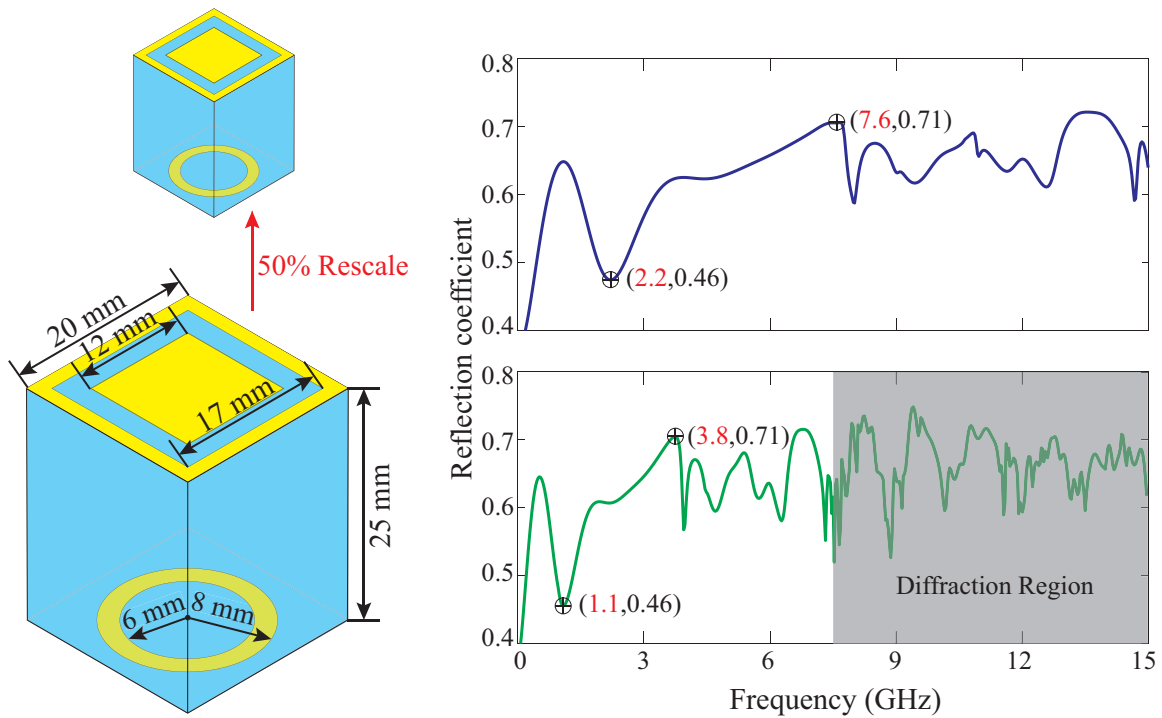


Figure 2.2. Empirical observation of scalability. The unit-cell size is 20 mm, and the other dimensional parameters are randomly picked for demonstration purpose. The surface resistance for both FSSs is $50 \Omega/\square$, and the dielectric spacer is silicon dioxide ($\epsilon_r = 4$, $\tan\delta = 0$). The scaling factor here is 50%.

It should also be noted that the equivalent circuit modeling is a design aid rather than a replacement for the full-wave simulation. Considering the additional computation cost arising from adding more circuit elements, a trade-off in simplicity versus accuracy is necessary, where not all geometric features of the FSS must be explicitly reflected in the equivalent circuit model. In practice, a circuit model depicting the major geometric features can suffice and yield acceptable accuracy in a limited frequency range. As shown in Fig. 2.4 [35], an *RLC* in series does not qualify to describe the wideband frequency response for a staggered Jerusalem cross FSS. However, with only one equivalent capacitor added in parallel, which is still insufficient for explicit modeling, the reflection coefficient of the modified circuit model closely matches the full-wave simulated result.

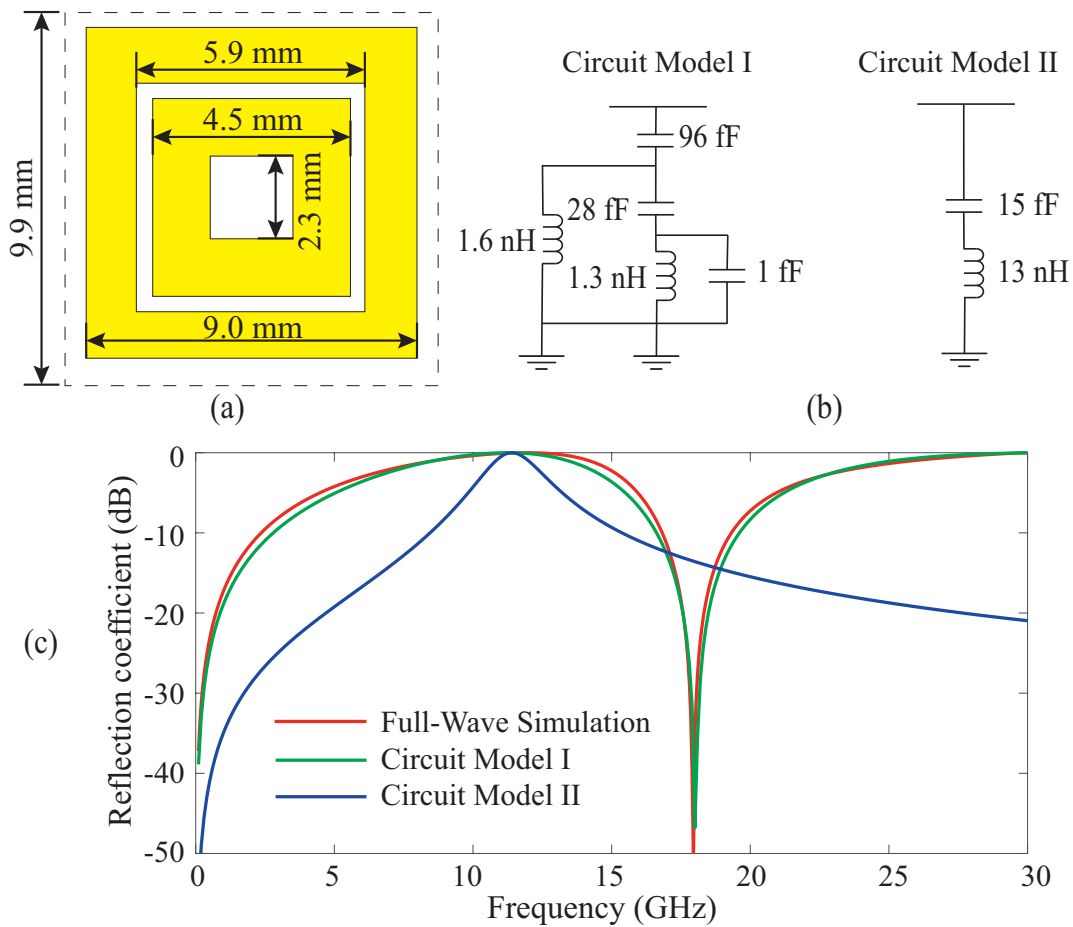
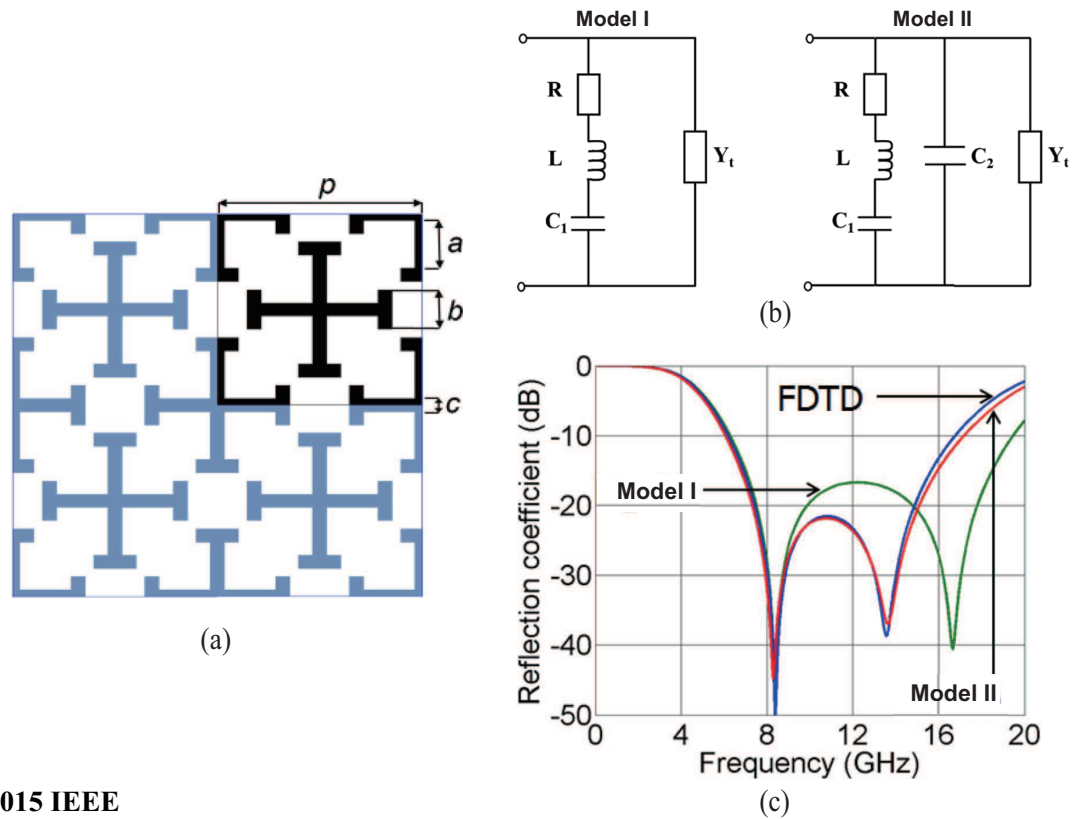


Figure 2.3. Equivalent circuit modeling for a free-standing lossless FSS. (a) The unit-cell geometry adopts nested square loops with randomly picked dimensions; (b) Two equivalent circuit models at different levels of complexity where the parameters are obtained by matching the zeros and poles; (c) Reflection coefficient curves from the full-wave simulation and the equivalent circuit calculation.

2.2.4 Transmission Line Approach for Multilayer Structures

A multilayer structures can be depicted with a topology where the FSSs are shunting circuit branches and the dielectric spacers are transmission line sections. For both CA absorbers and filters, the design problem in essence is impedance matching to the free space. The intrinsic impedance of air is $\sqrt{\mu_0/\epsilon_0} = 377 \Omega$, and a metal plate is modeled as a shorting [23].The following details the basics of building and analyzing equivalent circuit models that represent multilayer structures.



© 2015 IEEE

Figure 2.4. Balanced trade-off between accuracy and complexity when modeling staggered Jerusalem cross FSS. (a) The unit-cell geometry with four essential design variables; (b) over-simplified and appropriate circuit models; and (c) frequency responses from the FDTD simulation and equivalent circuit calculations. [35]

Multilayer Buildup

Assuming that an initial layer of FSS arrays or dielectric spacer with an input impedance Z_{load} is given as the basis. A planar multilayer structure can be synthesized by sequentially and alternately stacking more FSSs and dielectrics, which are respectively demonstrated in the following:

- When adding an FSS array to this existing structure, as shown in Fig. 2.5 (a), the input impedance can be directly calculated as:

$$Z_{\text{in}} = Z_{\text{FSS}} || Z_{\text{load}}, \quad (2.1)$$

where Z_{FSS} represents the impedance for the FSS, and $||$ indicates parallel circuit topology for simplicity. If the intrinsic impedance of a dielectric layer added on

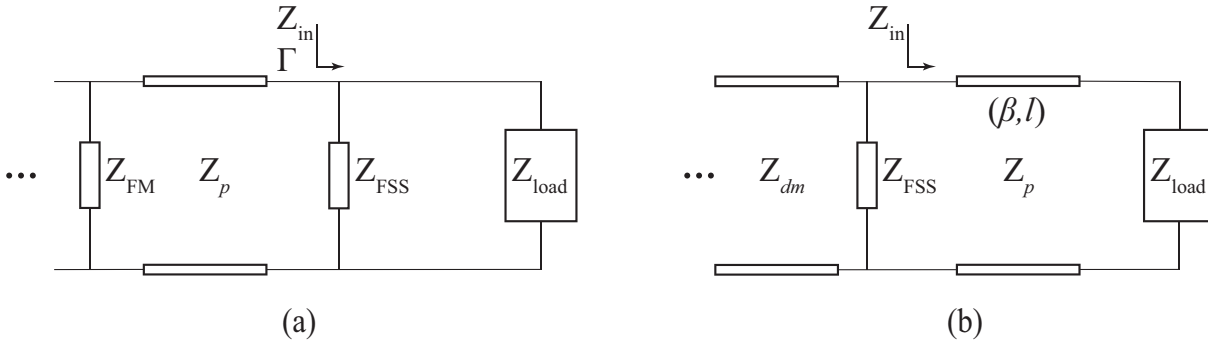


Figure 2.5. Equivalent circuits for multilayer structures. Equivalent topology when adding (a) an FSS as a circuit branch; (b) a dielectric slab of specified propagation constant and length as a transmission line section.

top of the FSS is Z_p , then the reflection coefficient at this interface is:

$$\Gamma = \frac{Z_{\text{FSS}} \parallel Z_{\text{load}} - Z_p}{Z_{\text{FSS}} \parallel Z_{\text{load}} + Z_p}. \quad (2.2)$$

- By adding a lossless dielectric layer of permittivity ϵ_p and thickness l , as shown in Fig. 2.5 (b), the total input impedance including the dielectric slab can be calculated as:

$$Z_{\text{in}} = Z_p \frac{Z_{\text{load}} + jZ_p \tan \beta l}{Z_p + jZ_{\text{load}} \tan \beta l} \quad (2.3)$$

where $\beta = 2\pi f \sqrt{\epsilon_p \mu_0}$ is the propagation constant, and Z_p is the intrinsic impedance of this dielectric layer.

Theory of Small Reflections

In some special cases, the total frequency response of a multilayer structure can be more conveniently investigated through a physical insight into the partial response at each discontinuity and applying the concept of interference. This theory of small reflections has been used in various multisection transformers for improved impedance matching or enlarged bandwidth.

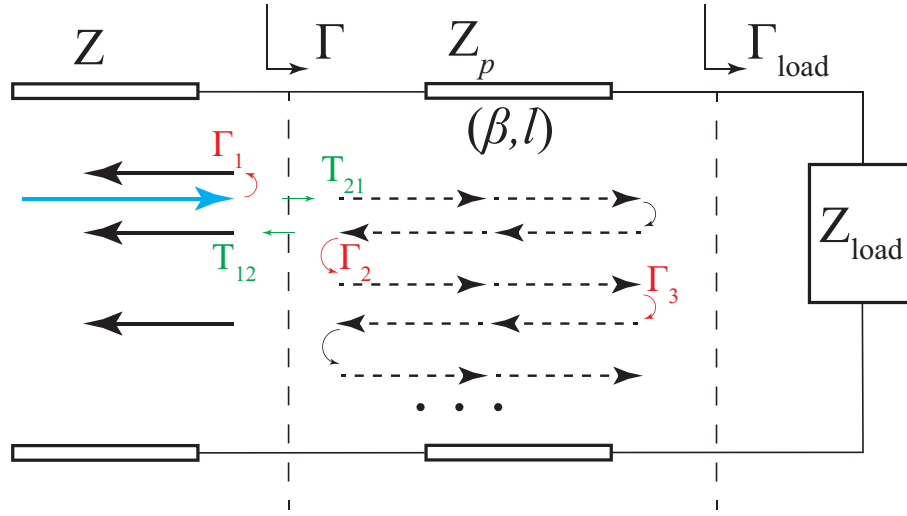


Figure 2.6. Theory of small reflections. Partial reflections and transmissions across a single-section matching transformer. Adapted from [23].

As the basis, a single-layer dielectric transformer is illustrated in Fig. 2.6, where the partial reflection and transmission coefficients are [23]:

$$\begin{aligned}
 \Gamma_1 &= \frac{Z_p - Z}{Z_p + Z}; \\
 \Gamma_2 &= -\Gamma_1; \\
 \Gamma_3 &= \frac{Z_{\text{load}} - Z_p}{Z_{\text{load}} + Z_p}; \\
 T_{21} &= 1 + \Gamma_1 = \frac{2Z_p}{Z + Z_p}; \\
 T_{12} &= 1 + \Gamma_2 = \frac{2Z}{Z + Z_p}.
 \end{aligned} \tag{2.4}$$

Thus, the overall reflection coefficient can be expressed as an infinite summation in form of the geometric series:

$$\begin{aligned}
 \Gamma &= \Gamma_1 + T_{12}T_{21}\Gamma_3e^{-2j\beta l} + T_{12}T_{21}\Gamma_3^2e^{-4j\beta l} + \dots \\
 &= \Gamma_1 + \frac{T_{12}T_{21}\Gamma_3e^{-2j\beta l}}{1 - \Gamma_2\Gamma_3e^{-2j\beta l}} \\
 &= \frac{\Gamma_1 + \Gamma_3e^{-2j\beta l}}{1 + \Gamma_1\Gamma_3e^{-2j\beta l}}.
 \end{aligned} \tag{2.5}$$

This theory also can be applied to the analysis of CA absorbers under oblique wave incidence. In Fig. 2.7, the load is shorted by a ground plane and the FSS circuit branch

is placed at the discontinuity. The total reflection coefficient can be calculated using Equation (2.5), in which the partial reflection coefficients are:

$$\begin{aligned}\Gamma_1 &= \frac{Z_{\text{FSS}} \parallel Z_{\text{I}} - Z_{\text{II}}}{Z_{\text{FSS}} \parallel Z_{\text{II}} + Z_{\text{I}}}, \\ \Gamma_2 &= \frac{Z_{\text{FSS}} \parallel Z_{\text{I}} - Z_{\text{II}}}{Z_{\text{FSS}} \parallel Z_{\text{I}} + Z_{\text{II}}}, \\ \Gamma_3 &= -1,\end{aligned}\tag{2.6}$$

where the equivalent wave impedance for the superstrate and substrate are $Z_{\text{I}} = Z_1 / \cos \theta_1$ and $Z_{\text{II}} = Z_2 / \cos \theta_2$ under TE mode, whilst $Z_{\text{I}} = Z_1 \cos \theta_1$ and $Z_{\text{II}} = Z_2 \cos \theta_2$ for TM mode. θ_1 and θ_2 respectively represent the incidence and refraction angles. The reflection coefficient for the metal ground is -1 .

Smith Chart

In addition to the above analytical approach adopting a multi-section transformer, the Smith chart as a qualitative tool can efficiently aid the synthesis procedure aiming for improved impedance matching [1, 20, 25, 36]. Specifically, the Smith chart can intuitively direct the optimization of multilayer structures including the thickness and permittivity of a dielectric slab as well as surface impedance of an FSS.

The performance of a CA absorber or an FSS filter can be estimated by the length and shape of the input impedance or admittance locus located inside the standing wave ratio (SWR) circle that represents a specified level of acceptable reflectivity. Adding a patterned resistive surface will shift and resize the locus based on the real and imaginary parts of its equivalent circuit model, whilst appending a dielectric slab will rotate the locus depending on its physical thickness and relative permittivity. To broaden the operation bandwidth and reduce the level of reflectivity, a dense locus clustered into the center of the Smith chart is expected. Such a series of manipulations are not always unidirectional, where under-compensation or over-compensation are sometimes necessary at intermediate steps. In other words, the impedance matching is not gradually improved after adding each FSS or dielectric slab, but rather globally optimized as a whole.

The Smith chart not only suits analysis for specular TEM mode, but also works for TE and TM modes under oblique incidence. Figure 2.8 shows an example of a Jaumann absorber for simplicity, however this design approach still remains feasible to multilayer CA absorbers [36]. As illustrated in the Smith chart, each locus corresponds to

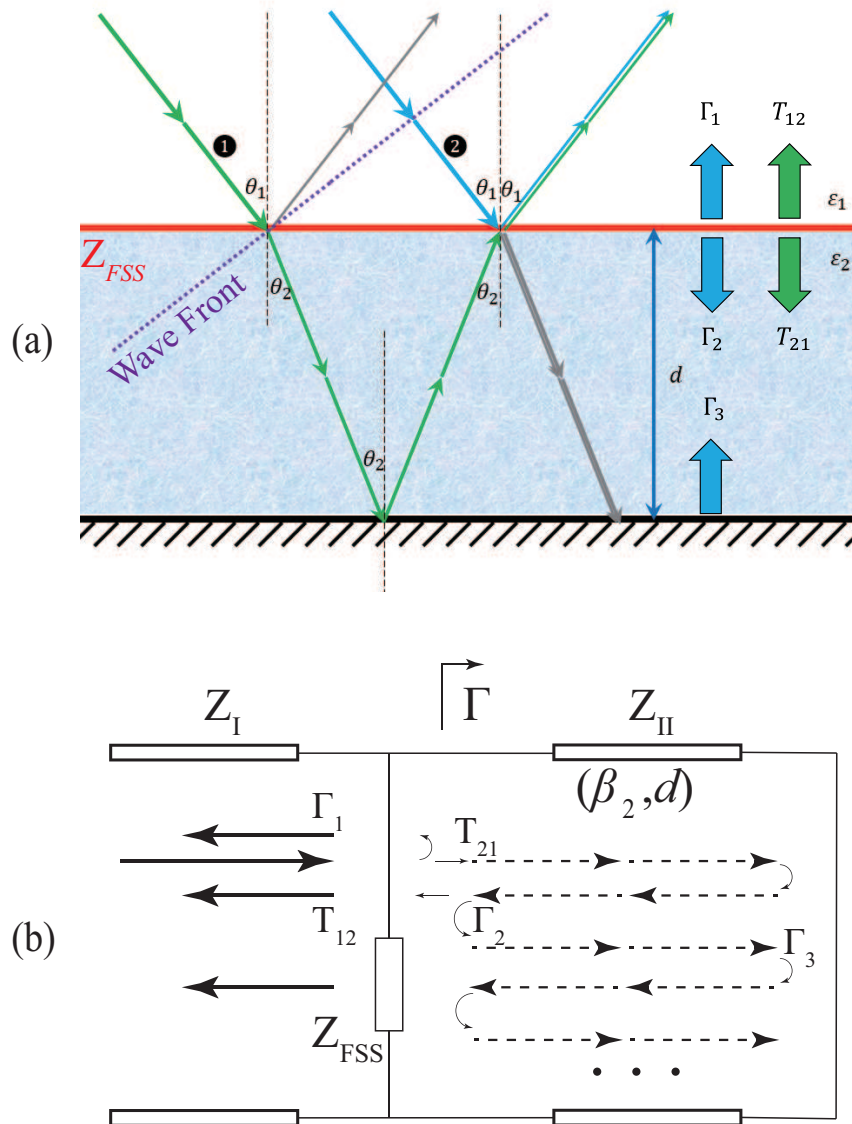


Figure 2.7. Single-layer CA absorber under oblique angle of incidence. (a) Partial reflections and transmissions inside the physical structure, which also shows the phase delays along the paths; (b) equivalent transmission line topology.

the input impedance over the spectrum of interest at a position in the multilayer absorber. The loci evolve differently for TE and TM modes because the equivalent wave impedance for the dielectric spacers differ under oblique incidence as calculated previously.

2.3 FSS-Inspired Circuit Analog Absorbers

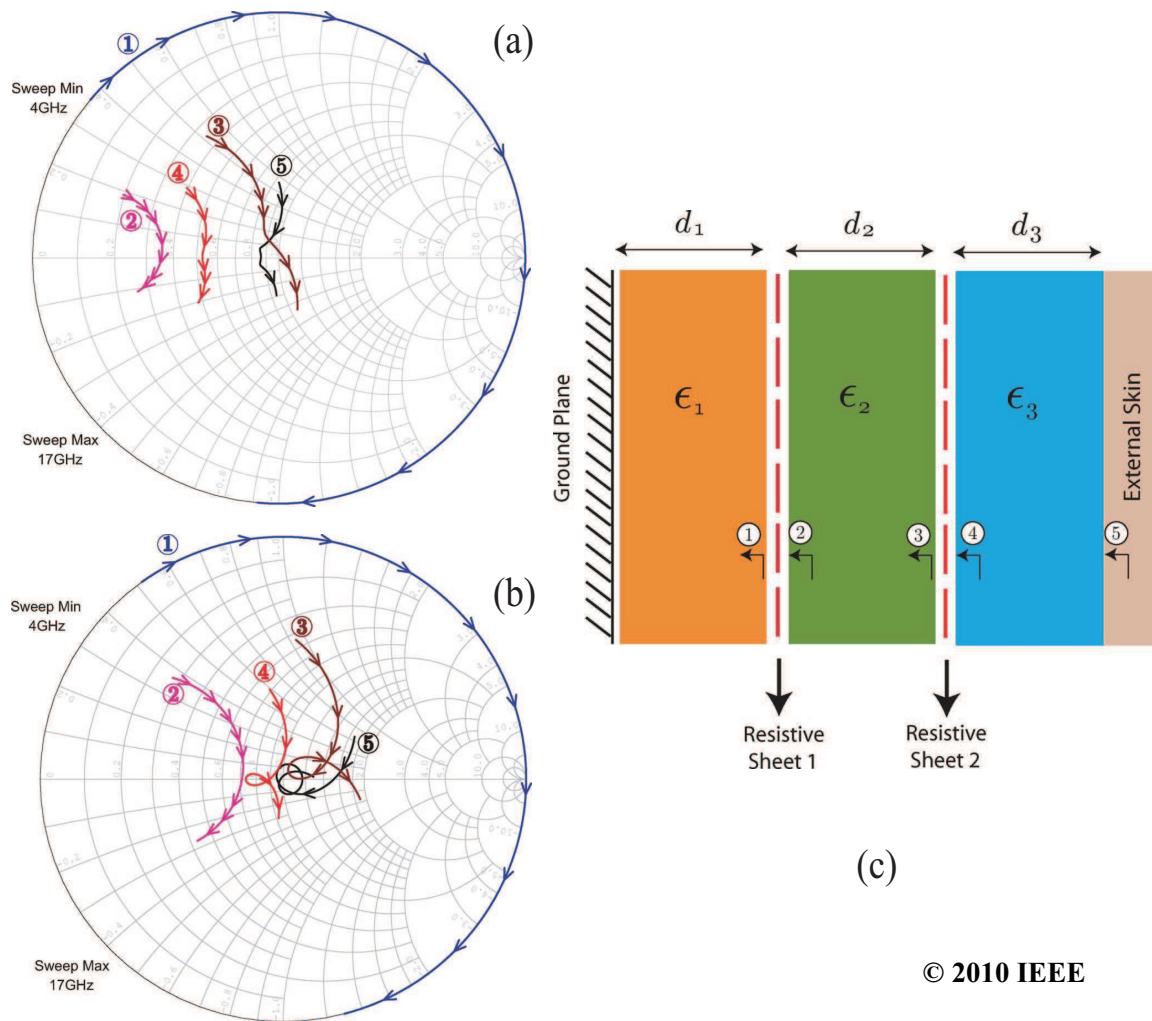


Figure 2.8. Frequency responses when building up a Jaumann absorber in the Smith chart. (a) TE and (b) TM polarization under 45° oblique angle of incidence. Each colored locus represents the input impedance after adding an FSS or dielectric in (c) Jaumann absorber structure. Adapted from [36].

2.3 FSS-Inspired Circuit Analog Absorbers

Planar electromagnetic (EM) absorbers have been used in a variety of wireless applications to reduce EM interference. Under this category, the Salisbury absorber or the Jaumann layers [1] were invented based on the principle of destructive interference and usually consist of homogeneous resistive films and quarter-wavelength spacings. These homogeneous resistive sheets can be further patterned into periodic arrays namely FSSs to further enhance the bandwidth-to-thickness ratio.

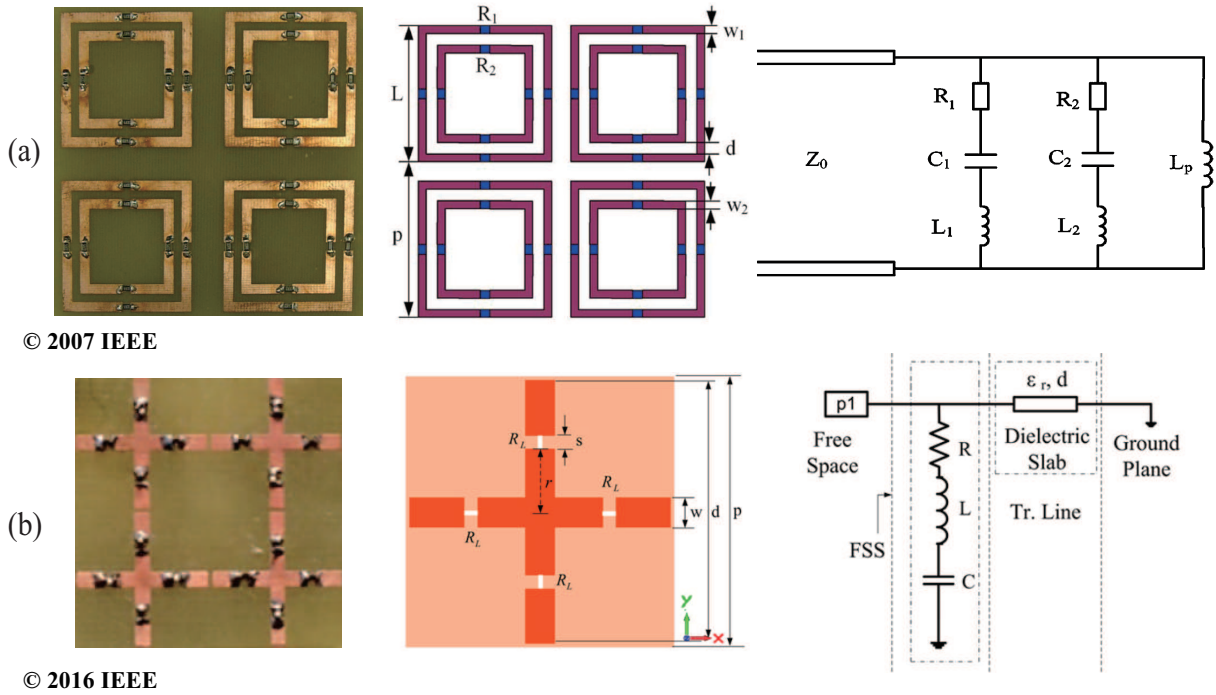


Figure 2.9. Synthesis for surface resistances with high-frequency lumped resistors. Unit cell in correspondence to the equivalent circuit models for (a) double square-loop FSS [38]; (b) cross FSS [37].

2.3.1 Embedding Surface Resistance

A typical CA absorber is an assembly of FSS layers and dielectric spacers on top of a metal ground. Equivalent circuit modeling has been discussed in the previous sections for lossless FSSs. However for CA absorbers, adding losses in a controlled manner and taking them into consideration at the modeling stage is essential. There are two existing approaches to fabricate a resistive FSS array, namely by soldering lumped RF resistors or using a thin layer of lossy conducting material.

Lumped RF Resistor

High-frequency resistors can be soldered at specified positions on each metallic FSS element, as shown in Fig. 2.9 [37,38]. This enables straightforward synthesis for desired resistances in the corresponding equivalent circuit branches. The dimensions of the unit-cell geometry are configured based on the equivalent reactive components independently, thus the design approach can be significantly simplified.

2.3 FSS-Inspired Circuit Analog Absorbers

Since these lumped resistors must be specially fabricated to avoid parasitic effects and customized for specific resistances, the cost is high. Furthermore, thicknesses of lumped RF resistors are not negligible, and they add to the calculation of the bandwidth-to-thickness ratios. For high frequency applications, it is also difficult to obtain lumped resistors that fit the small unit-cell size of an FSS.

Resistive Ink

In contrast to lumped RF resistors, surface resistance also can be introduced by using a thin layer of resistive material, which can be obtained for example by silk-printing with lossy ink as illustrated in Fig. 2.10. The advantages of this technique include negligible FSS thickness, light weight, flexibility and relatively low cost for applications in the microwave frequency range. Nonetheless, as both reactive and resistive elements are inter-dependent, the difficulty in optimization is significantly enhanced. Moreover, microfabrication technologies do not well accommodate the commonly used resistive inks for silk-printing in the terahertz frequency range.

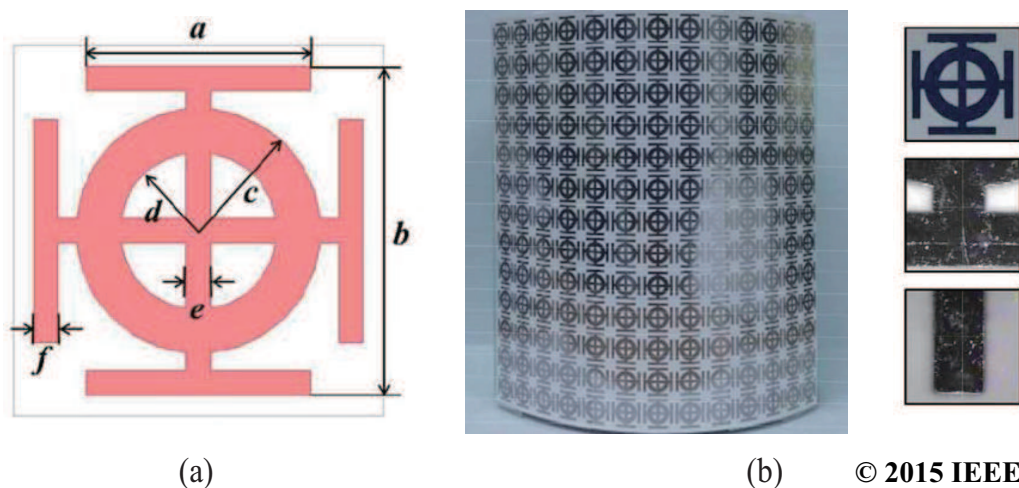


Figure 2.10. Introducing surface resistance by silk-printing with silver nanoparticle ink. (a) Unit-cell pattern; (b) fabricated flexible FSS on thin PET sheet with unit-cell inspections [39].

2.3.2 Evaluation Criteria

The total energy of an impinging EM wave can be divided into reflection, transmission and absorption. From the perspective of energy conservation, to improve the performance of a CA absorber over a metal ground, the reflection should be suppressed considering that there is no transmission through such a metal-backed structure. In other words, in this case, absorption can be evaluated by the reflection coefficient alone. In addition to the bandwidth and absorption level, the total thickness of the realized absorber also needs to be taken into consideration.

For comparison purpose, the commonly used levels of absorption are at 10 dB or 20 dB which respectively correspond to 90% or 99% power absorption. Other considerations are the following:

- The operation bandwidth BW must always be evaluated in ratio:

$$\text{BW} = \frac{f_H - f_L}{(f_H + f_L)/2}, \quad (2.7)$$

where f_H and f_L are the upper and lower boundaries for the operation frequency range at a specified level of reflection as shown in Fig. 2.11;

- The total thickness h_L must be normalized:

$$h_L = \frac{d}{\lambda_L}, \quad (2.8)$$

where d is the realized thickness in absolute scale, and λ_L is the free-space wavelength at the lowest operation frequency.

There is a trade-off between the relative bandwidth, the absorption level and the normalized thickness. For performance evaluation of an absorber, a comprehensive criterion is required. The Bode-Fano criterion in the transmission line theory indicates the optimum result that can be achieved for a given structural complexity. It provides a benchmark against practical designs for comparison purpose [23]. On this basis, the minimal achievable thickness of a non-magnetic multilayer absorber can be estimated based on a given reflection coefficient curve [31]:

$$\left| \int_0^\infty \ln |\rho(\lambda)| d\lambda \right| \leq 2\pi^2 \sum_i d_i, \quad (2.9)$$

where ρ is the reflection coefficient as a function of the wavelength λ , and d_i is the thickness of the i -th dielectric layer. The above relationship effectively enables a fair

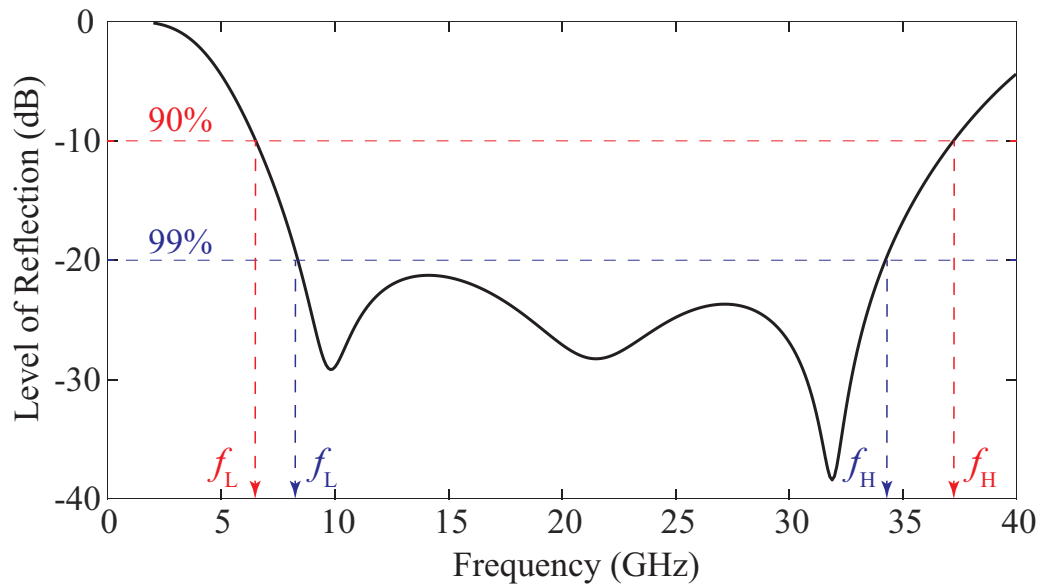


Figure 2.11. Absorber performance at specified absorption levels. The reflectivity of -10 dB and -20 dB respectively indicates 90% and 99% power absorption of the incident wave.

comparison between a thinner absorber of narrower bandwidth and a thicker absorber of broader bandwidth by calculating the proximity to their physically achievable minimal thicknesses.

2.3.3 Experimental Setup for Frequency Response Measurement

The simulated absorption performance of a CA absorber can be verified in an anechoic chamber by measuring the reflection coefficient either with a bi-static or mono-static configuration. A metallic plate of the same size as the testing sample is used for referencing purpose. Since the unit-cell geometries for the vast majority of absorbers are symmetric and thus insensitive to polarization, the measurement mainly focuses on the frequency responses under normal and oblique angles of incidence [40].

Bistatic Measurement

As shown in Fig. 2.12, the fabricated absorber is placed on the symmetry axis between a pair of horn antennas which are equally tilted with a specified angle. The surroundings should be covered with pyramidal foam absorbers to avoid interference from the equipment, holders and walls. The results for TE and TM modes can be obtained by setting the shorter or longer edges of the horn antennas parallel to the horizontal plane [41].

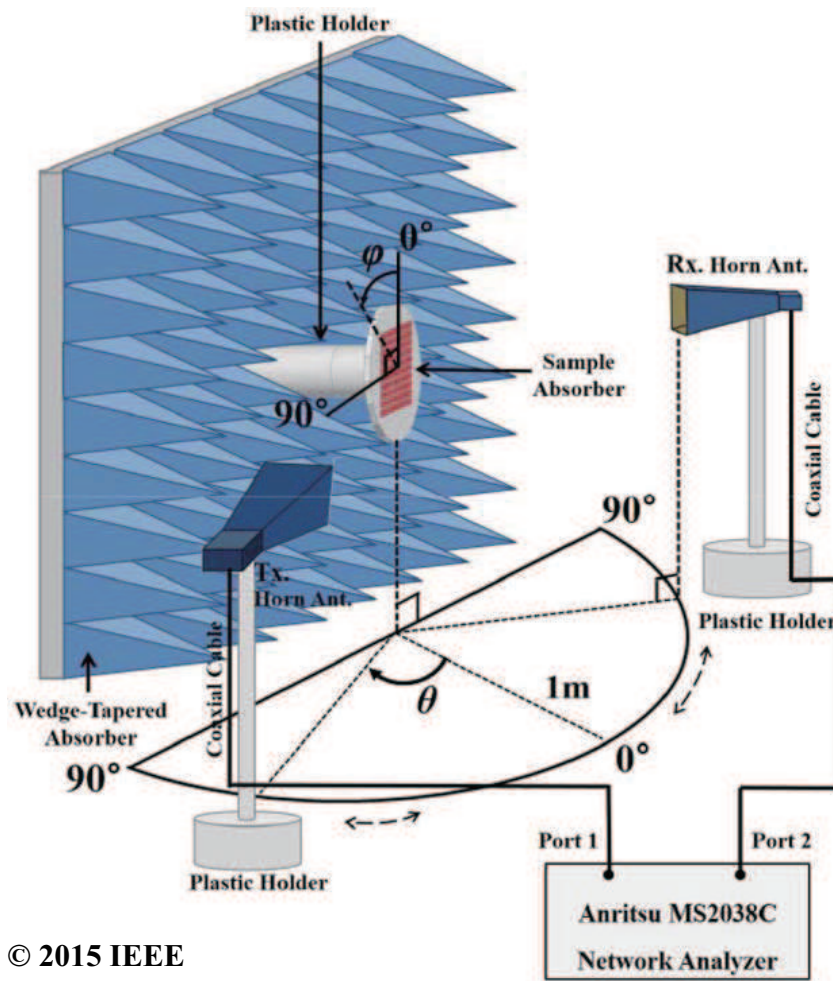


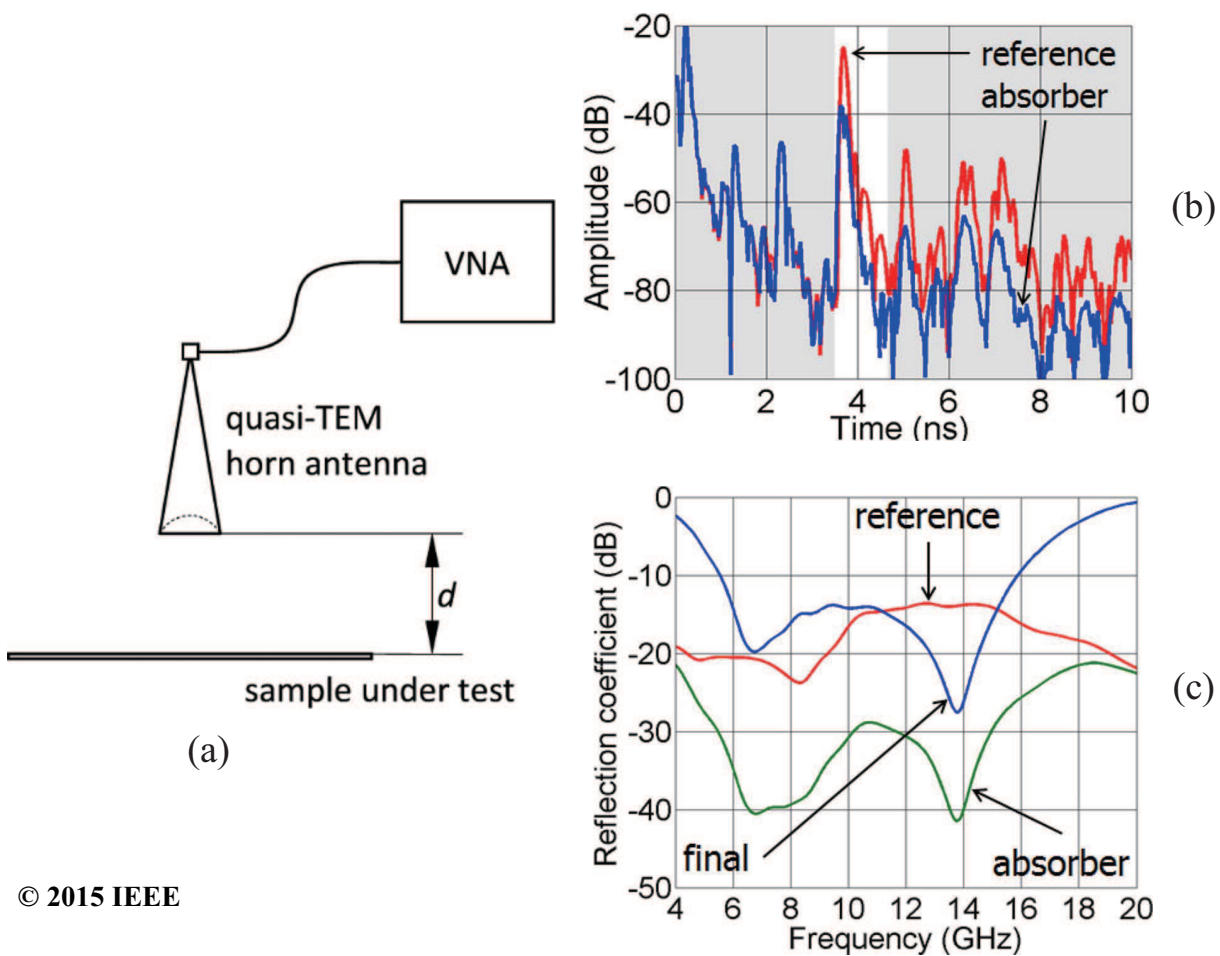
Figure 2.12. Bistatic measurement. A pair of horn antennas are placed on the circumference of a circle, and the sample under test is located in the center of this circle. Both antennas are symmetrically aligned for their maximum gain directed toward the sample along the radius to ensure an effective path for obliquely incident EM wave from the transmitter to the receiver [39].

It should be noted that ideally the absorber sample must be placed in the far-field region of the antennas, i.e. at a distance larger than

$$d = 2D^2 / \lambda_{AH}, \quad (2.10)$$

where D is the longer dimension of the absorber sample, and λ_{AH} is the wavelength at antenna's highest operation frequency. In practice, the calculated value is likely to be unrealistically large and a compromise has to be made considering the height or width of the anechoic chamber.

The data post-processing is carried out by normalizing the reflection coefficient of the absorber relatively to the metallic reference.



© 2015 IEEE

Figure 2.13. Monostatic measurement. (a) A typical setup including a vector network analyzer (VNA), a coaxial cable, a horn antenna with dielectric lens and a supporting platform; (b) time-gating at a proper position and with a reasonable width; (c) final result as a ratio of reflection coefficients between the sample and the reference [39].

Monostatic Measurement

If there is only one antenna available or insufficient space in the anechoic chamber, a mono-static setup as illustrated in Fig. 2.13 (a) can be applied. To mitigate beam diffraction, a dielectric lens is typically placed in front of the horn antenna to flatten the phase fronts. In most cases, the reflected wave is weaker than the level of undesired reflections from the surroundings. Thus, a time-gating method has to be adopted for post-processing. The window position can be decided based on the distance between the antenna and the sample under test, with an additional transit time in the coaxial

cable, whilst the gate width can be chosen based on the positions of obstacles in the surroundings and the requirement on resolution.

The primary disadvantage of this mono-static schematic is the incapacity of measuring frequency responses under obliquely incident EM waves. Although the far-field condition is not critical for such a setup, the lens must be specially designed, fabricated and calibrated. Possible distortion of the frequency response curve caused by time gating should be mitigated through a thorough analysis of the time scales and distances in the experimental setup.

2.4 FSS-Inspired Reconfigurable Filters

Filters are among the most important applications for FSS-based structures. They aim for maximizing the level of transmission in the passband whilst reflecting the out-of-band energy. They are widely used in wireless communications systems and are complementary to signal processing techniques that are associated with aliasing effects. Without significantly increasing the number of design parameters, multiple identical FSS layers can be stacked to achieve a high-order filter with enhanced bandwidth and steep transitions. However, in many applications, a high selectivity, i.e., a high Q -factor that can be tuned across a wide frequency range is required. Such reconfigurable filters allow shifting of the operation frequency in a feasible range via electrical or mechanical approaches. It should be noted that adapting a microwave design to the terahertz spectrum is not as straightforward as scaling down all its geometric dimensions, because the material attributes and fabrication processes become different. More importantly, varactors for terahertz applications are challenging to fabricate and come with high power dissipation. Thus, thermal control on novel materials has been considered as an alternative approach. In the remainder of this section, a few types of reconfigurable bandpass filters from the literature are illustrated.

To adaptively cover a broad spectral range whilst maintaining high frequency selectivity, a series of FSS filters of large Q -factors operating at discrete frequencies can be arranged on a rotatable circular disk [42]. As shown in Fig. 2.14, an FSS patterned with orthogonal slots is adopted for narrowband filtering. Its operation frequency depends on the slot design. By sequentially embedding a series of these filters on a rotary switch, frequency reconfiguration can be achieved. Although its design principle

2.4 FSS-Inspired Reconfigurable Filters

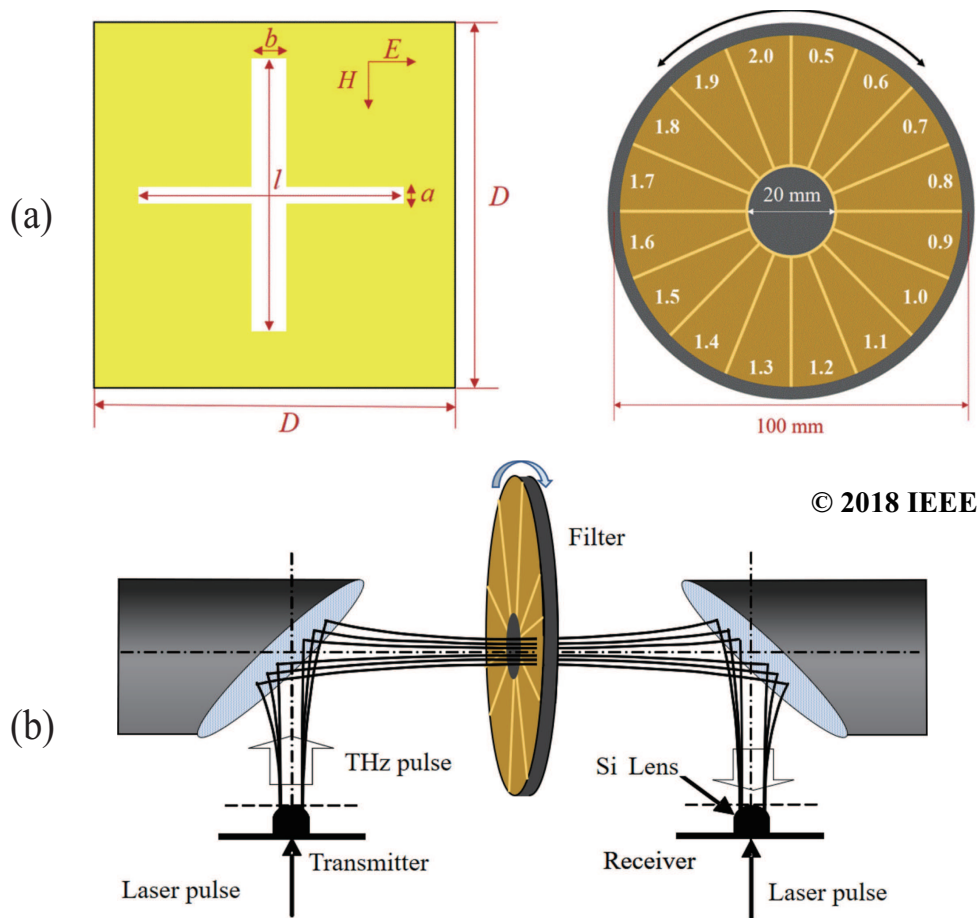


Figure 2.14. Design schematic and experimental configuration of high-selectivity terahertz filter. (a) Generic unit-cell geometry and overall assembly; (b) measurement setup [42].

is simple and straightforward, such tunability is limited to a series of pre-determined discrete frequencies rather than in a continuous spectrum sweep.

Another mechanical approach to obtain frequency reconfigurability is by adjusting the compression level of a three-dimensional spring FSS [15]. Equivalent circuit modeling still remains valid for this geometry as shown in Fig. 2.15. This design allows continuously tuning the operation frequency by mechanically compressing the spring array. In contrast to planar FSS structures, nonetheless, the circuit elements vary along with compression, which increases the complexity in analysis and synthesis. In addition, considering the challenges in fabrication, this design approach better suits the microwave frequency range.

A varactor is a diode with capacitance controlled by controlling a bias voltage applied between its terminals. Embedded on an FSS geometry, the varactors are used to adjust

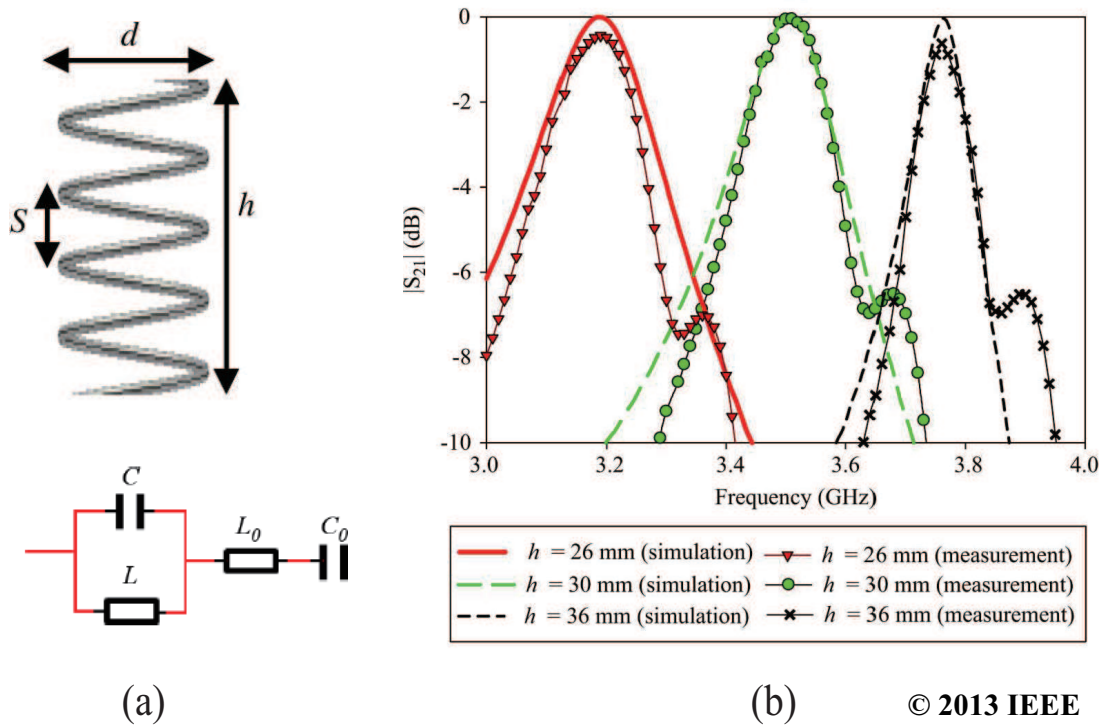


Figure 2.15. Spring geometry and frequency tunability. (a) Array element and its equivalent circuit model; (b) frequency shift via change in compression level [15].

the local reactance and thus manipulate the frequency response. The zeros and poles of the equivalent circuit branches for an FSS-based filter can be changed correspondingly, which determine the passband or stopband. The primary challenge for designing an active FSS-based filter is embedding a dedicated bias network on the periodic array, especially when there are multiple FSSs. One possible solution proposed in [43] was to include a grid pattern in all unit cells as illustrated in Fig. 2.16. These grids in combination with the metallic vias were not only part of the filter geometry, but also provided bias for the varactors. Although a tuning range of 8.8% fractional bandwidth was achieved in [43], the transmission coefficients measured in a parallel-plate waveguide show that the insertion loss within the passband amounted up to 6 dB, which was mostly explained by the ohmic loss of the diodes in the varactors. Along with an increase in the bias voltage, the insertion loss became lower due to a smaller series resistance as indicated in Fig. 2.17 (b) [43].

A design adopting vanadium dioxide (VO₂) phase-change material (PCM) which has a transition between an insulator and metal phase at a practical temperature was reported [34]. As illustrated in Fig. 2.18 (a) and (b), the FSS array was surrounded by an

2.4 FSS-Inspired Reconfigurable Filters

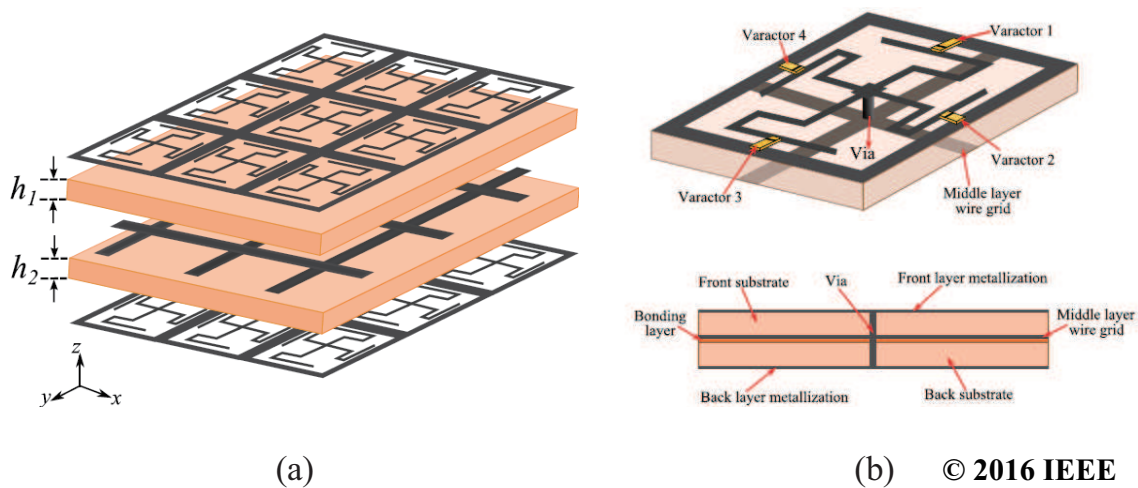


Figure 2.16. FSS-based varactor-tunable bandpass filter. (a) Exploded view for multi-layer FSS; (b) perspective and cross-sectional views for placement of varactors and vias for the bias network [43].

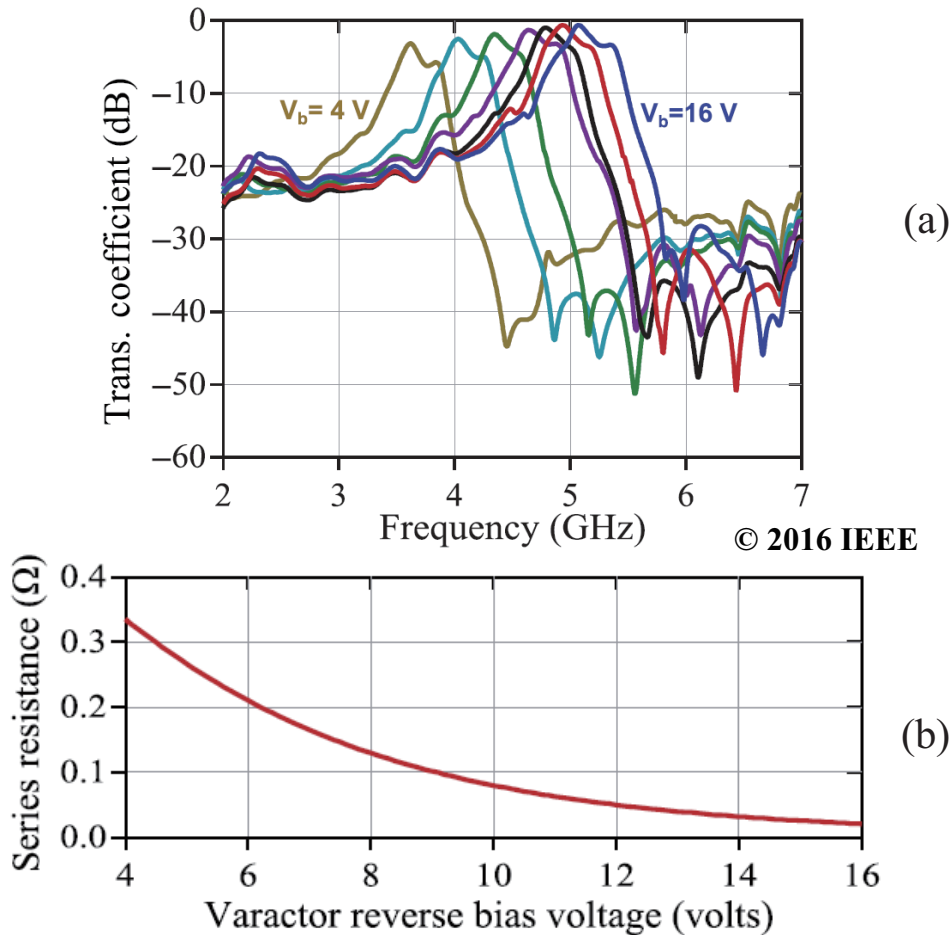


Figure 2.17. Passband reconfiguration and insertion loss of a varactor-based FSS spatial filter. (a) Measured transmission coefficients in the tuning range under normal incidence; (b) relationship between bias voltage and series resistance of the varactors [43].

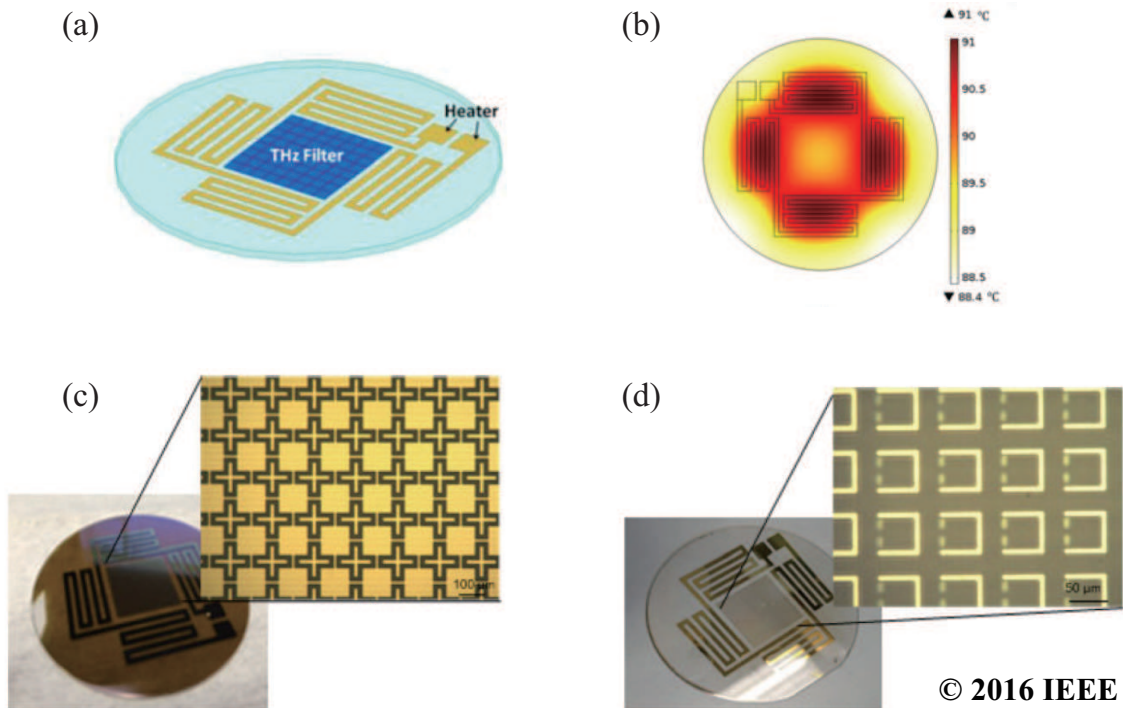
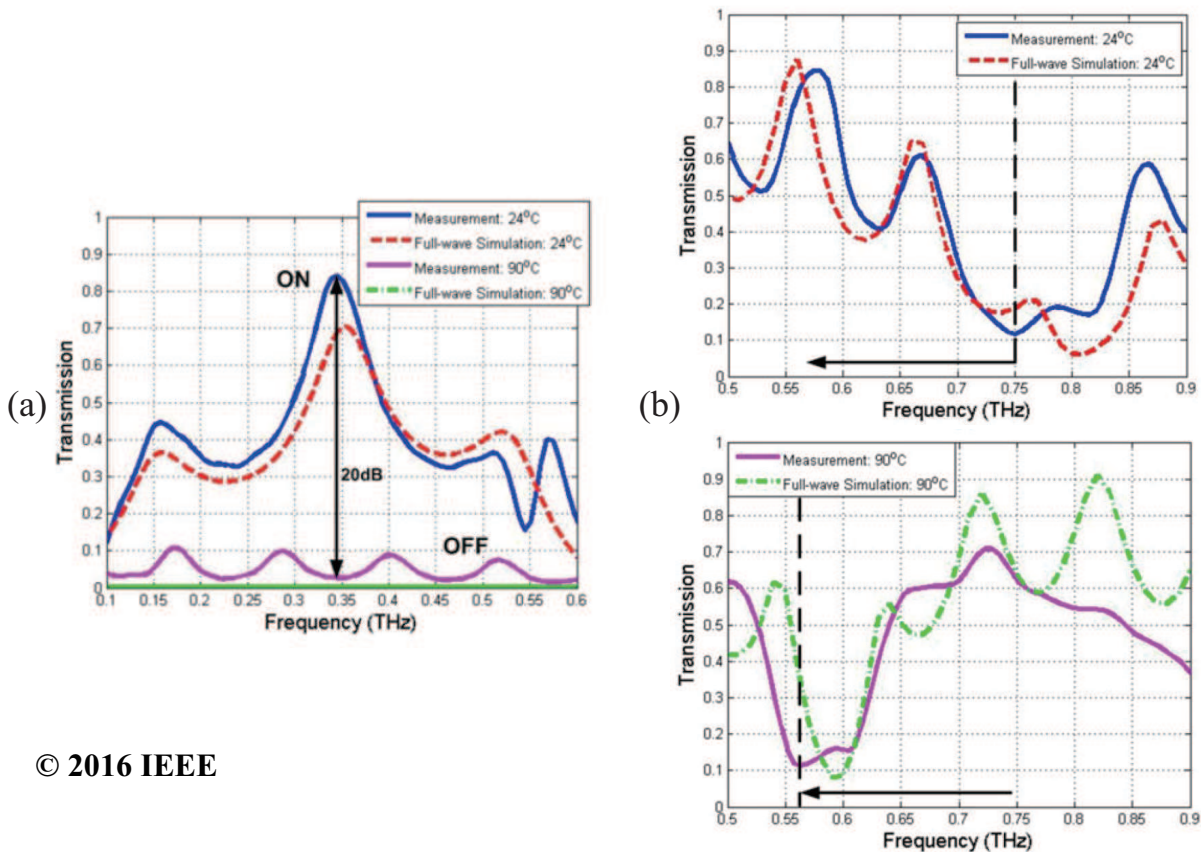


Figure 2.18. Bandpass and bandstop FSSs using phase-change materials with integrated meander loop heater. (a) Generic design schematic; (b) temperature contour of the integrated meander loop heater; fabricated (c) broadband on/off bandpass filter and (d) frequency-reconfigurable bandstop filter [34].

integrated meander loop heater that was controlled by a voltage. The types of filtering are determined by the unit-cell geometries, as the on/off bandpass filter and the tunable bandstop filter respectively illustrated in Fig. 2.18 (c) and (d).

Switching of the bandpass filter in Fig. 2.19 (a) is clear at different temperatures, and a high transmission at 0.35 THz can be observed at its ON mode. The insertion loss is mainly from the non-ideal conductive material. The very limited usable bandwidth, however, does not support the claim of a broadband design. The bandstop filter in Fig. 2.19 (b) shows a narrow operation bandwidth of 30.77%. The frequency responses of these proposed filters may be improved by further optimizing the unit-cell geometries, and selecting novel materials for the FSS array and the substrate [34].



© 2016 IEEE

Figure 2.19. Frequency responses for reconfigurable bandstop and bandpass filters. (a) On/off switch bandpass filter; (b) frequency tunable bandstop filter [34].

2.5 Summary

This chapter has summarized the relevant theories, design principles and existing techniques for FSS structures. The Babinet's principle and scalability can be used to reduce the number of design variables and thus improve the efficiency in global optimization. Equivalent circuit modeling is the most widely used analysis and synthesis approach for FSS-based structures, whilst the transmission line theory provides a simple but effective way of modeling multilayer structures. The theory of small reflections can be adapted for calculating the S -parameters and further exploited for oblique incidences. In addition to the analytical formulas and equations, the Smith chart is also useful for synthesizing multilayer structure by qualitatively manipulating its input admittance locus. The existing absorbers in the literature have been discussed in terms of the surface resistance, evaluation criteria and experimental setup. The reconfigurable filters

mostly adopt varactors in the microwave spectrum. However, special materials are required for the tunable terahertz filters due to the small unit cell size.

Chapter 3

Single-FSS-Layer Absorber Adopting Impedance Matching Superstrate

CIRCUIT analog (CA) absorbers embedding a lossy frequency selective surface (FSS) have gained increasing popularity in applications such as high-quality telecommunication systems and high-resolution navigation devices. The bandwidth-thickness trade-off is fundamental to the design of thin absorbers. In this chapter, we challenge the common belief that adding a dielectric superstrate will enlarge the bandwidth at the cost of increased thickness. It is firstly demonstrated using lumped circuit considerations that a wider relative operating bandwidth can be achieved with a thinner absorber including an impedance matching cover. By adopting this dielectric superstrate, we further show on the basis of full-wave simulation that the highest bandwidth ratio (BWR) at 10 dB absorption can be increased from 1:3.54 to 1:6.94, with the normalized thickness being reduced from $0.0920\lambda_L$ to $0.0906\lambda_L$ (including superstrate). Restricted by readily available materials, an experimentally validated design obtains a BWR of approximately 1:5.32 at 10 dB absorption for a figure of merit of 88.26%. This performance is superior to existing designs with more complicated FSS patterns.

3.1 Introduction

Electromagnetic absorbers have found diverse applications, such as improving electromagnetic compatibility (EMC) of integrated circuits, reducing backscattering and eliminating electromagnetic interferences (EMI) in complicated environments or even being adapted as chip-less radio frequency identification (RFID) tags [18,35,37]. There primarily exist three interdependent criteria to evaluate an absorber, namely its relative bandwidth, level of absorption, and normalized thickness. For simplicity in comparison, a figure of merit measures how close an absorber approaches the theoretical minimal thickness [31] for a given absorption performance [26,44]. In practice, additional criteria including complexity, flexibility, robustness, sensitivity under oblique incidence, and cost-effectiveness [45] should also be considered.

Compared to bulky wedge-tapered absorbers, metal-backed planar absorbers are widely considered as a trade-off between high performance and low profile [8]. Under this category, the Salisbury absorber or the Jaumann layers [1] were invented based on the principle of destructive interference and usually consist of homogeneous resistive films and quarter-wavelength spacings. However, their thickness-to-bandwidth ratio is far from the theoretical limit. This has motivated the development of CA absorbers consisting of lossy periodic arrays to provide low- Q -factor resonances. To avoid parasitic effects, resistors specially made for high-frequency applications were often employed to introduce ohmic loss in metallic FSSs [26,37,38,46,47], thus increasing manufacturing complexity and cost. As an alternative, flexible and lightweight lossy FSSs can be created from resistive inks made of graphene, conductive polymers or silver nanoparticles [21,35,39,48].

Based on such lossy layers, a large number of existing broadband absorber designs in the microwave spectrum have focused on exploring various patterns of FSS [8–12,24]. The absorption bandwidth can indeed be enlarged by adding more resonances derived from more complex FSS shapes. Nonetheless, complicated coupling existing among resonators could severely hinder accurate analysis and preclude rigorous synthesis. Further to the bandwidth consideration, recent studies revealed that the addition of an outermost dielectric slab as superstrate can help maintaining performance for oblique incidence by reducing the frequency shift and mitigating the absorption level deterioration [25,36]. Due to concerns of excessive thickness [46], however, the hidden benefit on bandwidth arising from the additional superstrate has neither been thoroughly investigated nor experimentally verified.

In this chapter, the author challenges the common belief that adding a dielectric superstrate will enlarge the bandwidth at the cost of increased thickness. Section 3.2.1 adopts a simple resistive square as unit cell geometry for demonstration purpose, and its circuit configuration is optimized using a genetic algorithm (GA). The insight into the circuit equivalence enables exhaustive exploration of the potential of the chosen topology. The synthesis based on the Smith chart is shown in Section 3.2.2 where the superstrate acts as an impedance matching transformer that effectively improves the absorption performance while reducing the overall absorber thickness (including superstrate). Section 3.3 examines an experimentally validated design which uses available dielectric as the superstrate and resistive ink for the FSS. The measured result is compared to the best single-FSS-layer absorbers in the literature. The comparison highlights a highly competitive performance, namely a BWR of approximately 1:5.32 at 10 dB absorption for a figure of merit of 88.26%, in spite of the simplicity of the design.

3.2 Absorber Design with Dielectric Superstrate

When interacting with an object in free space, the total energy of an incident electromagnetic wave is divided into 3 parts, namely reflection, transmission and absorption. The design principle for electromagnetic absorbers can be built upon the law of energy conservation, where the power absorption will be maximized given that the transmission and reflection are minimized. For planar absorbers whose transmission path is terminated with a metal ground, the absorption performance can be solely determined by the level of reflection, which motivates the adoption of impedance matching techniques in the modeling using transmission line (TL) theory. On such a basis, a dielectric superstrate is applied on top of the classic single-FSS-layer absorber as an adapter, and the Smith chart is used for qualitative analysis.

Figure. 3.1 illustrates the investigated structure, which consists of a simple resistive square patch array in-between a metal-backed substrate and a dielectric superstrate. The central operation frequency is primarily determined by thickness and relative permittivity of the substrate. The thin superstrate not only contributes to the overall impedance matching to the free space, but also can protect the resistive FSS from the UV light, moisture and abrasion. In the following, we will demonstrate the performance benefits of this outermost dielectric cover, and explain the physical mechanism

3.2 Absorber Design with Dielectric Superstrate

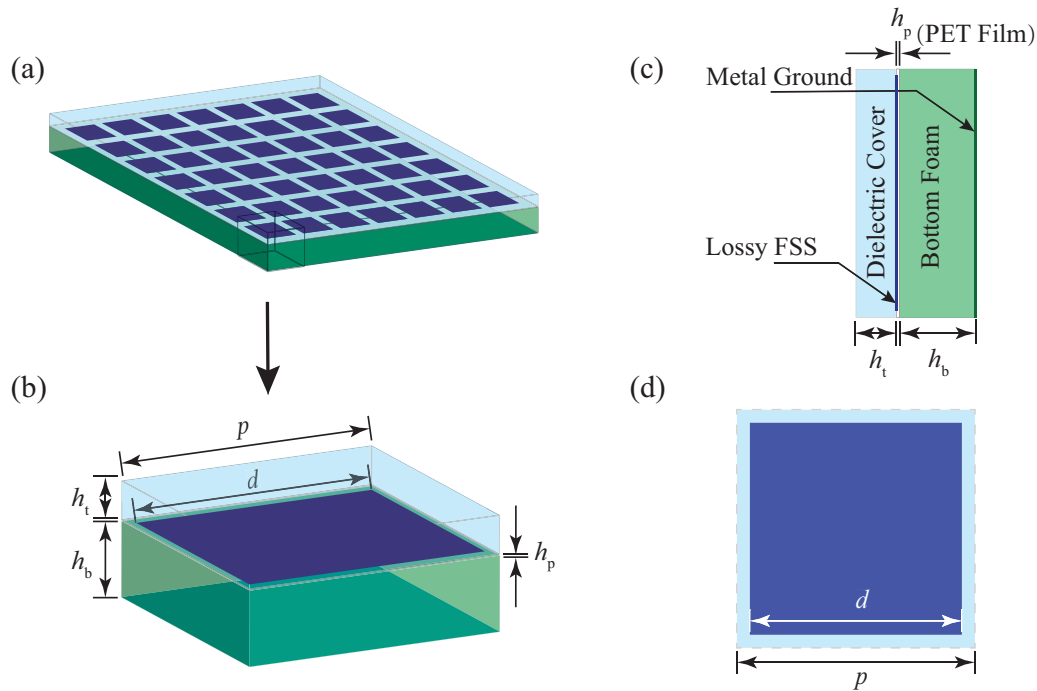


Figure 3.1. Schematics of a single-FSS-layer absorber with dielectric matching cover.

(a) Perspective view of the absorber; (b) unit-cell; (c) side view, and (d) top view. A PET (polyethylene $\epsilon_p = 2.25$) film supports the patterned resistive layer.

behind this improvement through equivalent circuit modeling and impedance matching.

3.2.1 Equivalent Circuit Modeling and Full-wave Simulation

The square patch, as the most fundamental unit cell geometry, corresponds to the simplest FSS equivalent circuit model, namely RLC in series as illustrated in Fig. 3.2. The values for RLC elements can be considered as frequency-independent within the spectrum of interest from 2 GHz to 25 GHz. The patch edge length d and the gap width $g = p - d$ are considered as determinant variables when synthesizing reactive components, whereas the distance between the FSS and the metal ground has little impact on the equivalent inductance or capacitance [49]. Under normal incidence, the reactive elements in the equivalent circuit remain unchanged with regard to polarization because of the intrinsic symmetric feature of square unit cells. Nevertheless, the constraint on symmetry also gives rise to slight interdependence between L and C . In addition, a dielectric cover shielding the FSS will also affect the reactive components in accordance

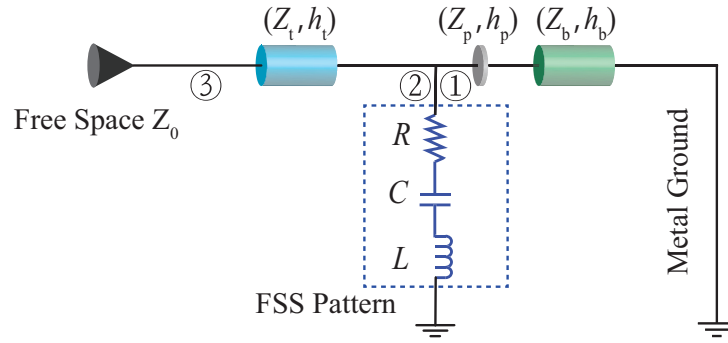


Figure 3.2. Equivalent circuit model of a single-layer CA absorber. The transmission line sections correspond to the layered dielectric materials with assigned characteristic impedances in association with their relative permittivities. The numbers along the transmission line positions indicate the steps in developing the admittance loci in the following subsection.

to its relative permittivity. The series resistance can be evaluated through an empirical formula [21]:

$$R = (1 + \zeta)R_s \left(\frac{p}{d}\right)^2, \quad (3.1)$$

where R_s is the surface resistance of the resistive layer, and ζ is assigned to 5% as an empirical correction factor considering the fringing effect on current distribution.

Based on the obtained circuit model, the genetic algorithm (GA) toolbox [50] can be employed with recommended values for initial parameters in Matlab™ to seek for the minimal thickness upon the predefined -10 dB bandwidth ratio (BWR). According to Fig. 3.3, the topology with superstrate can significantly help reduce the thickness for a predefined BWR starting at 2:1, as well as increase the largest BWR achievable. It has been cross-validated through exhaustive searches that the GA results are accurate and reliable. Alternative optimization algorithms can be used to determine the global optimum for the problem under consideration.

To approach widest possible BWR in practical settings, additional considerations are necessary. These include limitations due to the interdependence between reactive components in the square patch geometry, as well as due to diffraction effects linked to the finite unit cell size. Taking into account these constraints, the absorber is synthesized in the full-wave electromagnetic solver HFSS™, on the basis of the GA optimized circuit attributes (e.g., layer thicknesses) and S -parameter fitting. The corresponding equivalent RLC values and the transmission line characteristics for this best realizable design are tabulated in Table 3.1, whilst the geometric dimensions and material parameters are listed in Table 3.2. The broadest bandwidths realizable for the configurations without and with a top dielectric cover are 1:3.54 and 1:6.94 respectively, as shown in Fig. 3.4.

3.2 Absorber Design with Dielectric Superstrate

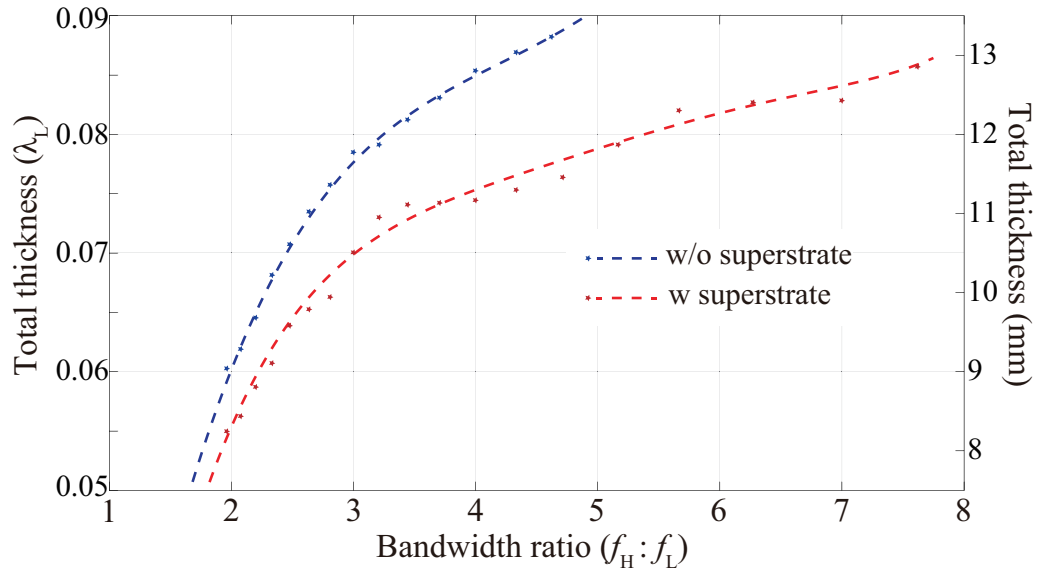


Figure 3.3. Bandwidth-thickness relationship for GA optimized topologies without and with dielectric superstrate. The left vertical axis indicates the normalized thickness in λ_L that corresponds to the wavelength at the lowest operation frequency for 10 dB absorption level. Assuming f_L is 2 GHz, the absolute thickness in mm can be calculated and measured on the right vertical axis. The scatter plots of the raw data are fitted with polynomial regression lines for visual aid.

Table 3.1. Equivalent RLC values and transmission line attributes for both topologies.

Absorber	R (Ω)	L (pH)	C (fF)	Z_t (Ω)
Without superstrate	225.44	1140.04	464.81	N/A
With superstrate	163.53	203.40	584.65	190.90

The thicknesses of these absorbers are $0.0920\lambda_L$ and $0.0906\lambda_L$, respectively. The comparison suggests that enhanced bandwidth and lowered profile can be achieved simultaneously via proper implementation of dielectric superstrate. To match the maximal BWR of 1:3.54 of its counterpart, the total thickness of an absorber with a dielectric cover can be reduced by $0.0121\lambda_L$ or 1.82 mm.

3.2.2 Impedance Matching Analysis

This subsection supplements the previous one with a thorough analysis on performance improvement with a dielectric superstrate. The efficiency in optimization can

Table 3.2. Dimensions and material parameters for both topologies. ϵ_t is the relative permittivity of the dielectric superstrate.

	h_t	h_b	p	d	ϵ_t	R_s (Ω/\square)
without superstrate	N/A	13.4	45.0	40.0	N/A	160
With superstrate	4.3	8.9	21.1	19.1	3.9	125

All dimensions above are in mm.

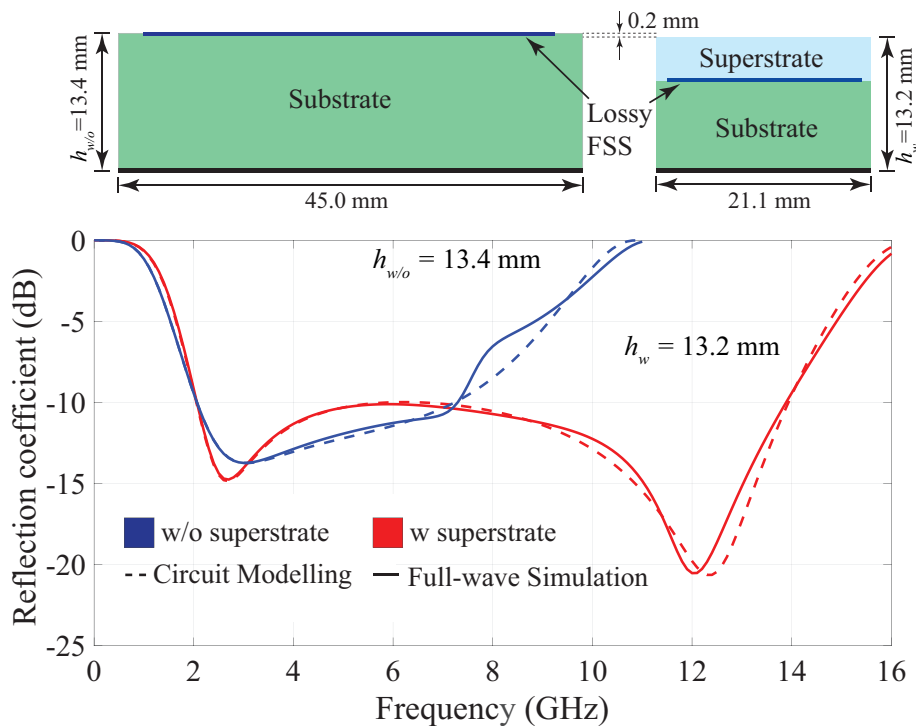


Figure 3.4. Optimization aiming at -10 dB level of reflection for single-layer CA absorbers without and with dielectric superstrate. With the lowest operating frequencies aligned at 2 GHz, the latter achieves significantly larger bandwidth with smaller thickness and miniaturized unit cell geometry. The $100 \mu\text{m}$ PET film is omitted for simplicity.

be enhanced by intuitively manipulating the loci that indicates the level of reflection in a specified frequency range.

Wideband absorption corresponds to a broad spectral range where the input impedance of the absorber matches the intrinsic impedance of free space, thus the reflection is suppressed to a given level. To better understand the effect of adding a impedance matching dielectric, the Smith chart which illustrates the frequency-dependent impedance

3.2 Absorber Design with Dielectric Superstrate

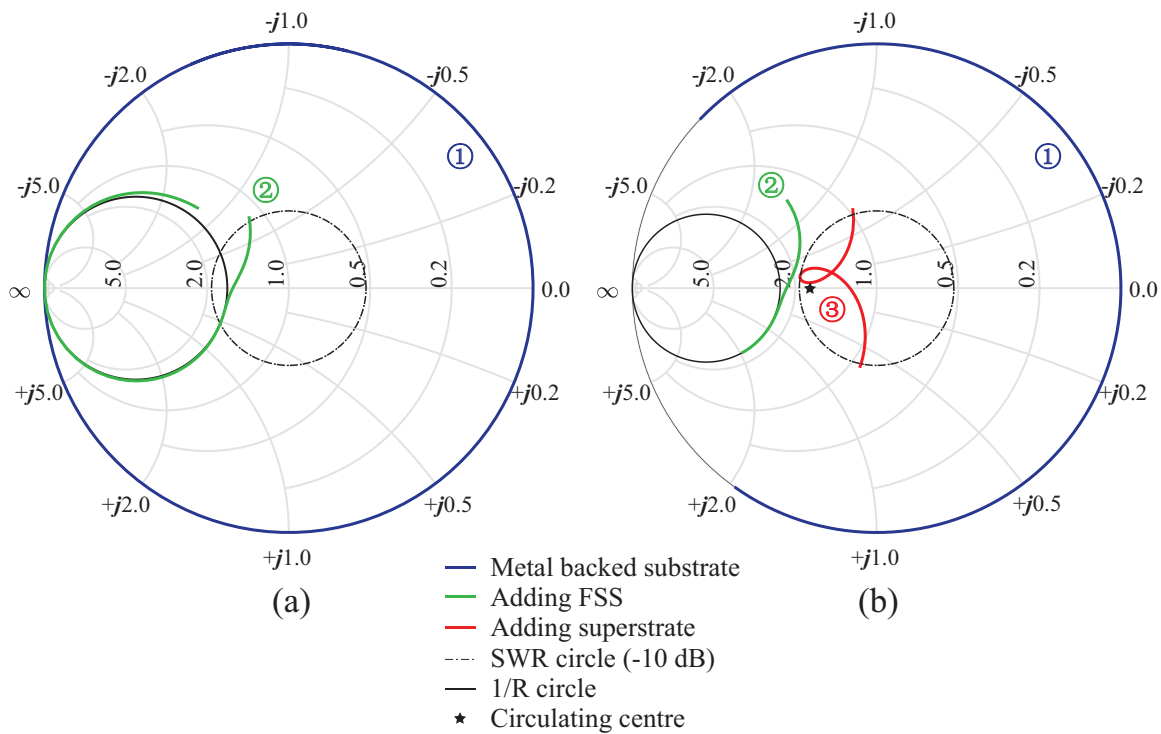


Figure 3.5. Admittance Smith chart for wideband impedance matching manipulation.

It shows the schemes for the optimized designs (a) without and (b) with dielectric superstrate. The loci span the frequency range from 2 to 14 GHz clockwise. The circled numbers refer to the corresponding transmission line positions in Fig. 3.2.

can be used for qualitative analysis [1, 21, 25, 36]. The absorption bandwidth can be estimated from the length and shape of the reflectivity locus captured within the standing wave ratio (SWR) circle that corresponds to a given level of reflectivity. More specifically, a broadband absorber would typically require a short locus with dense frequency distribution clustering around the center of the Smith chart.

To begin with, the input admittance Y_b associated with a metal-backed dielectric spacer is represented by loci denoted as ① in Fig. 3.5 (a) and (b). The circled number refers the corresponding position in the transmission line topology of a single-FSS-layer absorber as illustrated by Fig. 3.2. This input impedance is purely imaginary and located on the rim of the Smith chart. The length of the loci is in positive correlation with the electrical length of the substrate [1]. Since any metal-backed substrate of relative permittivity larger than that of free space would generate a longer curve for the same frequency range, a spacer with relative permittivity close to unity becomes the preferable choice.

Next, the admittance of the FSS, according to the lumped circuit model in Fig. 3.2, can be calculated as:

$$Y_{\text{FSS}} = \frac{R + j\frac{1-\omega^2 LC}{\omega C}}{R^2 + \left(\frac{1-\omega^2 LC}{\omega C}\right)^2}. \quad (3.2)$$

Since the resonance frequency $\omega_0 = 1/\sqrt{LC}$ of this FSS is located beyond the upper spectral boundary ω_H , the square patch exhibits a capacitive response. Owing to the series resistance, the real part \Re of the combined input admittance ② is scaled down from ① and approaches the conductance circle $1/R$:

$$\lim_{\omega \rightarrow \omega_0} \Re\{Y_{\text{FSS}} + Y_b\} = \lim_{\omega \rightarrow \omega_0} \Re\{Y_{\text{FSS}}\} = \frac{1}{R}. \quad (3.3)$$

On the other hand, the imaginary part of the total admittance increases, which leads to clockwise rotation and compression of the locus, according to: $\Im\{Y_{\text{FSS}}\} > 0$.

As an impedance matching transformer, the dielectric superstrate circulates the locus around its normalized admittance $Y_c = \sqrt{\epsilon_r}$. Therefore, trace ② in Fig. 3.5 (b) is further clustered into ③. The rotating angle at each operation frequency on the locus is in direct correlation with the electrical length of the superstrate, which can be deduced from its physical thickness and relative permittivity. Via proper manipulation in the Smith chart, reasonable estimations can be made to effectively reduce the effort on parametric study of the superstrate.

3.3 Experimental Validation and Comparison

The physical realization of an absorber design is limited by accessibility to materials. Therefore, to validate the consideration above, the optimal configuration needs further adjustment. To this end, the bottom dielectric spacer adopts a standard 6.4 mm thick PF4 foam ($\epsilon_t = 1.06$, $\tan\delta = 0.0001$) and the dielectric cover mounted on the FSS plane is a 3 mm Rogers RT6002 board ($\epsilon_t = 3.0$, $\tan\delta = 0.0012$). The surface resistance of a commercially obtained resistive layer printed on a PET sheet is $160 \Omega/\square$. On that basis, an optimal unit cell size p of 10.5 mm, and a patch size d of 10 mm are acquired through parametric studies. The absorption band for this configuration extends from 3.32 to 19.96 GHz, which is equivalent to 1:6.01 BWR with an overall thickness of $0.105\lambda_L$. In this design process, a margin of -1 dB is added to the reflectivity threshold to accommodate tolerances in material parameters and dimensions. As shown in Fig. 3.6, the

3.3 Experimental Validation and Comparison

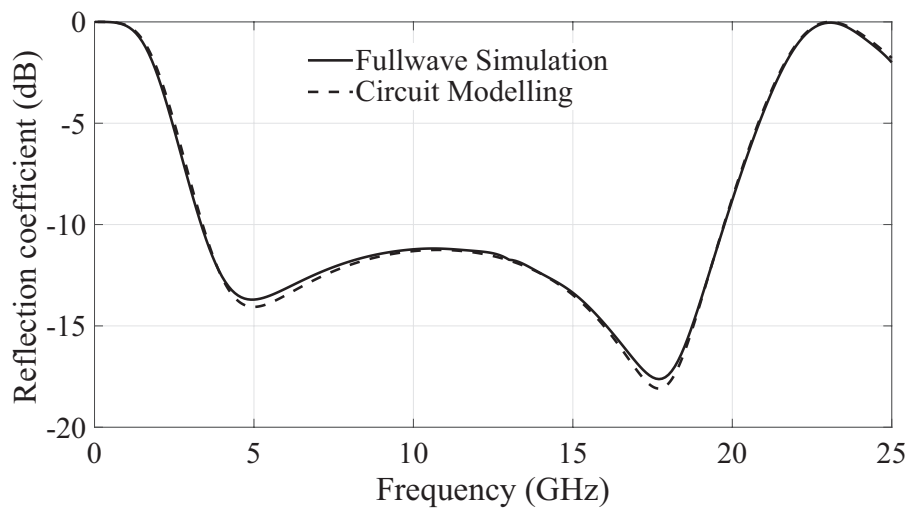


Figure 3.6. Reflection coefficients for the proposed design accounting for material availability. The total thickness, including 6.4 mm PF4 foam, 3 mm RT6002 dielectric cover and 0.1 mm PET sheet, equals to 9.5 mm.

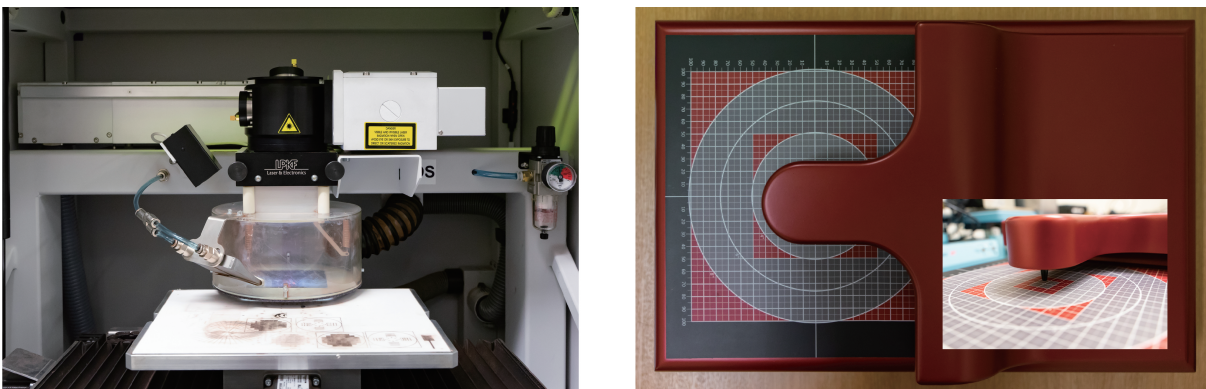


Figure 3.7. Equipment for the proposed absorber validation. (a) LPKF[®] laser machine for FSS patterning; (b) EddyCus[®] contactless platform for surface resistance measurement.

reflection coefficients obtained from the full-wave simulator HFSS[™] and the circuit modeler ADS[™] fit closely over the operation spectrum.

The core equipment tools used for absorber validation are shown in Fig. 3.7, including a LPKF[®] laser milling machine and a contactless surface resistance measurement platform EddyCus[®] TF Lab 2020. Figure. 3.8 shows the absorber before assembly. A zoom-in view depicts the laser-cut and silk-printed trails forming the patches on the resistive layer. The surface resistance has been adjusted to $195 \Omega/\square$ in simulation to

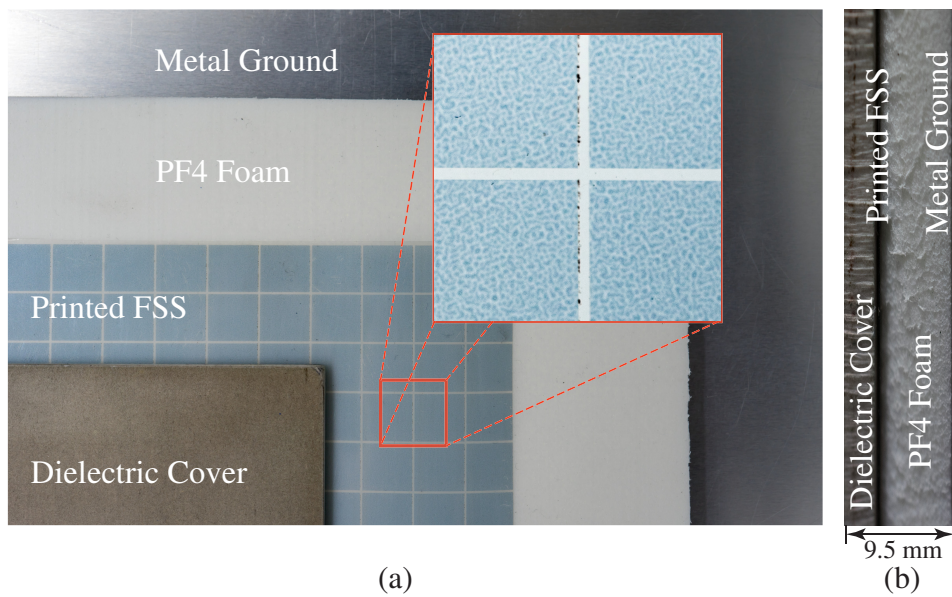


Figure 3.8. Exploded view of the fabricated absorber. (a) from bottom to top: metal ground, PF4 foam, FSS patterned on the PET film, and dielectric superstrate; (b) side-view.

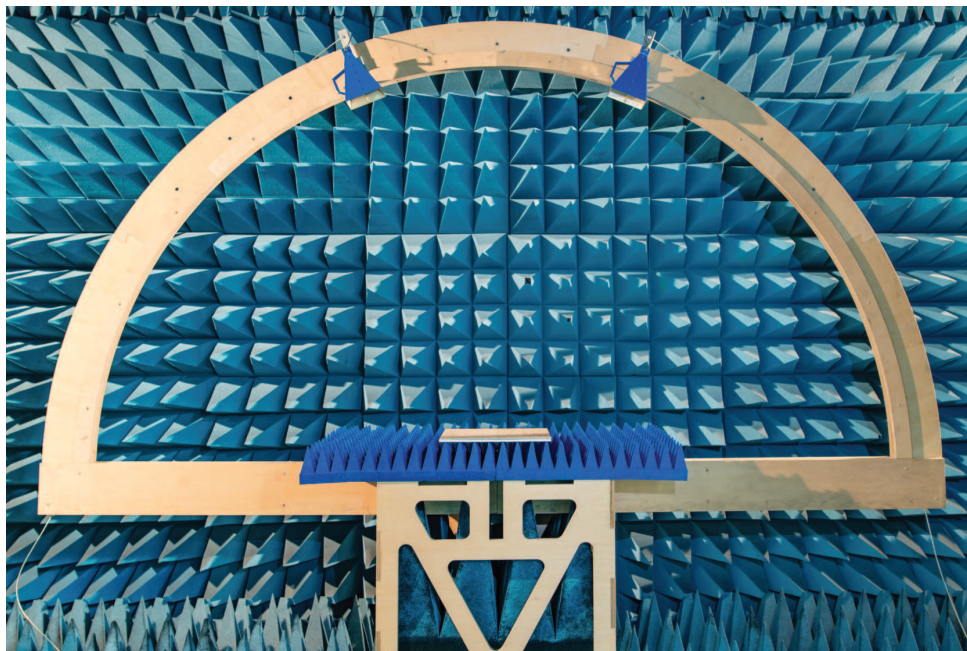


Figure 3.9. Experimental setup for absorption performance measurement. The sample size is 210 mm by 300 mm, and the radius of the arch is 1.35 m.

match a value found in the independent contactless measurement. For experimental verification of the absorbing performance, two wideband ridged horn antennas are symmetrically mounted on a wooden arch at a certain angle of incidence with the sample under test placed at the arch center as illustrated in Fig. 3.9. The reflectivity of the

3.3 Experimental Validation and Comparison

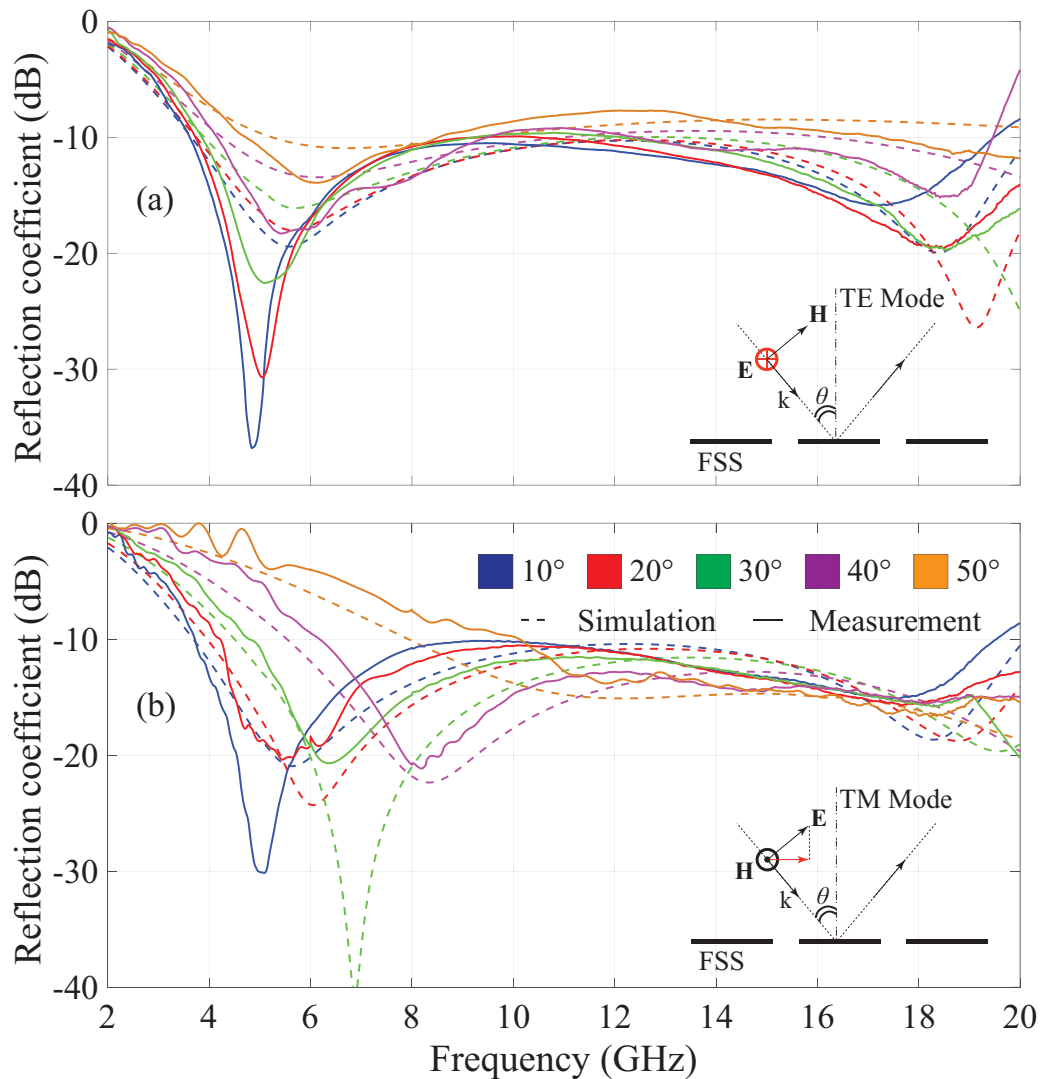








Figure 3.10. Measured and simulated reflection coefficients. (a) TE and (b) TM modes under oblique incidence up to 50 degrees.

absorber is measured by normalizing the bi-static transmission to a piece of metal reference of equal size. Although ideally the radius of the arch should extend beyond the far-field distance throughout the entire spectrum [40, 41], a realistic compromise has to be made considering the available anechoic chamber height. The measured BWR is 1:5.32 with a normalized thickness $0.117\lambda_L$, which is in agreement with the simulated result under normal incidence (approximated in the measurement as 10 degrees off the normal incidence). The absorption performance is significantly worsened under TM oblique incidence [25, 36] because of a variation in the tangential electrical component (insets of Fig. 3.10). At the lower spectrum end, the measured results seem to be better than simulation due to the limited size of the absorber sample. Only a small portion

Table 3.3. Comparison of the notable fabricated single-FSS absorbers. *Red blocks indicate lumped resistors whose thickness is not counted in the overall thickness, resulting in over-estimated figure of merit. • Polarization sensitive absorption due to planar anisotropy. DoF is the abbreviation of "degrees of freedom".

Reference	FSS Pattern	DoF	BWR ($f_L : f_H$)	$h(\lambda_L)$	Figure of Merit
[37]*		8	1 : 2.11	0.077	88.14%
[35]		6	1 : 2.86	0.111	64.22%
[12]		10	1 : 3.30	0.073	84.20%
[52]•		5	1 : 3.67	0.076	89.60%
[26]*		12	1 : 4.46	0.088	80.94%
Proposed		6	1 : 5.32	0.117	88.26%

of the operation bandwidth, namely less than 1 GHz at the higher spectrum end, is affected by diffraction at 30 degrees angle of incidence according to [1,51]:

$$f_g = c/[p(1 + \sin \theta_g)], \tag{3.4}$$

where θ_g is the angle of incidence, and f_g is the lowest frequency from which a grating lobe starts to occur.

A collection of notable experimentally validated single-FSS-layer wideband absorber designs, aiming at -10 dB reflectivity, are listed in Table 3.3. The featured designs are ranked in ascending order with regard to their relative bandwidths, and the realized total thicknesses h are normalized to the free-space wavelengths at the lowest operation frequencies. The figure of merit is a comprehensive criterion for performance evaluation, which abstracts the trade-off between BWR and h . It can be estimated by the ratio of Rozanov's optimal thickness d [31] to the achievable thickness h . The available

3.4 Conclusion

simulated reflection coefficients ρ have been used to determine the optimal thickness:

$$d = \frac{\int_0^\infty \ln(|\rho(\lambda)|) d\lambda}{2\pi^2 \mu_s}; \quad (3.5)$$
$$\text{Figure of Merit} = \frac{d}{h}.$$

where ρ is treated as a function of the free-space wavelength λ , and μ_s is the static permeability of the slab. Our absorber has the widest BWR of all featured works. Comparing with the polarization-insensitive designs (i.e., excluding [52]), it combines performance with simplicity, as evidenced by a high figure of merit and a low number of degrees of freedom (DoF).

3.4 Conclusion

The absorber design investigated in this chapter consists of a single resistive FSS layer and a dielectric superstrate. A square patch, as the most fundamental FSS pattern, is chosen to simplify the circuit analysis and synthesis procedure. By fully exploiting the potential of a series RLC, a very competitive performance has been achieved compared to existing more complicated designs in the literature. The most significant conclusion drawn from the considerations is that broader bandwidth and overall thinner structure can be achieved simultaneously by adopting a superstrate as the outermost matching cover. In addition, the fabrication tolerance and insensitivity to oblique incidence have been experimentally verified.

The unit cell geometry may be further adapted into other elementary shapes for improved absorption performance, or evolve into more sophisticated patterns to further approach theoretical limits. The materials adopted for the superstrate and substrate also can be varied to satisfy specific mechanical and thermal properties.

Fast Semi-Analytical Design Approach for Circuit-Analog Absorbers

EXTENDING from the qualitative techniques proposed in the previous chapter for optimizing absorbers with a single frequency-selective surface (FSS), a quantitative design approach is developed in this chapter to exhaustively exploit the potential of fundamental FSS patterns and the absorber topology as a whole. The proposed semi-analytical design method systematically integrates analytical, empirical, and numerical techniques for analyzing and synthesizing circuit analog (CA) absorbers. It dramatically reduces the number of full-wave simulations required for global optimization, so that the near optimal bandwidth-thickness can be quickly and reliably calculated for a given single-FSS-layer topology with the semi-analytical algorithm. To demonstrate the robustness of our semi-analytical approach, a square-patch and square-ring FSS absorbers at 10 dB level of absorption are revisited and optimized. The designs are constrained by available materials and standard tolerances for experimental validation. A manufactured prototype achieves a relative bandwidth of 144.15% and a normalized thickness of $0.0972\lambda_L$, which is superior to existing designs with more complicated FSS patterns in the literature.

4.1 Introduction

The past few decades have seen a great leap in the number of wireless communication devices, which have led to an increasingly complicated electromagnetic (EM) environment. Correspondingly, EM absorbers find wide applications in interference reduction and compatibility enhancement for integrated radio frequency (RF) components [53, 54]. Another application includes resolution improvement for satellite navigation systems by eliminating backscattering [35].

In practice, a microwave absorber can be primarily evaluated in terms of its absorption level, relative operation bandwidth, and thickness expressed in wavelength at the lowest operation frequency. Despite a high absorptivity and broad bandwidth, pyramidal absorbers are bulky and fragile, and thus their usage is limited in anechoic chambers. Composed of homogeneous resistive sheets, the Jaumann absorber offers reduced profile but modest performance [1, 8]. To further enhance the bandwidth-to-thickness ratio of planar absorbers, circuit-analog (CA) absorbers have been introduced with lossy periodic patterns to manipulate the input impedance through shunt equivalent circuit elements. Based on the Bode-Fano constraint of transmission line (TL) theory, the trade-offs in absorber performance were quantified by Rozanov via a theoretical minimal thickness for a specified reflection level and operation bandwidth [26, 31, 37, 44]. On that basis, the objective function for absorber optimization can be accordingly defined as how close the realized thickness is to this theoretical limit [22].

Most studies on CA absorbers have focused on exploration of various unit-cell patterns with multiple resonances [8–12, 24]. The main limitation of the approach stems from the fact that full-wave optimizations rapidly become computationally prohibitive with increasing degrees of freedom (DoF) in the geometry. To reduce the computation cost, frequency-selective surfaces (FSSs) are typically approximated by fundamental *RLC* circuits [55]. A particularly important aspect is the control of the resistive loss, which can be achieved by silk-printed resistive sheets [21, 35, 39, 48], or by using high-frequency chip resistors [26, 37, 38, 46, 47], noting that the manufacturing scalability of the latter approach may be limited. Nonetheless, it is generally challenging or even intractable for equivalent circuits to a-priori reproduce the impedance variation throughout a wide spectral range or to predict mutual coupling among geometric features with sufficient accuracy. As such, the absorbers designed in this way are often not approaching the theoretical limit. A number of analytical formulas describing the relationship between a specific FSS shape and its equivalent circuit configuration

have been adopted to facilitate absorber design [26–28]. However, their complexity hikes dramatically with each additional geometric feature (e.g., from square patch to square loop [56]) whilst their accuracy is not sufficient. The gap in-between circuit optimization and generic structure synthesis motivates the development of concise semi-analytical tools that benefit from the speed and comprehensiveness from analytical models, while achieving the accuracy close to full-wave simulations.

In this chapter, an efficient and effective optimization approach for CA absorbers is developed by systematically integrating analytical, empirical and numerical techniques. In view of the control variates method (i.e., varying one design variable whilst retaining the others), it is first observed that the unit-cell geometry, the lossless dielectric substrate/superstrate and the sheet resistance linearly and independently affect the equivalent circuit elements of a lossy FSS. Importantly, in lieu of an exhaustive full-wave parametric sweep, the proposed approach allows to reduce the millions of full-wave evaluations into three small groups of dozens or hundreds of generic seed simulations. Regression functions are then obtained by fitting circuit topologies with full-wave seed simulations as illustrated in Fig. 4.1. These functions can be recombined for semi-analytical synthesis which leads to accurate and fast computations with the aid of appropriate circuit models. This approach can be broadly considered as related to a Surrogate Model in space-mapping technique [57,58]. Global optimization methods such as the genetic algorithm (GA) can then be adopted to accelerate the search in the parameter space of the fundamental FSS geometries towards enhanced absorption performance. Adopting this technique, we can not only draw corollaries on choice of materials (i.e., dielectrics and resistive sheet), but also demonstrate that the FSS pattern of a CA absorber does not necessarily need to be complicated, where relatively simple shapes can achieve performance close to the theoretical limit exploiting the fact that they are tractable for optimization. To verify the effectiveness of the proposed methodology, a single-FSS-layer absorber adopting square rings as the unit-cell pattern is synthesized and experimentally characterized. Despite the structural simplicity, it achieves a relative bandwidth of 144.15% for a polarization-independent 10 dB absorption level. The design outperforms single-FSS-layer wideband absorbers demonstrated in the open literature.

4.2 Semi-Analytical Design Approach

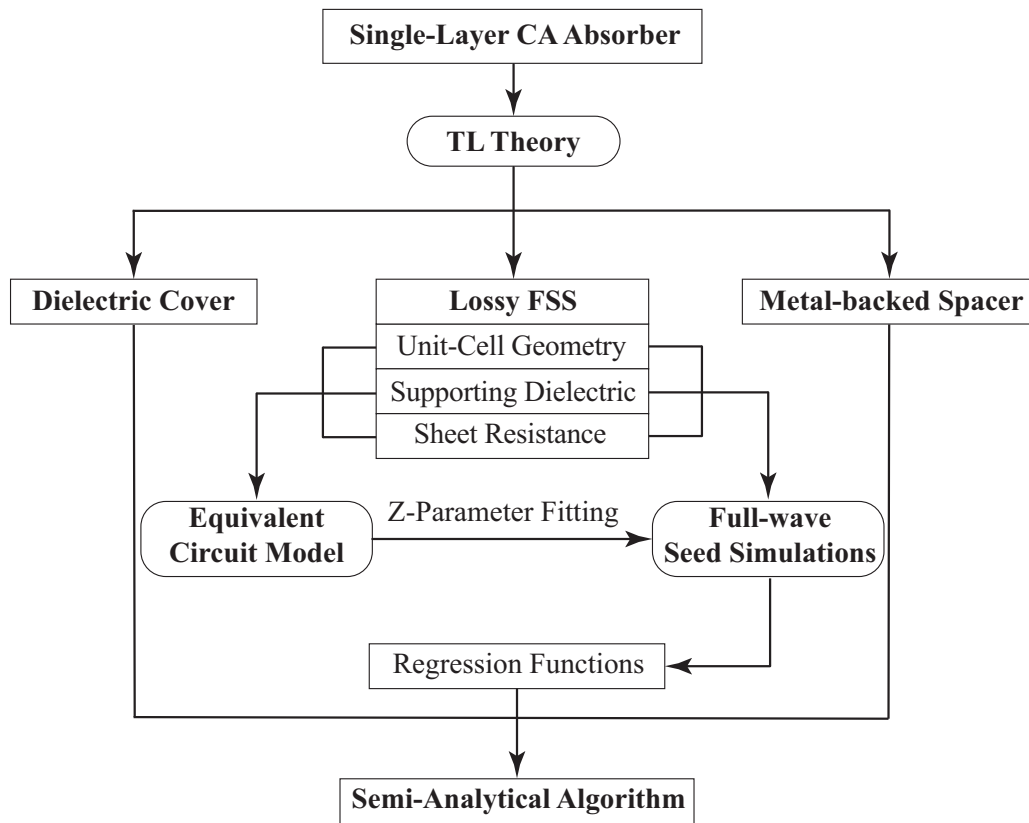


Figure 4.1. Overview of the semi-analytical design approach. The control variates method is applied to each essential element of a dielectric supported lossy FSS, for which regression functions can be obtained by fitting the Z-parameters. The overall absorber assembly is based on the transmission line (TL) theory.

4.2 Semi-Analytical Design Approach

A typical single-FSS-layer CA absorber includes a lossy periodic array of resonators and a metal-backed spacer. Its bandwidth-to-thickness ratio and insensitivity to angle of incidence can be simultaneously improved by adding a dielectric cover, which serves as an impedance transformer [22, 25]. Exhaustive search on such an absorber requires $m^{n_1+n_2+n_3}$ full-wave simulations in total, where m is the sample size for each design variable, and n_1, n_2, n_3 are the number of design variables for each part of the FSS, namely the unit-cell resonator geometry, the lossless dielectrics and the sheet resistance. Here for simplicity in demonstration, m has been assumed equal for each variable without restriction to generality. In the following subsections 4.2.1, 4.2.2 and 4.2.3, we will detail how the number of required simulations is determined and how to lower it to a much smaller set of $2m^{n_1-1} + m^{n_2-2}$ seed simulations by exploiting the properties of the FSS including linearity, independence and scalability. The Z-parameters of these

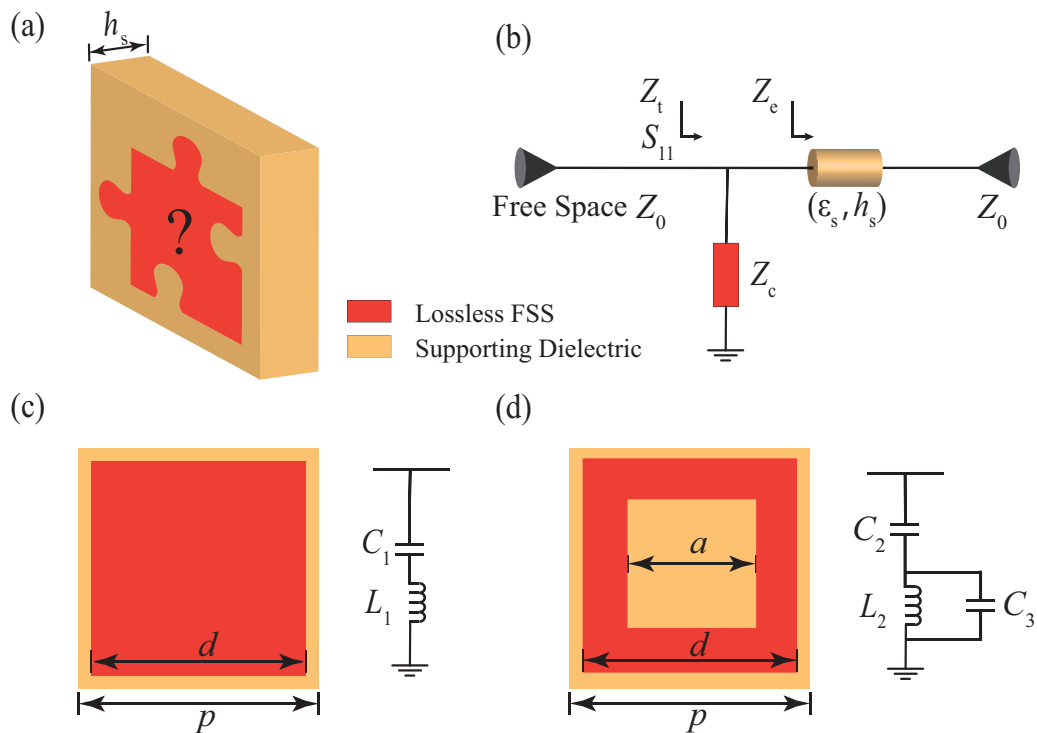


Figure 4.2. Dielectric-supported lossless single-layer FSS. (a) 3D view of a unit-cell geometry; (b) generic transmission line topology; equivalent circuit for (c) square patch and (d) square ring.

seed simulation results will be statistically fitted with their equivalent circuit models, where the *RLC* components can be reversely expressed as a function of geometric dimensions and material attributes of the FSS. This lays a foundation for the proposed semi-analytical method.

Based on a generic structure with no ground plane, the FSS pattern, the supporting dielectrics and the sheet resistance are independently investigated in subsections 4.2.1, 4.2.2 and 4.2.3 to obtain multi-regression models. They are then recombined with a metallic ground using the TL theory in subsection 4.2.4 for synthesizing single-FSS-layer absorbers. Square patch and square ring, as the most fundamental FSS shapes, are studied in parallel throughout the following subsections. All full-wave simulations are performed with Ansys HFSS™.

4.2.1 Equivalent Circuit Elements for Lossless FSS Patterns

Our investigation begins with a lossless FSS on a supporting substrate and its generic transmission-line topology, as shown in Fig. 4.2(a) and (b). A simple square patch is considered first because of its simplicity. From there, further geometric features such

as an inner aperture in the patch can be added to enhance the overall performance or to reduce the total thickness. Equivalent circuit models are presented in Fig. 4.2(c) and (d) next to their unit-cell patterns.

Square Patch Array

The impedance Z_c of a lossless square patch array, according to the lumped circuit model as illustrated in Fig. 4.2(c), can be calculated for a given angular frequency ω as [21]:

$$Z_c = j\omega L_1 + \frac{1}{j\omega C_1}. \quad (4.1)$$

By extracting its resonant frequency $\omega_0 = 1/\sqrt{L_1 C_1}$ from the full-wave simulated transmission coefficient S_{21} , Z_c can be expressed as a univariable function of L_1 at each frequency:

$$Z_c = j \frac{\omega^2 - \omega_0^2}{\omega^2} L_1. \quad (4.2)$$

To avoid diffraction effects that could mask the fundamental resonance at high frequencies, a supporting dielectric layer can be introduced to lower the resonance frequency of the simulated square patch array, as illustrated in Fig. 4.3(a). The resonance is then shifted to the left by approximately $\omega_0/\sqrt{\epsilon_s}$, where ϵ_s is the relative permittivity of the substrate. In this study, for referencing purpose but without restriction to generality, a 7-mm thick lossless substrate of relative permittivity $\epsilon_s = 4$ is chosen. This supporting dielectric is sufficient to avoid the masking effect of diffraction for all cases of interest.

On the basis of the TL theory [23], the impedance of the FSS can also be expressed in terms of the full-wave simulated reflection coefficient S_{11}

$$Z_c = \frac{Z_0 Z_e (1 + S_{11})}{Z_e (1 - S_{11}) - Z_0 (1 + S_{11})}, \quad (4.3)$$

where Z_0 is the intrinsic impedance of free space, and Z_e is the impedance of the substrate together with the free space behind, as indicated in Fig. 4.2(b). By minimizing the root-mean-square deviation between the circuit-analyzed impedance in (4.2) and the full-wave simulated impedance in (4.3) across the spectrum, the values of the reactive components L_1 and C_1 for this particular patch configuration can be obtained. This will only be necessary for a few seed simulations as will be explained later in this section.

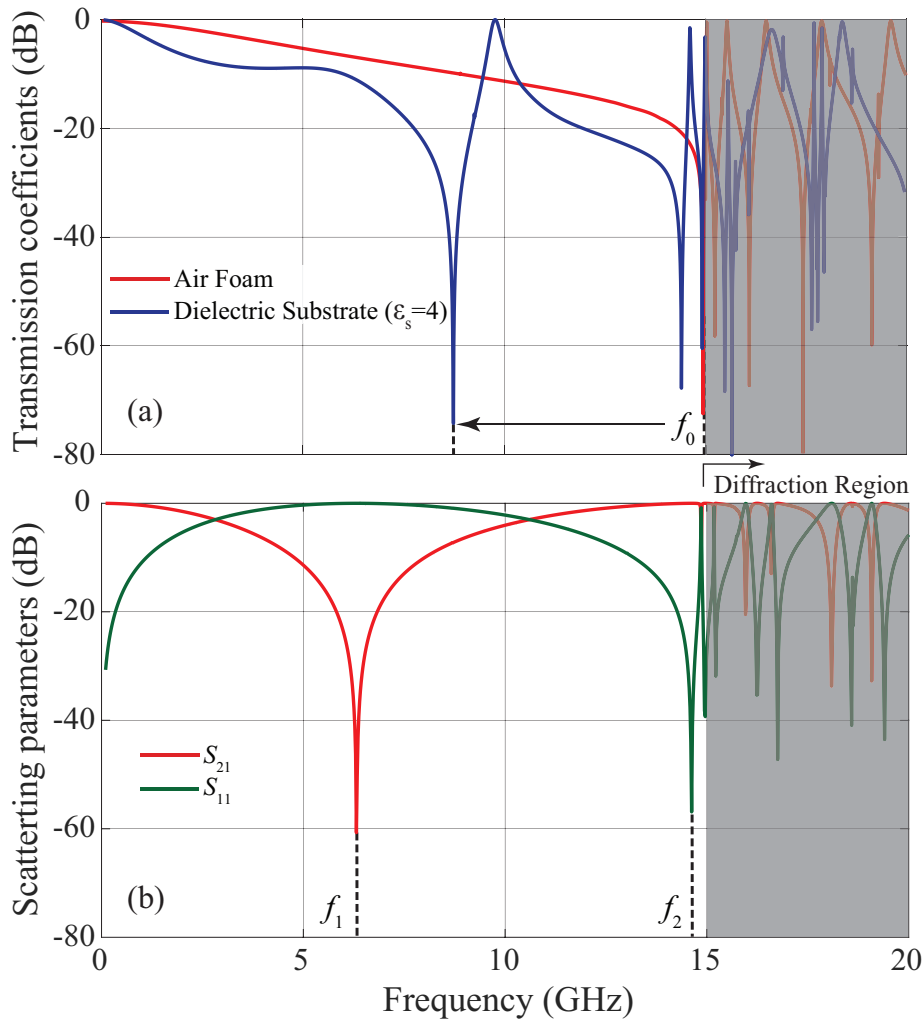


Figure 4.3. Full-wave simulated S -parameters for fundamental unit-cell patterns. (a) transmission coefficients for lossless square patch FSS ($p = 20$ mm, $d = 18$ mm); and (b) transmission and reflection coefficients for air foam supported lossless square ring FSS ($p = 20$ mm, $d = 18$ mm, $a = 12$ mm). $f_n = \omega_n/2\pi$ ($n = 0, 1, 2$). According to Equation (3.4), the onset frequency from which a grating lobe starts to occur equals c/p under normal impinging waves.

Square Ring Array

The equivalent circuit model for a lossless square-ring FSS is illustrated in Fig. 4.2(d). Its impedance can be calculated as:

$$Z_c = \frac{1 - \omega^2 L_2 (C_2 + C_3)}{j\omega C_2 (1 - \omega^2 L_2 C_3)}. \quad (4.4)$$

The zero and pole are at critical angular frequencies $\omega_1 = \sqrt{1/[L_2 (C_2 + C_3)]}$ and $\omega_2 = \sqrt{1/(L_2 C_3)}$ which can be extracted from the minima of the full-wave simulated scattering coefficients S_{21} and S_{11} respectively. Then, by substituting $C_3 = 1/(\omega_2^2 L_2)$ and

4.2 Semi-Analytical Design Approach

$C_2 = 1/(\omega_1^2 L_2) - 1/(\omega_2^2 L_2)$ in (4.4), Z_c can be represented as a frequency-dependent function of L_2

$$Z_c = \frac{1 - \frac{\omega^2}{\omega_1^2}}{j\omega \left(\frac{1}{\omega_1^2} - \frac{1}{\omega_2^2} \right) \left(1 - \frac{\omega^2}{\omega_2^2} \right)} L_2. \quad (4.5)$$

The resonant trough at ω_1 , as indicated in Fig. 4.3(b), is located far away from the diffraction region, and as such a supporting dielectric is not essential in this case. As a simplified version of (4.2) where $Z_e = Z_0$, the corresponding impedance determined from the simulated reflection coefficient is

$$Z_c = -\frac{Z_0(1 + S_{11})}{2S_{11}}. \quad (4.6)$$

Similarly, the values of the reactive components L_2 , C_2 and C_3 will be obtained by fitting Z_c in (4.5) to (4.6) across the spectrum.

A square patch can be considered as the special case of a square ring with no aperture. If the inner aperture length a is not sufficiently large, the pole at ω_2 may fall in the diffraction region due to small L_2 and C_3 . In this case, the initial value of ω_2 has to be assumed at the diffraction onset and then adjusted adaptively to probe the best Z-parameter fit. Further evolved FSS patterns with more design variables can be analyzed by investigating the zeros and poles of their Z-parameters with appropriate equivalent circuit models.

Tabulated Seed Simulations

A limited number of seed simulations are conducted for investigating the contribution of each essential part of a dielectric-supported lossy FSS to the *RLC* configurations of their equivalent circuit model. The obtained values of circuit components for feasible combinations of design variables are tabulated and then fitted by semi-analytical functions using least-square method with a reasonably large coefficient of determination ($R^2 \geq 0.9$). In conjunction with the TL topology and FSS properties, these regression functions can be recombined for synthesizing and optimizing a single-FSS-layer absorber.

A square patch array contains two DoFs, namely the patch length d and the periodicity p of a unit-cell. Accordingly, the required lookup tables for its equivalent inductance and capacitance should be two-dimensional. Nonetheless, based on the fact that rescaling the FSS with a factor ζ will proportionally relocate the transmission and reflection coefficients by $1/\zeta$ in frequency, the seed simulations can be simplified to a

one-dimensional set using $\alpha = d/p$ as parameter, which empirically needs to be larger or equal to 0.7 to obtain a practically sufficiently large capacitance C_{1B} in-between adjacent patches. With arbitrarily chosen (scalable) reference periodicity $p = 20$ mm, L_{1B} and C_{1B} can be statistically fitted in Matlab™ toolbox as univariable functions of α based on a very limited number of seed simulations:

$$\begin{aligned} L_{1B} &= 9.4(1 - \alpha)^{1.48} + 0.2 \text{ nH}; \\ C_{1B} &= 147.8(1 - \alpha)^{-0.67} - 104.5 \text{ fF}. \end{aligned} \quad (4.7)$$

A square-ring FSS has one more independent variable $\beta = a/p$ that describes the inner aperture size. It is observed that this parameter empirically needs to be larger or equal to 0.45 to ensure a distinguishable resonant performance from a square patch. The lookup tables for equivalent reactive components therefore become two-dimensional and depict biharmonic surfaces as a function of (α, β)

$$\begin{aligned} L_{2B} &= e^{-4.06\alpha + 4.27\beta + 1.89} - 0.29 \text{ nH}; \\ C_{2B} &= e^{31.67\alpha - 24.24} + 111\beta + 75.76 \text{ fF}; \\ C_{3B} &= e^{5.67\alpha - 4.49\beta + 1.65} - 3.26 \text{ fF}. \end{aligned} \quad (4.8)$$

Assuming the sample size is $m = 15$ for each design variable, and the number of independent design variables for the unit-cell geometry is $n_1 - 1 = 1$ for square patch or $n_1 - 1 = 2$ for square ring, then their reactive components can be interpolated via regression function sets (4.7) or (4.8) with $m^1 = 15$ or $m^2 = 225$ seed simulations respectively.

4.2.2 Impact of Dielectric Substrate on Reactive Components

So far the modeling has assumed a fixed permittivity and thickness for the supporting dielectric layer. The substrate and a dielectric cover (if present) do not only contribute to the EM wave propagation as transmission lines, but also impact on the equivalent reactance of the FSS. Indeed, lateral coupling between unit-cells and current distribution on conductive patterns are both affected by the supporting dielectric. Therefore, the equivalent inductance and capacitance change accordingly. Within a practical range of FSS dimensions, we found that the same dielectric slab contributes to the reactive components with the same set of scaling factors. The impact of permittivity and thickness can then be investigated with a arbitrarily selected reference FSS.

4.2 Semi-Analytical Design Approach

Our previous work [22] indicated that an air spacer as the substrate would maximize the bandwidth-to-thickness ratio of a CA absorber with a dielectric superstrate. Therefore, the relative permittivity of the substrate can be set to $\epsilon_r = 1$ and the number of DoFs for the FSS can be further reduced by 2 (i.e., the permittivity and thickness of the substrate). On that basis, the number of additional seed simulations required to characterize the effect of substrate and superstrate on the FSS is only m^2 , where m is the sample size for each design variable, and $n_2 - 2 = 2$ is the number of independent design variables for the lossless dielectrics, including permittivities and thicknesses for both superstrate and substrate. Specifically, if the sample size is $m = 15$ for each design variable, only 225 seed simulations are needed for any FSS array.

Square Patch Array

For the reference lossless square-patch FSS, as shown in Fig. 4.4, its equivalent inductance and capacitance are positively correlated to the permittivity ϵ_s and thickness h_s of a dielectric superstrate. We obtained empirical formulas for L_1 and C_1 of the patch in the presence of a superstrate in conjunction with (4.7) as:

$$\begin{aligned} L_1 &= L_{1B} \Theta_{L_1}(\epsilon_s, h_s); \\ C_1 &= C_{1B} \Theta_{C_1}(\epsilon_s, h_s), \end{aligned} \quad (4.9)$$

with the normalized scaling factors Θ_{L_1} and Θ_{C_1} of this dielectric represented as regression functions of ϵ_s and h_s

$$\begin{aligned} \Theta_{L_1}(\epsilon_s, h_s) &= \frac{\sqrt{\epsilon_s}}{2.5} \left[\tan^{-1} \left(\frac{h_s}{6.3} \right) + \frac{e^{1-0.29\epsilon_s}}{2} \right]; \\ \Theta_{C_1}(\epsilon_s, h_s) &= \frac{(1 - 0.79\epsilon_s) e^{-h_s/2} + 2\epsilon_s^{0.77}}{5.5}, \end{aligned} \quad (4.10)$$

where the permittivity ϵ_s is no more than 10 taking into account the impedance matching purpose of the dielectric superstrate, and the thickness h_s is no more than 20 mm within the considered operating frequency range.

Square Ring Array

The impact of the dielectric layer on reactive components of a square-ring FSS are dominated by ϵ_s provided that h_s is larger than $0.05\lambda_1$ [1] (e.g., $h_s > 0.75$ mm given $\lambda_1 = c/(f_1\sqrt{\epsilon_s})$, $f_1 = 10$ GHz and $\epsilon_s = 4$), as the evanescent wave decays dramatically with the distance from the array surface. Through a similar approach as for the

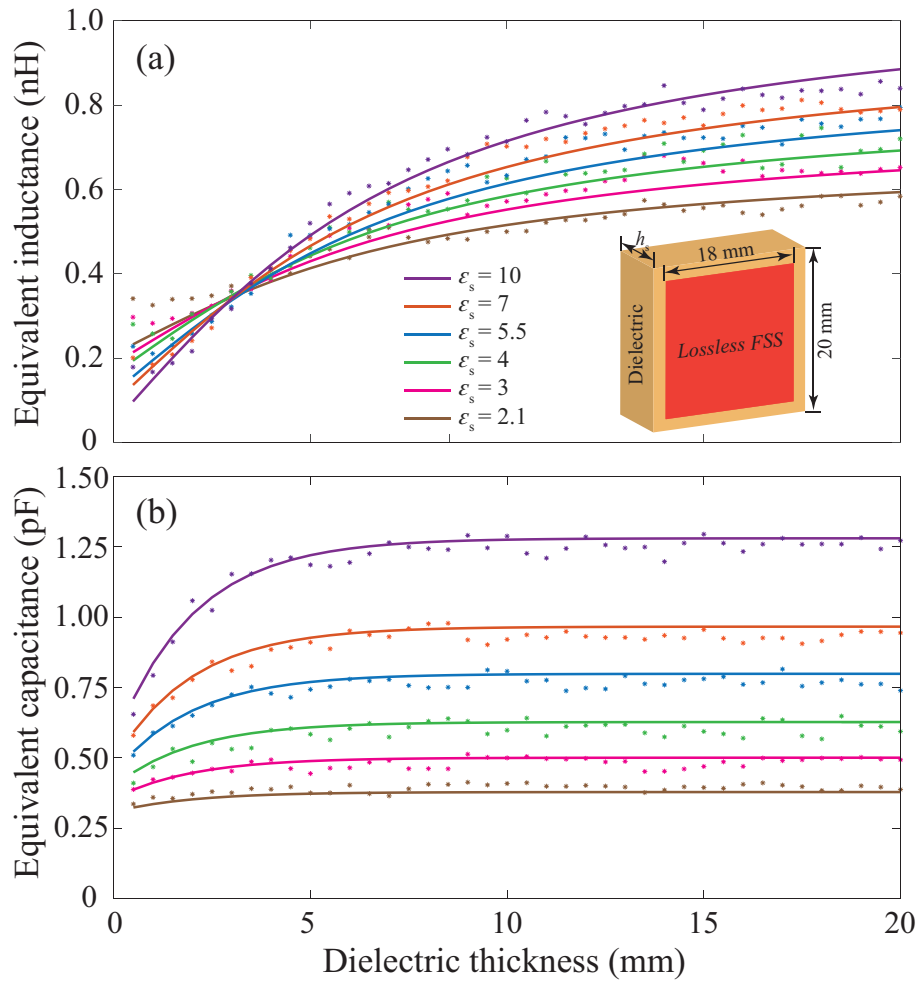


Figure 4.4. Impact of dielectric substrate on equivalent reactive components for a reference square patch FSS. The periodicity $p = 20$ mm and the patch length $d = 18$ mm. (a) Inductance and (b) capacitance are a function of dielectric thickness and permittivity. Circuit modeling is an ideal analyzer with macro physical insight, and thus insignificant systematic fluctuations can be observed in the analyzed results. The scatter plots are fitted with regression lines defined by function sets (4.10).

square-patch FSS, the normalized scaling factors of a supporting dielectric for L_2 , C_2 , and C_3 can be approximated in terms of ϵ_s only, provided the condition $h_s > 0.05\lambda_1$ is satisfied:

$$\begin{aligned}\Phi_{L_2}(\epsilon_s) &= 1; \\ \Phi_{C_2}(\epsilon_s) &= \Phi_{C_3}(\epsilon_s) = \frac{1 + \epsilon_s}{2}.\end{aligned}\quad (4.11)$$

The scaling factor for inductance is approximately 1 because the strips of a typical square ring (i.e., $\beta \geq 0.45$) introduce significantly larger current densities than the square patch. Compared to the relatively small impact from the dielectric slab, the

equivalent inductance is dominated by the geometric features of the conductors. In contrast to the side-to-side electric flux of a patch array, the equivalent capacitances of a typical square ring can be differently explained by an edge-to-edge model. With a single-side dielectric support, the equivalent capacitances are proportional to the averaged relative permittivities of the free space and the supporting material. Thus, the critical frequencies will be lowered by ratio of $1/\sqrt{(1+\epsilon_s)/2}$ which equals the square-root of the scaling factor for capacitance. In analogy to (4.9), the complete set of empirical formulas for L_2 , C_2 and C_3 can be acquired through pair-wise products of expressions in (4.8) and (4.11)

$$\begin{aligned} L_2 &= L_{2B}\Phi_{L_2}; \\ C_2 &= C_{2B}\Phi_{C_2}; \\ C_3 &= C_{3B}\Phi_{C_3}. \end{aligned} \tag{4.12}$$

4.2.3 Impact of the Sheet Resistance

The equivalent circuit models for resistive square-patch and square-ring FSSs, as shown in Fig. 4.5, are expansions of Fig. 4.2(c) and (d) which depicted corresponding lossless FSS patterns. Since the equivalent reactive components are dominantly determined by the FSS geometry [21,22], the results from subsection 4.2.1 can be directly used to limit the number of seed simulations. In the circuit model, the placement of lumped resistors depends on the geometrical shape of the FSS, whilst their values are in proportion to the surface resistance of the conductive area in a unit cell [21].

The number of design variables for the sheet resistance itself is $n_3 = 1$, namely a value in Ω/\square . In conjunction with scalability and linearity, the numbers of seed simulations for resistive square-patch or square-ring FSS is only $m^{n_1-1+n_3-1} = m^{n_1-1}$. Specifically, if the sample size is $m = 15$ for each design variable, then their resistive components can be interpolated with $m^1 = 15$ or $m^2 = 225$ seed simulations for the square-patch or square-ring FSS respectively.

Square Patch Array

The equivalent shunt circuit for the square-patch FSS, according to Fig. 4.5(a), is an *RLC* in series:

$$Z_c = j\omega L_1 + \frac{1}{j\omega C_1} + R_1. \tag{4.13}$$

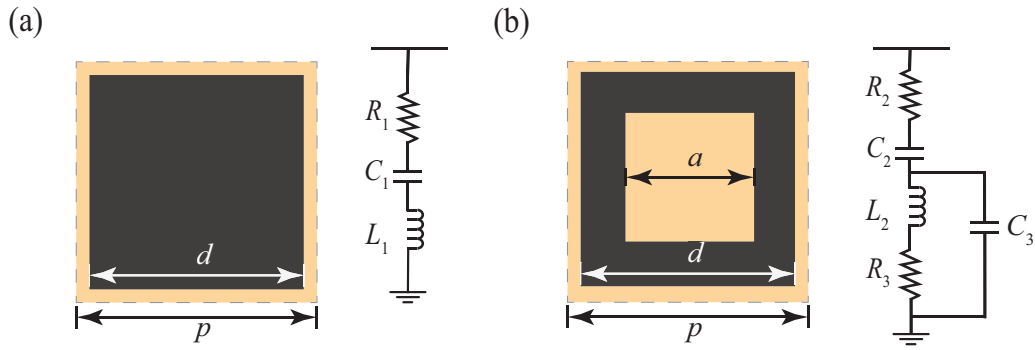


Figure 4.5. Equivalent circuit models for unit-cell FSS adopting a patterned resistive layer. (a) square patch and (b) square ring. The distribution of lumped resistors depends on the unit-cell geometry.

Then, the relationship between α and R_1 can be determined by fitting (4.13) to (4.3) with only 15 seed simulations. The estimated equivalent lumped resistance for a square-patch FSS can be expressed in reverse proportion of the square patch size to the unit cell area:

$$R_1 = (1 + \zeta)R_s \left(\frac{1}{\alpha}\right)^2, \quad (4.14)$$

where R_s is the surface resistance in Ω/\square , and $\zeta = 5\%$ acts as an empirical correction factor because of the fringing effect. Incidentally, this model is in agreement with the existing empirical formula [21,22].

Square Ring Array

The impedance of the resistive square-ring FSS can be calculated in accordance with Fig. 4.5(b)

$$Z_c = \frac{j\omega L_2 + R_3}{1 - \omega^2 L C_3 + j\omega R_2 C_3} + \frac{1}{j\omega C_2} + R_2. \quad (4.15)$$

The relationship between the equivalent lumped resistors (i.e., R_2 and R_3) and the FSS dimensional parameters can be obtained by fitting Z_c in (4.15) to (4.6) with only 225 seed simulations. Because R_2 and R_3 are proportional to the surface resistance R_s , the number of DoF can be reduced by adopting an arbitrary reference resistive sheet of $R_0 = 100 \Omega/\square$ to facilitate the calculation:

$$\begin{aligned} R_2 &= \left(e^{-20.82\alpha^2 + 24.12\alpha + 8.50\beta - 5.31} + 148.1 \right) \frac{R_s}{R_0}; \\ R_3 &= \left(e^{-5.78\alpha + 5.48\beta + 6.57} - 13.8\alpha^4 \right) \frac{R_s}{R_0}. \end{aligned} \quad (4.16)$$

The above expressions are however found to remain valid for surface resistance R_s up to $1000 \Omega/\square$ in practice.

4.2 Semi-Analytical Design Approach

Table 4.1. Dimensions and material attributes for schematics in Fig. 4.6.

Schematic	α	β	h_s (mm)	ϵ_s	R_s (Ω/\square)
I.A	0.9	Nil	10	3	150
I.B	0.75	Nil	3	7	300
I.C	0.95	Nil	7	10	75
II.A	0.9	0.6	6	5.5	200
II.B	0.95	0.8	5	10	75
II.C	0.8	0.5	10	2.1	100

The periodicity p is fixed to 20 mm, and the thickness of the air spacer h_0 remains equal to 10 mm.

Table 4.2. Equivalent circuit components (two decimals) for lossy FSSs in Fig. 4.6.

Schematic	L_1 (nH)	C_1 (fF)	C_2 (fF)	R_1 (Ω)	R_2 (Ω)
I.A	0.56	471.04	Nil	194.44	Nil
I.B	0.87	413.08	Nil	576.81	Nil
I.C	0.36	2023.93	Nil	581.72	Nil
Schematic	L_2 (nH)	C_2 (fF)	C_3 (fF)	R_2 (Ω)	R_3 (Ω)
II.A	1.90	766.50	175.65	482.22	191.25
II.B	3.88	2956.22	148.94	298.45	144.75
II.C	1.91	213.57	73.99	271.19	143.90

4.2.4 Absorber Assembly and Algorithm Validation

Based on the acquired semi-analytical function sets described in subsections 4.2.1, 4.2.2 and 4.2.3, a direct mapping between the physical dimensions of a single-FSS-layer absorber and its equivalent circuit can be established with very quick calculation for analysis and synthesis. To validate the proposed approach and demonstrate its reliability, four single-FSS-layer absorber topologies are examined by comparing the performance determined from the full-wave simulation to those obtained from the semi-empirical circuit analysis. Within the feasible ranges of FSS dimensions, arbitrarily selected structural parameters and material attributes are listed in Table 4.1, whilst the estimated equivalent circuit elements are tabulated in Table 4.2.

The reflection coefficient for a single-FSS-layer absorber can be calculated in two different cases:

- With dielectric substrate:

$$S_{11} = \frac{Z_c // Z_e - Z_0}{Z_c // Z_e + Z_0}, \quad (4.17)$$

where $Z_e = jZ_s \tan(2\pi f \sqrt{\epsilon_s \epsilon_0 \mu_0} h_s)$, and $//$ indicates parallel circuit topology for simplicity.

- With air spacer and dielectric superstrate:

$$S_{11} = \frac{Z_s(Z_t - Z_0) + j \tan(2\pi f \sqrt{\epsilon_0 \mu_0} h_0)(Z_s^2 - Z_0 Z_t)}{Z_s(Z_t + Z_0) + j \tan(2\pi f \sqrt{\epsilon_0 \mu_0} h_0)(Z_s^2 + Z_0 Z_t)}, \quad (4.18)$$

where $Z_s = \sqrt{\frac{\mu_0}{\epsilon_0 \epsilon_s}}$, and $Z_t = Z_c // jZ_0 \tan(2\pi f \sqrt{\epsilon_0 \mu_0} h_0)$.

As illustrated in Fig. 4.6, the reflection coefficients calculated using the semi-analytical method closely resemble the HFSSTM simulated results throughout the frequency range. It is emphasized that the absorber designs listed are randomly selected to verify the accuracy of the proposed algorithm, and as such they are unlikely to be optimal in the bandwidth-to-thickness ratio.

4.3 Global Optimization and Evaluation Criterion

In contrast to a full parametric sweep that would demand $m^{n_1+n_2+n_3}$ full-wave simulations, the proposed design approach merely requires $2m^{n_1-1} + m^{n_2-2}$ reusable seed simulations for thorough search with acceptable reliability. Taking a typical sample size $m = 15$ for example, the number of full-wave simulations dramatically reduces from 1.71×10^8 to 255 for a square patch absorber optimization, and correspondingly from 2.56×10^9 to 675 for a square ring configuration. Once the once-off seed simulations are completed, the optimization can be carried out using the semi-analytical computations in MATLABTM, which are approximately 10^5 order of magnitude faster than full-wave simulations in HFSSTM. Of course, those computation times can be further reduced using evolutionary optimization algorithms, such as GA. By virtue of this proposed fast calculation algorithm, global optimization becomes feasible to determine the near-optimal absorber designs that yield a minimal thickness for a specified relative

4.3 Global Optimization and Evaluation Criterion

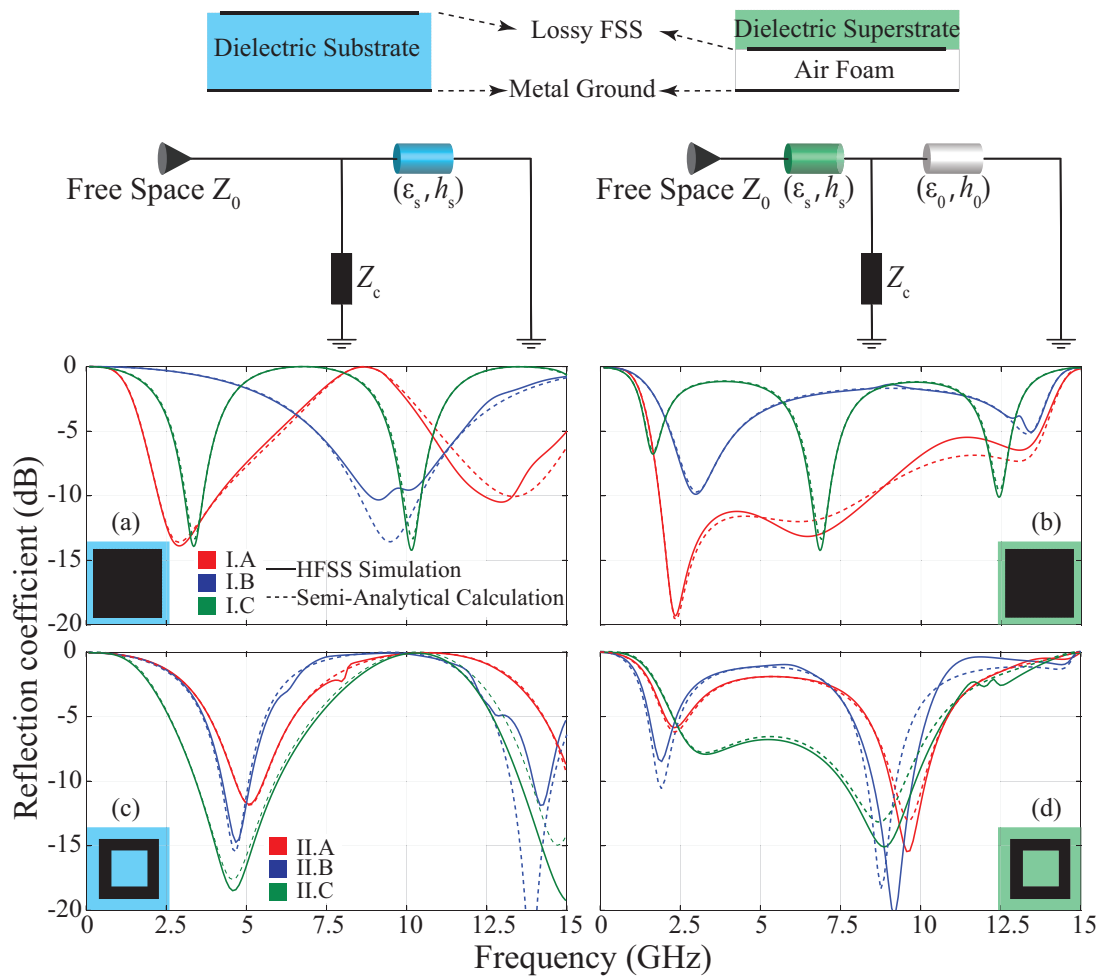


Figure 4.6. Reflection coefficients for random designs in four different absorber topologies.

Categorization is based on the position of dielectric slab and the FSS geometry. These are not optimized absorber designs, but only for validation of the semi-analytical calculation. Absorption performances for 3 random designs for each topology as indicated in Table 4.1 and Table 4.2 are obtained from full-wave simulations and circuit calculations respectively. The dielectric substrate is colored in blue whilst dielectric superstrate is colored in green. The substrate and superstrate have identical properties.

bandwidth at a given absorption level (e.g., 10 dB) in relation to the topologies shown in Fig. 4.6. In the present case, the GA is chosen as optimization technique [50], although other choices of global optimization algorithm could be considered. Figure. 4.7 shows the minimal thickness curves obtained from optimizing these absorber topologies for specified relative bandwidth at a reflection level of -10 dB. Each scatter point distributed along the curve represents a CA absorber synthesized by the optimization algorithm that aims for the smallest thickness at a specified bandwidth. The performance for all these designs are further verified using the full-wave simulator. The

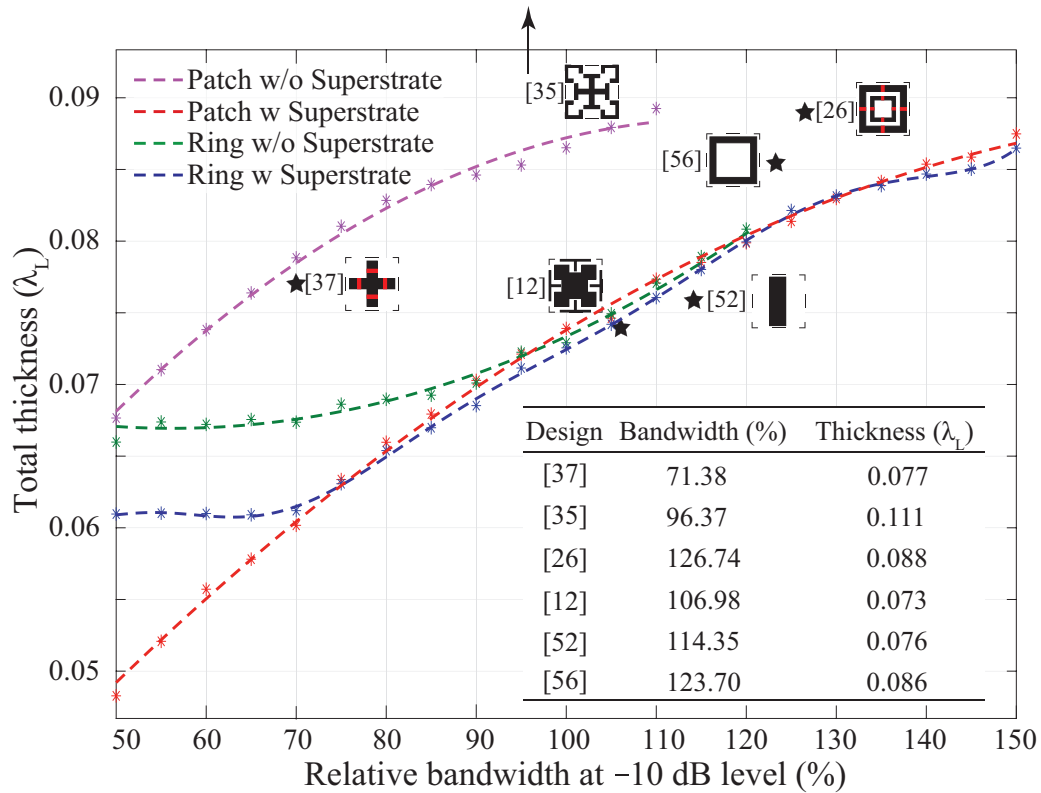


Figure 4.7. Optimized bandwidth-thickness curves for different topologies as illustrated in Fig. 4.6. The discrete solutions are verified with full-wave simulation and then fitted with polynomial trend lines for visual aid. Simulation results for notable experimentally validated single-FSS-layer absorbers in the literature are indicated as stars or arrow (if located out of the range). The red dots with regard to [26, 37] indicate HF resistors whose physical thickness is not counted.

maximum absorption bandwidth for a square patch CA absorber is found to be around 110% (magenta curve). This can be increased to 120% by evolving into a square ring CA absorber (green curve), noting that a significantly smaller thickness can be achieved. Alternatively, further improvement can be attained by adopting an impedance transformer [22], with a possible bandwidth up to 150% (red curve). It is unnecessary to add an inner aperture to a square patch CA absorber with a superstrate (red curve vs. blue curve), because such a geometric feature does not appear to effectively contribute to further the absorption performance. Despite the simplicity in geometry, the maximal absorption bandwidth achievable for all topologies with an impedance transformer is around 150%, which is among the widest bandwidth found for single-FSS-layer absorbers reported in the literature.

A collection of simulated bandwidth-thickness coordinates for notable state-of-the-art single-FSS-layer absorbers [12, 26, 35, 37, 52, 56] are also included in Fig. 4.7. Design [56]

4.4 Experimental Validation

adopts square loop but its FSS is placed above both the air spacer and the dielectric layer. If a design is located lower than an optimized curve, then it outperforms the corresponding topology. Among the state-of-the-art designs, only [52] is lower than all the margins, but that design is polarization-dependent. We can deduce that a remarkable absorption performance can be achieved by fully exploiting the potential of fundamental shapes of FSS-based CA absorbers without necessarily resorting to sophisticated geometrical shapes that may be intractable for semi-analytical calculations.

4.4 Experimental Validation

4.4.1 Wideband Single-FSS-Layer Absorber Design

In order to further demonstrate the effectiveness of our design approach, a wideband single-layer absorber adopting a square ring lossy FSS and a dielectric superstrate is proposed, fabricated and experimentally characterized. Importantly, a practical design has to take into account the restricted availability of material characteristics and manufacturing tolerances. Therefore, a 2 dB margin for the absorption spectrum is reserved against tolerances in material attributes and structural dimensions. With a goal function aiming for the minimal total thickness at the maximal bandwidth, the optimization starts with a predetermined periodicity p of 20 mm to facilitate the numerical synthesis. Given an available dielectric substrate (i.e., 3 mm Rogers RT6002; $\epsilon_s = 3.0$, $\tan\delta = 0.0012$), the whole structure then needs to be rescaled accordingly. The resistive layer acquired from the commercial supplier Polychem[®] is silk-printed with conductive polymer ink on a 100 μm PET film to introduce sheet resistance. Its nominal surface resistance R_s is 75 Ω/\square , which is independently confirmed with our contact-less measurement equipment using the EddyCus[®] TF Lab 2020.

For the initial design, the equivalent circuit parameters are $C_2 = 860.57$ fF, $C_3 = 260.74$ fF, $L_2 = 0.78$ nH, $R_2 = 137.70$ Ω and $R_3 = 22.95$ Ω , whilst its synthesized physical dimensions are $d = 19.05$ mm, $a = 9.52$ mm, $h_s = 5.81$ mm and $h_0 = 12.19$ mm. The reflection coefficients obtained from the full-wave simulator HFSS[™] and from the semi-analytical algorithm implemented using MATLAB[™] match well throughout the absorption spectrum, as shown in Fig. 4.8. On this basis, the final manufacturable absorber design is obtained by rescaling the structure with a factor $\zeta_0 = 0.525$. Despite limited accessibility to materials, the simplicity in topology, and small total thickness of 9.5 mm, the fabricated prototype exhibits a measured operation bandwidth ranging

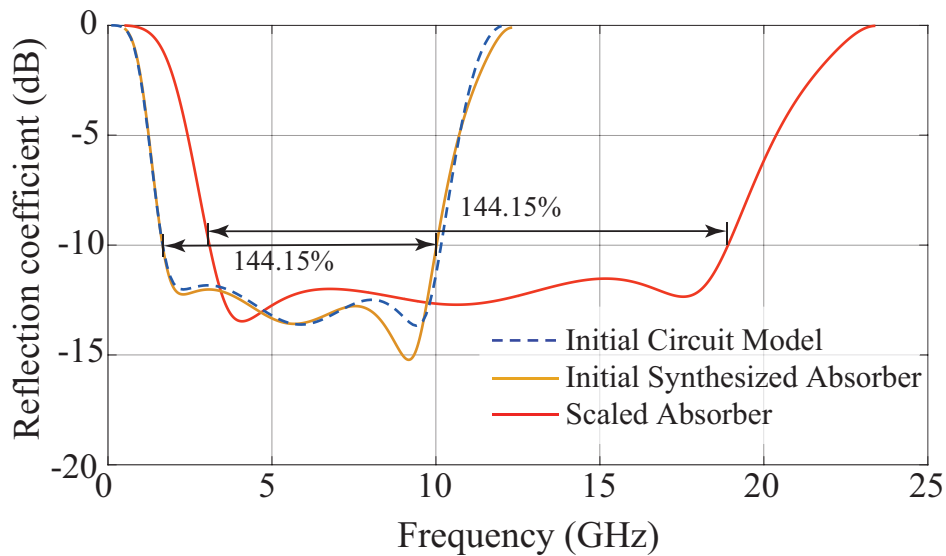


Figure 4.8. Absorption performance for designs during steps of the synthesizing process. It includes the initial circuit model, the initial synthesized spatial absorber, and the rescaled absorber. The scaling factor depends on the desired start frequency. The relative bandwidth remains unchanged as per discussion in subsection 4.2.1.

from 3.07 to 18.95 GHz, which is equivalent to a relative bandwidth of 144.15% and a normalized thickness of $0.0972\lambda_L$. For the same simulated reflection coefficients and FSS pattern, the proposed algorithm applied with an assumption of no material restrictions would yield a minimal total thickness of 9.37 mm. The Rozanov's thickness limit for this case would be 8.38 mm. This theoretical limit does not set any limitations on the complexity of the unit-cell geometry. Compared to our previous work [22] with 1 dB margin reserved against fabrication tolerance, the proposed design with 2 dB margin more completely exhausts the potential of the available materials and of the chosen topology as illustrated in Fig. 4.9.

4.4.2 Fabrication and Measurement

The exploded layers of the fabricated single-FSS-layer absorber before assembly are illustrated in Fig. 4.10. The resistive sheet is patterned with a LPKF[®] laser-milling machine. As shown in the inset of Fig. 4.11(a), a pair of ridged horn antennas are symmetrically mounted on a wooden arch to measure the reflectivity for TE or TM modes at the incidence angle ranging from 10 degrees to 50 degrees. Ideally, it is suggested that the absorber sample should be placed in the far-field of its operation range for measurement [40, 41]. The far-field distance equals $2D^2/\lambda = 11.15$ m, where D is the

4.4 Experimental Validation

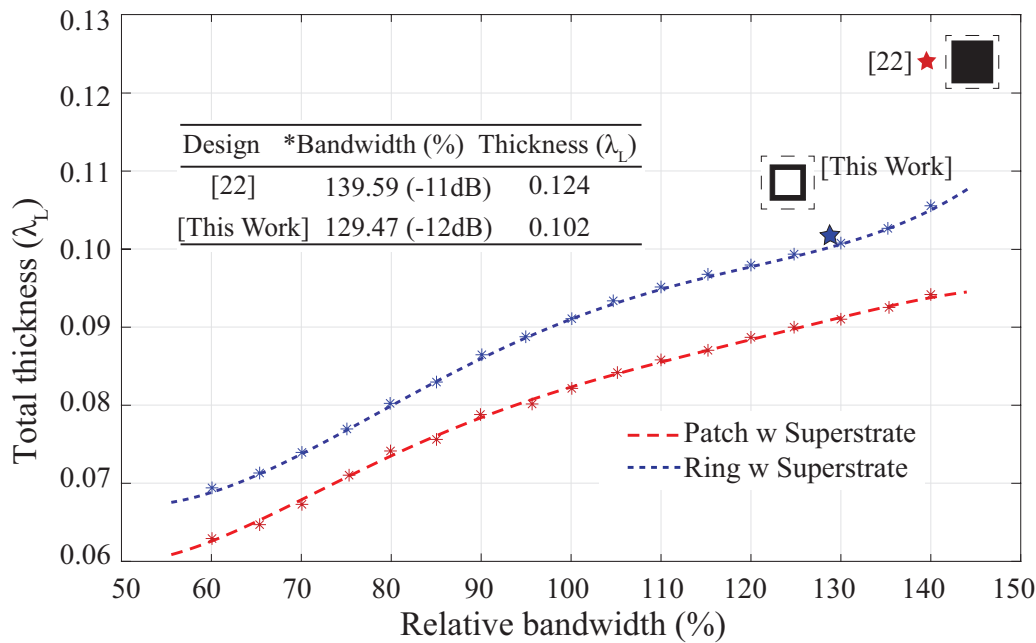


Figure 4.9. Optimized bandwidth-thickness curves for single-FSS-layer absorbers with performance margin included for fabrication tolerances. The benchmark for the relative bandwidth and normalized thickness are recalculated at 11 dB and 12 dB absorption level for our previous work and the proposed design respectively.

longer dimension of the A4 sized absorber and λ is the wavelength for the highest operation frequency 18.95 GHz. However, the radius of the wooden arch cannot be made beyond the height of our anechoic chamber. Nevertheless, results are expected to have only a small deviation, as the reflected energy (i.e., bi-static transmission coefficient) is normalized to a reference metal plate of the same size, rather than given as an absolute value.

As shown in Fig. 4.11, the measured 10 dB absorption under 10 degrees oblique incidence spans 3.15 to 19.2 GHz, which is a good approximation to the simulated result under normal incidence. At larger impinging angles, a deterioration in reflectivity can be observed under both TE and TM modes (Fig. 4.12). Specifically, the level of absorption decreases uniformly across the operation spectrum for the TE mode, whilst the absorption bandwidth reduces significantly on its lower frequency bound for the TM mode. This effect is typical for FSS-based structures. According to our previous work [22], the dielectric cover not only protects the FSS from detrimental environments and contributes to the impedance matching as an effective transformer, but also

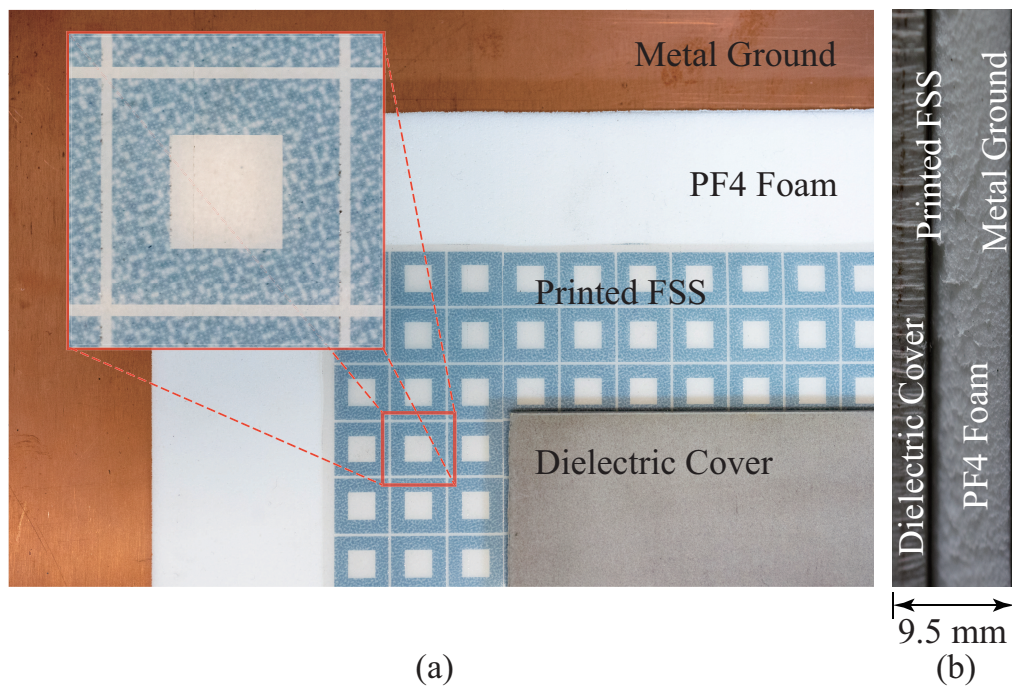


Figure 4.10. Fabricated single-FSS-layer absorber. (a) The exploded view reveals a copper ground, a PF4 ($\epsilon_r = 1.06$, $\tan\delta = 0.0001$) foam as substrate, square ring FSS ($R_s = 75 \Omega/\square$) printed on a thin PET film, and a Rogers RT6002 ($\epsilon_s = 3.0$, $\tan\delta = 0.0012$) as superstrate; (b) Side view.

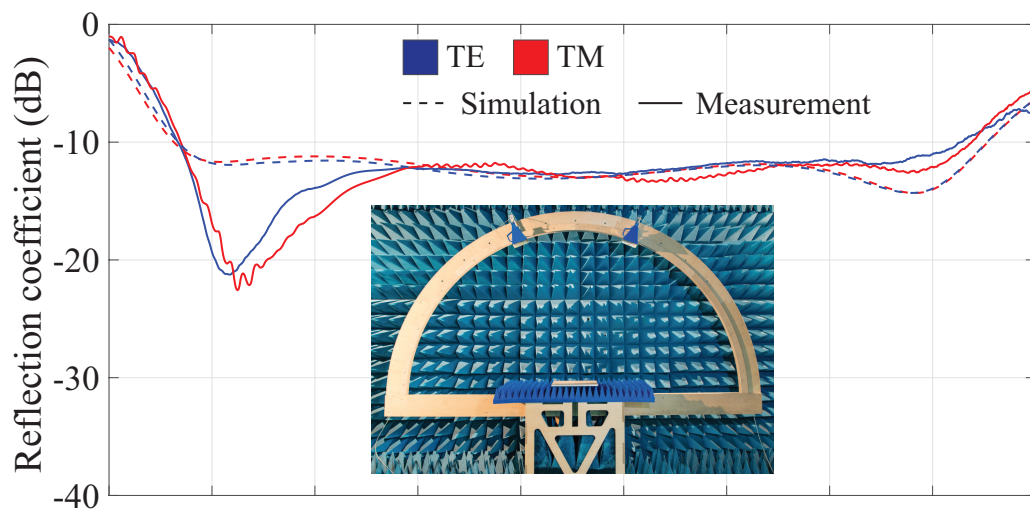


Figure 4.11. Simulated and measured reflection coefficients for near-normal incidence. The performance has been verified at 10 degrees. The absorber is in standard A4 size, and the radius of the wooden arch is 1.35 m. Due to the ultra-wide operation bandwidth, two pairs of ridged horn antennas are used to cover the spectra of 2–8 GHz and 6–20 GHz respectively.

4.5 Conclusion

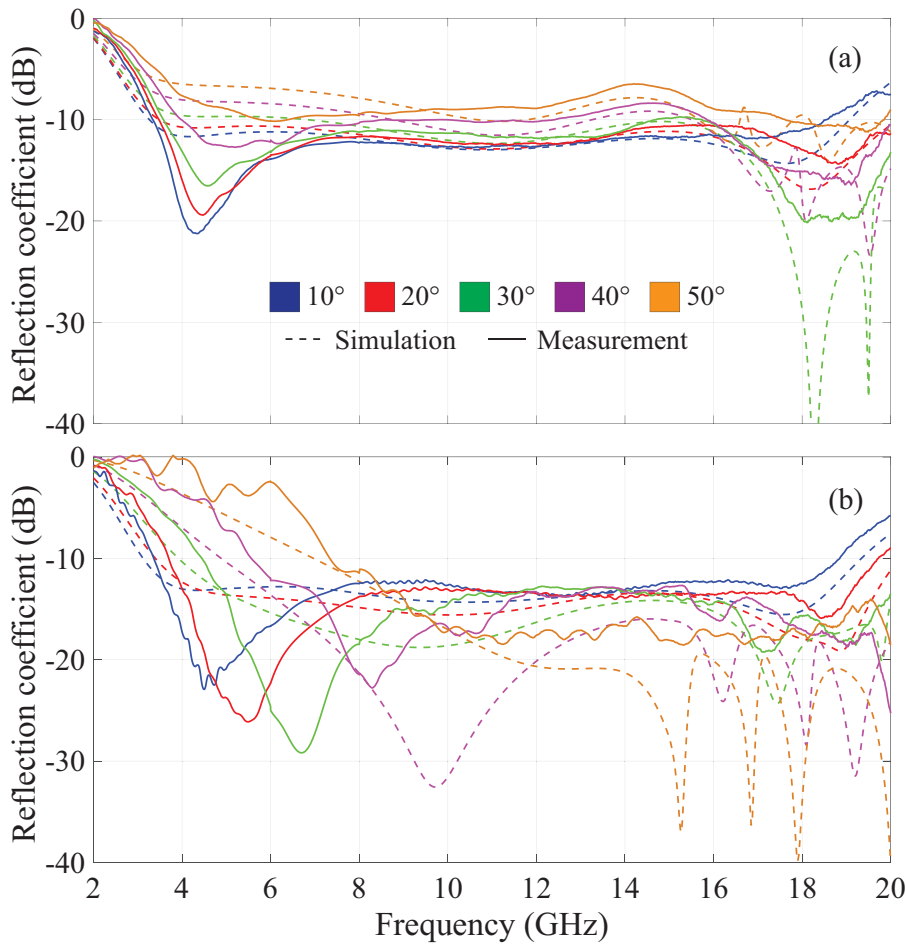


Figure 4.12. Proposed absorber under oblique incidences for (a) TE and (b) TM modes. The performance has been verified under incidence from 10 to 50 degrees.

contributes to the miniaturization of the FSS, which can alleviate a degradation in performance under oblique incidence [25,36].

4.5 Conclusion

A semi-analytical approach has been proposed for efficiently and effectively synthesizing single-FSS-layer absorbers. By integrating the transmission line theory and empirical characteristics of an FSS (i.e., linearity, independence and scalability), the number of seed simulations required for multi-regression has been dramatically reduced. Considering a sample size of 15 for each design variable for example, the semi-analytical algorithm runs approximately a million times faster than the parametric sweep in a

full-wave simulator. This fast calculation enables near global optimization that exhausts the potential of the considered FSS shapes for maximal absorption bandwidth-thickness ratio. With the aid of the GA, achievable bandwidth-thickness curves can be obtained for selected absorber topologies of fundamental FSS shapes. By comparing to existing absorbers proposed in the literature, the better bandwidth-thickness ratios indicate that more complicated and calculation-intensive FSS patterns may not necessarily ensure better absorption performance.

For verification, a wideband single-layer CA absorber has been fabricated and measured under oblique angles of incidence. The agreement between simulation and measurement has verified the reliability and robustness of the proposed semi-analytical method. The realized absorber prototype exhibits a very wide measured operation band of approximately 144% (at 10 dB absorption) while maintaining a small thickness of less than $0.1\lambda_L$, which outperforms the single-FSS-layer absorbers in the literature. In practice, the semi-analytical algorithm is not only efficient for designing CA absorbers, but also for other FSS based structures such as spatial filters or reflectarrays.

Terahertz Absorber with Sub-Skin-Depth Metal

RESISTIVE surfaces are frequently used as lossy layers constituting planar absorbers for microwave applications. Despite that, resistive materials are not common in microfabrication processes. In this chapter, we propose a means to achieve of controlled surface resistance using sub-skin-depth metal for circuit analog (CA) absorber designs at terahertz frequencies. The Drude model is adopted to accurately determine the frequency dependent features of metal in the terahertz range. The proposed single-layer absorber is firstly synthesized via equivalent circuit modeling, and then verified with silver and lead square ring in full-wave simulations. With readily available materials, the absorber design adopting simple square ring patterns is predicted to achieve a relative bandwidth of approximately 94% at -10 dB level of reflectivity. The absorption performance is robust to expected fabrication tolerances and stable to oblique incidence.

5.1 Introduction

Electromagnetic absorbers have found a wide range of applications, such as back-scattering suppression in anechoic chambers, electromagnetic interference (EMI) mitigation between wireless communications devices, and resolution enhancement in spectroscopy [35, 53, 54, 59]. Among the commonly proposed physical realizations, the circuit analog (CA) absorber is of high popularity because of its balanced trade-off between thickness and performance (defined by the bandwidth at a given absorption level). The operation spectral range can be broadened by either exploring the topological features of the embedded FSS layer to introduce additional resonances [8–12, 24] or by fully exploiting the low- Q -factor of the existing unit-cell shapes [21, 22, 36, 44]. The latter typically does not increase the complexity of the geometry, but requires an appropriate impedance manipulation of the unit cell with the aid of equivalent circuit modeling and transmission line techniques.

In addition to the equivalent reactive components that depend on the FSS geometry, the resistive components are crucial to the absorber performance and they can be patterned using lossy inks such as conductive polymer, graphene or silver nanoparticles [22, 35, 39, 48]. As the frequency of interest increases beyond the millimeter-wave range, however, the frequency-dependent material attributes such as conductivity can be significantly different from their values in the microwave range. Fabrication with resistive inks also becomes challenging for accurate periodic patterning at microscale.

Due to fabrication complexity of resistive layers at microscale, a variety of broadband CA absorbers have been proposed in the literature but verified with only full-wave simulated results [60–62]. To ease experimental validation, as a compromise, broadband absorbers for the terahertz spectrum have been realized by classic Jaumann layers adopting novel materials with no patterning [63], or 3D FSSs which are indeed a variant of pyramidal prototypes [64]. CA absorbers with resistive patterns compatible with microfabrication technologies are of great interest to improve absorption performance.

In this chapter, we focus at the spectrum between 200 and 400 GHz in the terahertz frequency range. This band overlaps with an atmospheric window and therefore is envisaged for various short-range wireless applications. Therefore, we propose to control surface resistance by exploiting sub-skin-depth thickness of a noble metal in common

microfabrication processes. The metallic FSSs will be sub-micron thick, which is significantly smaller than the wavelength at the highest operation frequency, thus the approximation regarding thin resistive sheet stands. For realistic and accurate computations, the Drude model [65] is applied in all simulations. Moreover, a dielectric superstrate is adopted to protect the metal layer, to improve impedance matching to the free space, and to enhance absorption performance at oblique incidence [22, 25]. Aiming for a 10 dB level of absorption, the proposed single-FSS-layer absorber is designed for a wide relative bandwidth of approximately 94% ranging from 165 to 460 GHz.

5.2 Metallic FSS-Based Terahertz Absorber

5.2.1 Equivalent Circuit Analysis and Synthesis

The proposed absorber design is illustrated in Fig. 5.1 (a) via an exploded view. Each unit cell comprises a grounded substrate, a metallic square ring array in sub-skin-depth thickness, and a dielectric superstrate. The corresponding transmission line topology in Fig. 5.1 (b) and the equivalent circuit model for the FSS branch in Fig. 5.1 (c) are obtained from physical considerations. The capacitance and inductance are dependent on only the dimensions of the square ring: C_1 and C_2 are created between gaps perpendicular to the electric field, whilst L is obtained along the strips parallel to the electric field. The resistances R_1 and R_2 are not only associated with the FSS geometry, but also controlled by the thickness of the metallic layer. This metallic layer is designed to be much smaller than the skin depth $\delta = 1/\sqrt{\pi f_H \mu_0 \sigma_{dc}}$ at the highest operation frequency f_H , where μ_0 is the free space permeability and σ_{dc} is the DC conductivity of the selected metal [66]. Taking silver (Ag) as a practically relevant material for the FSS, the skin depth at 500 GHz is approximately 84 nm. The perfectly conductive ground can be approximated by a 300 nm gold layer, which is significantly thicker than its skin depth across the operation spectrum.

In the terahertz spectrum, the classical first-order Leontovich boundary condition is however inaccurate for surface impedance estimation as the quasi-PEC assumption becomes invalid. Therefore, the Drude model for the high-frequency response of noble metals should be applied. Although the surface impedance Z_s is frequency dependent, its variation is not significant in the considered frequency range. On this basis, it can

5.2 Metallic FSS-Based Terahertz Absorber

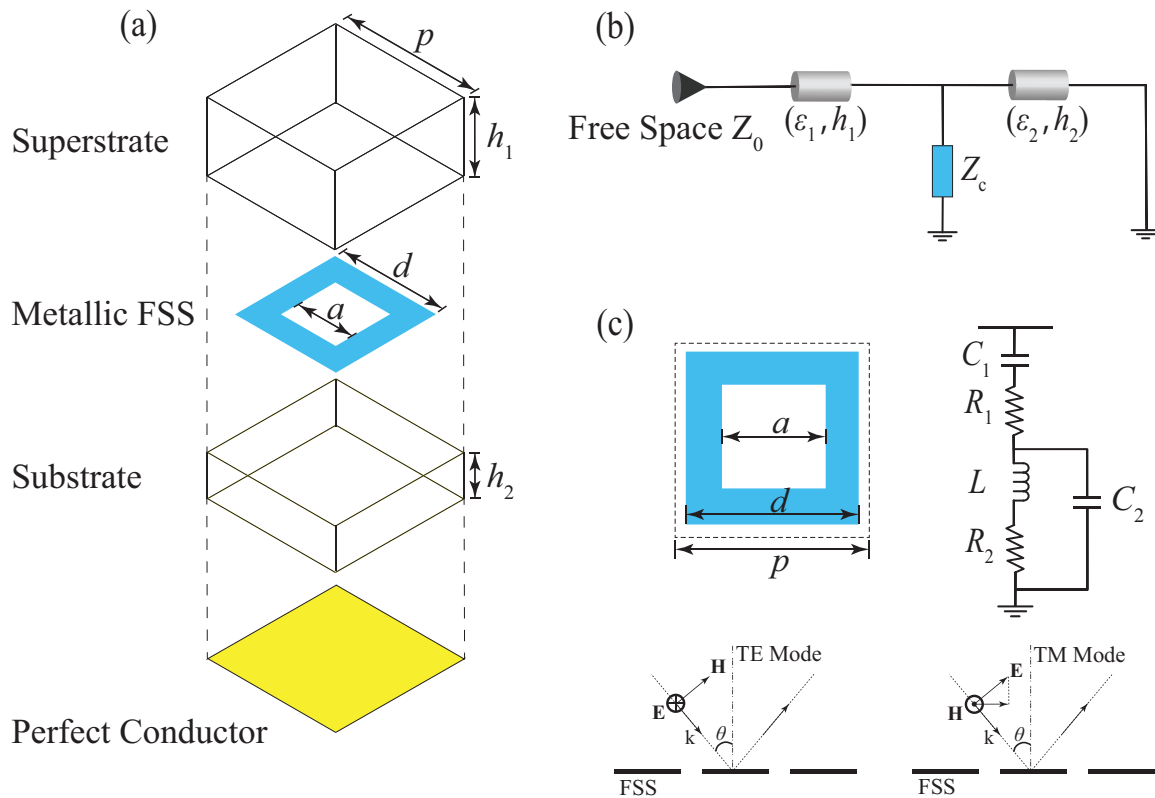


Figure 5.1. Unit-cell schematic of a square ring based single-FSS-layer absorber. (a) Exploded view; (b) generic transmission-line topology; (c) equivalent circuit branch for the periodic array.

be firstly assumed as a constant to simplify the equivalent circuit optimization and absorber synthesis. In later stages, calculations can be refined using frequency-dependent models to finalize the design.

The optimization begins with the circuit model which then guides the synthesis of the FSS geometry considering the inter-dependence between equivalent lumped elements. With the aid of the semi-analytical approach as demonstrated in Chapter 4, the circuit and geometric parameters for 10 dB absorption in the spectral range from 200 to 400 GHz can be easily obtained. It should be noted that the air spacer as substrate for microwave applications is replaced with the nearly lossless supporting dielectrics, and thus additional seed simulations are required. The values for the equivalent circuit elements are tabulated in Table 5.1, and the realized geometrical dimensions are listed in Table 5.2. The electrical lengths of the transmission lines omitted in Table 5.1 can be calculated from the physical thicknesses of the dielectrics as listed in Table 5.2. As shown in Fig. 5.2, the reflection coefficients obtained from the circuit calculation in MATLAB™ and full-wave simulation in HFSS™ agree reasonably well. To ease the

Table 5.1. Equivalent circuit and transmission line characteristics.

R_1 (Ω)	R_2 (Ω)	L (pH)	C_1 (fF)	C_2 (fF)	ε_1	ε_2
104.48	16.96	15.4	7.3	5.56	3.5	3.5

Table 5.2. Structural dimensions and material attributes.

p (μm)	d (μm)	a (μm)	h_1 (μm)	h_2 (μm)	R_s (Ω/\square)
193.4	163.2	121.6	94.3	73.6	16.5

fabrication, the dielectric substrate and superstrate both adopt polyimide. It is worth noting that to cope with possible fabrication imperfections, about 15% tolerance in band edges, as well as 2% tolerance in absorption level are applied.

5.2.2 Surface Impedance of Sub-Skin-Depth Metals

To realize the optimal surface resistance R_s , we can adopt a thin layer of noble metal with a sub-skin-depth thickness. At terahertz frequencies, the damping effect of electrons must be accounted for, and therefore, the frequency-dependent complex dielectric permittivity of the metal can be represented as [65]:

$$\varepsilon(\omega) = \varepsilon_\infty - \frac{\omega_p^2}{\omega^2 + j\gamma\omega}. \quad (5.1)$$

For Ag: $\varepsilon_\infty = 4$, $\omega_p = 1.38 \times 10^{16} \text{ s}^{-1}$; $\gamma = \gamma_1 + \beta\omega^2$, $\gamma_1 = 2.73 \times 10^{13} \text{ s}^{-1}$, and $\beta = 5.9 \times 10^{-18} \text{ s}^{-1}$ [65]. In the full-wave simulator HFSSTM, silver can then be described by the calculated frequency-dependent relative permittivity $\Re\{\varepsilon(\omega)\}$, and the conductivity $\sigma = -\omega\Im\{\varepsilon(\omega)\}$, as illustrated in Fig. 5.3.

To obtain the desired surface resistance in Table 5.2 (i.e., $16.5 \Omega/\square$), the thickness of the silver layer can be approximated by $1/(R_s\sigma) = 1 \text{ nm}$, which specifically results in a sheet impedance changing from $16.17+j0.61 \Omega/\square$ to $16.02+j1.68 \Omega/\square$ in the operation spectrum from 165 to 460 GHz. As shown in Fig. 5.4, this small spectral variation does not significantly affect the overall performance. Nonetheless, precisely fabricating a 1 nm silver layer is challenging.

5.2 Metallic FSS-Based Terahertz Absorber

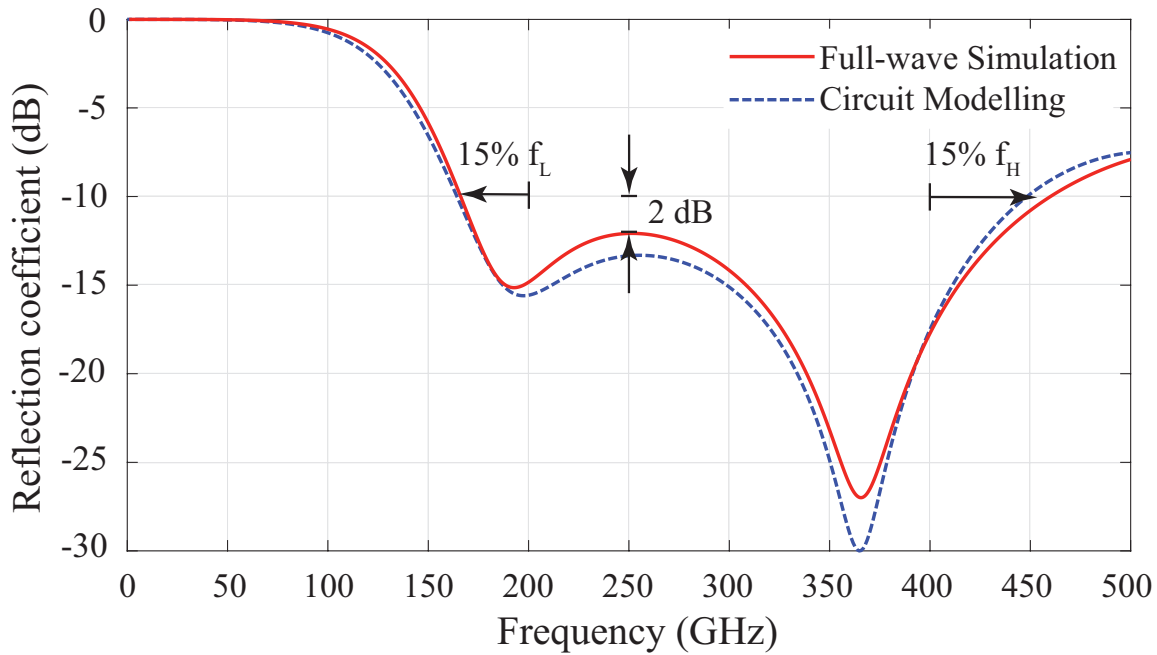


Figure 5.2. Simulated and calculated reflection coefficients for the proposed design. The tolerances introduced in the design are indicated with arrows.

Considering the fact that the resistivity of silver is not high enough below 1 THz, lead (Pb) is considered as an alternative, since it is a more lossy metal suitable for future experimental validation. Similar to silver, the variations of permittivity and conductivity for lead are limited in the operation frequency range, thus its Drude model can be simplified with constants (i.e., $\sigma = 4.5 \times 10^6 \Omega^{-1}\text{m}^{-1}$, $\epsilon = -1800$ [66]) without affecting accuracy. The required thickness is then 13.5 nm, which specifically results in a sheet impedance varying between $16.46 + j0.07 \Omega/\square$ to $16.46 + j0.19 \Omega/\square$ in the targeted spectrum in the terahertz range.

5.2.3 Reliability Evaluation

In practice, the microfabrication technology for FSS lateral features is highly accurate. Thus, for simplicity, it is assumed that the fabrication imperfections mainly come from depositing the metallic FSS to a certain sub-skin-depth thickness and spin-coating the dielectric substrates and superstrates for a given thickness. As shown in Fig. 5.5, with $\pm 5\%$ tolerance in h_1 , h_2 , and the thickness of the metal deposit l , the performance remains largely preserved over the nominated bandwidth from 200 to 400 GHz at -10 dB level of reflectivity.

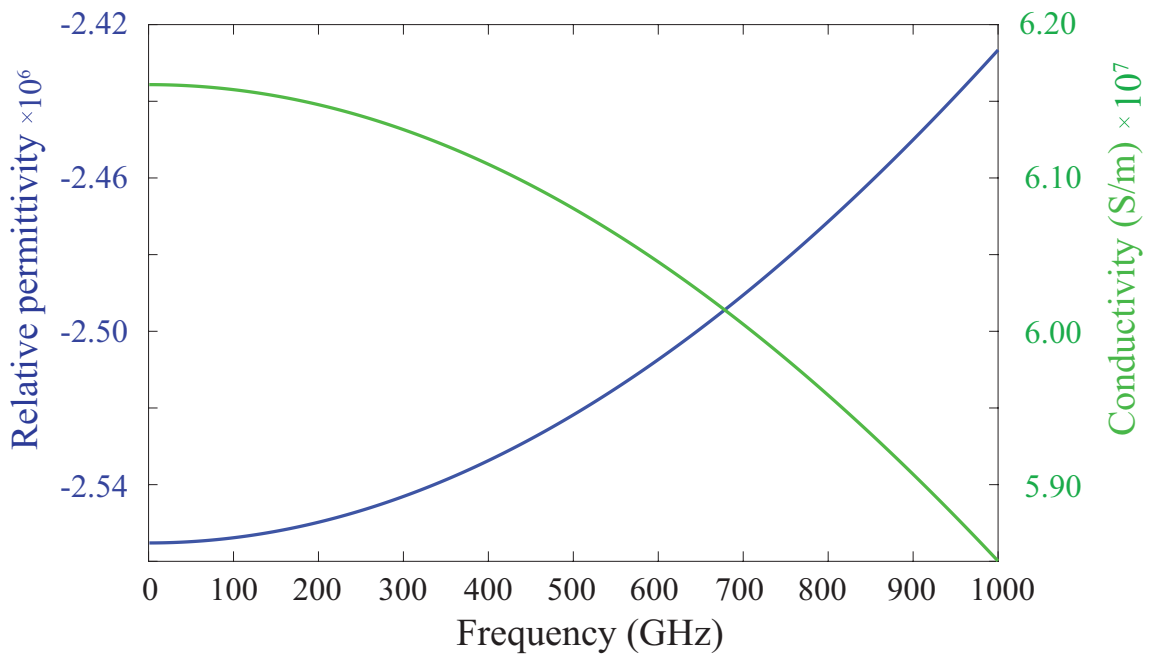


Figure 5.3. Frequency-dependent relative permittivity and bulk conductivity of silver (Ag).

The curves are obtained based on the Drude model up to 1 THz.

The sensitivity to TE and TM oblique incidence is demonstrated in Fig. 5.6, demonstrating that the 10 dB absorption bandwidth is not significantly deteriorated up to an incidence angle of 40 degrees for both the TE and TM modes. Typically, it is observed that under oblique incidence the absorption level is reduced for the TE modes, while the operation spectrum is shifted to the right for the TM modes.

5.3 Conclusion and Validation Progress

A concept of CA absorber is proposed in this chapter for terahertz waves. Instead of using lossy printing inks, an appropriate surface resistance can be attained by implementing a metallic layer with a sub-skin-depth thickness, using metal such as Ag or Pb. Considering the frequency-dependent characteristics of metals, the Drude model has been applied. The predicted 10 dB absorption bandwidth ranges from 165 to 460 GHz, equivalent to approximately 94%. The design can tolerate potential fabrication imperfections and is not strongly sensitive to TE and TM oblique incidences.

A few preliminary results have been collected for experimental validation, and the level of reflection is at approximately -5 dB. Such disagreement in simulation and

5.3 Conclusion and Validation Progress

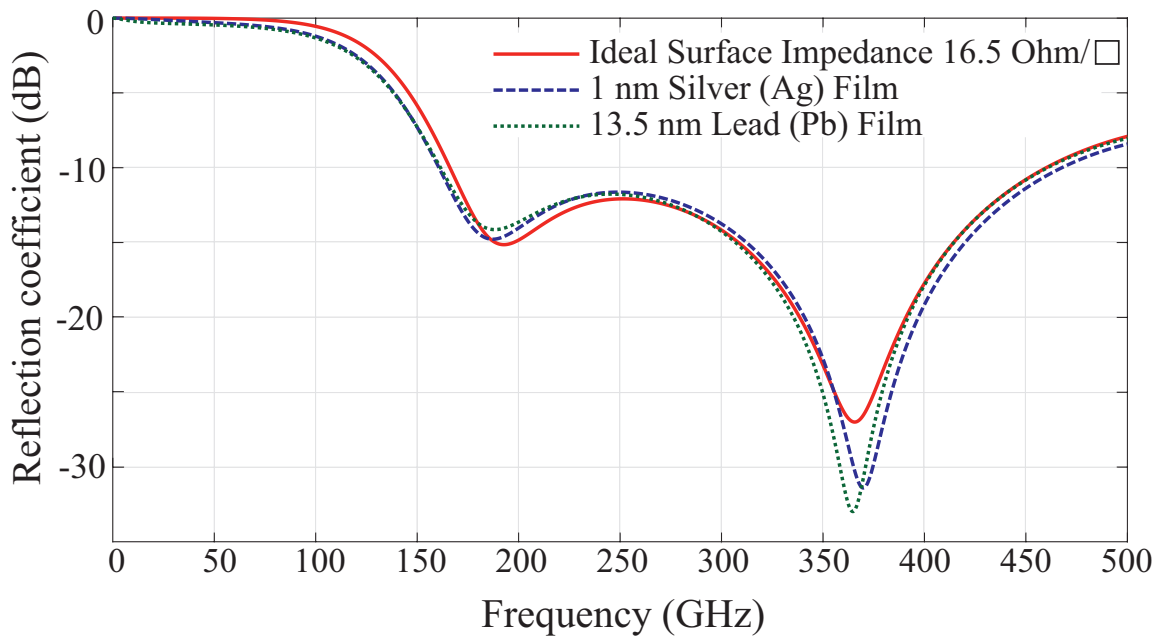


Figure 5.4. Comparison between simulated reflection coefficient for the proposed design adopting different resistive materials for the FSS. The absorption performance is slightly impacted by the choice of accessible metals of various conductivity.

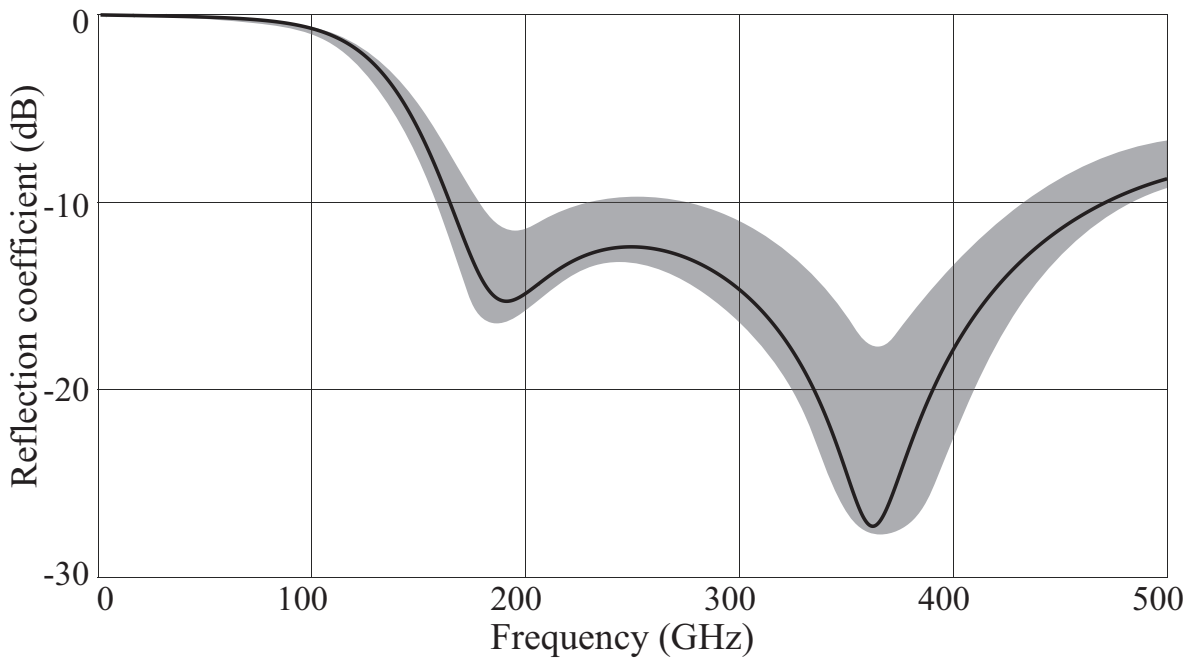


Figure 5.5. Simulated reflection coefficients for geometric imperfections. The shading area indicates the range of variation in absorption performance due to fabrication tolerances in thicknesses of the superstrate, substrate and metallic FSS by $\pm 5\%$.

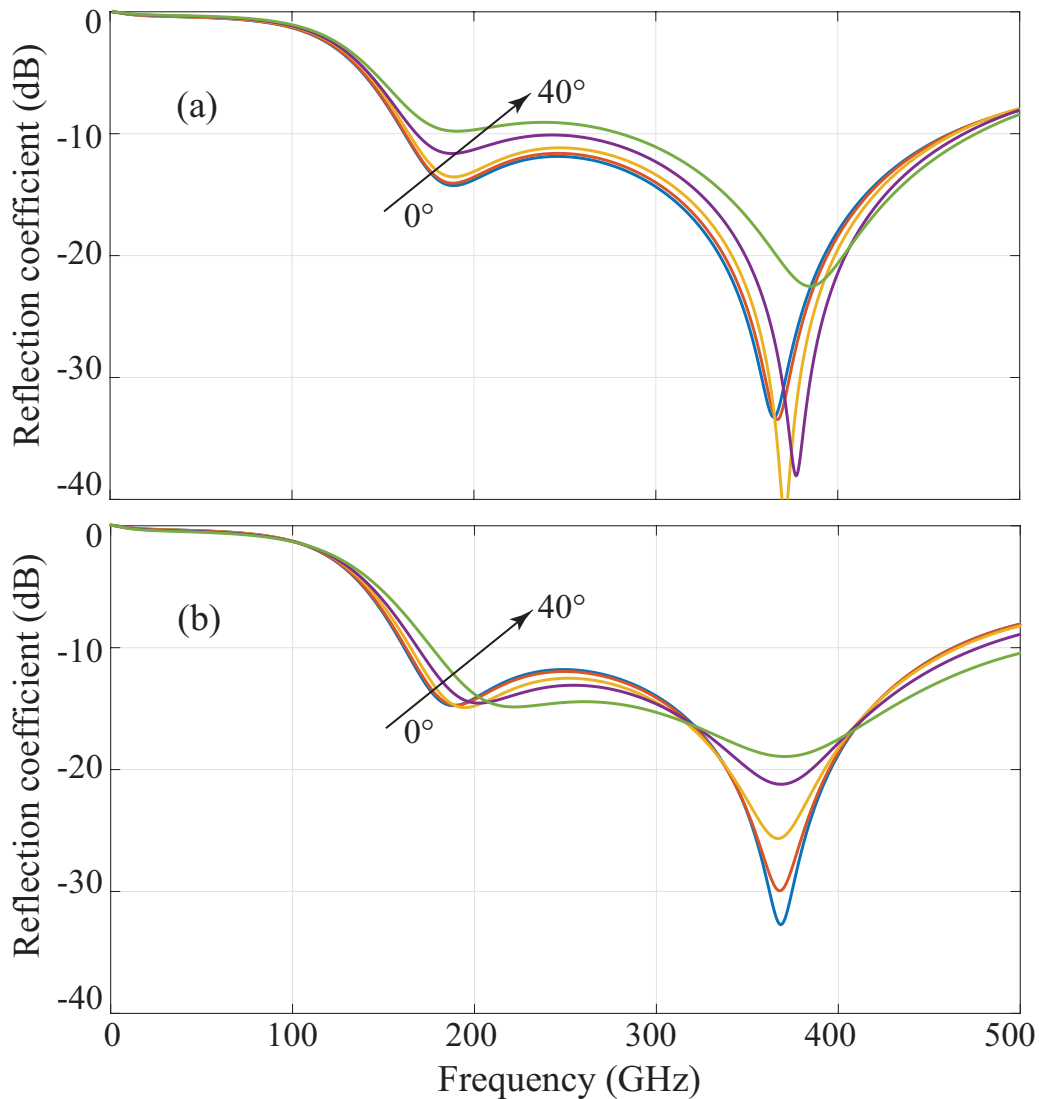


Figure 5.6. Simulated reflection coefficients. (a) TE and (b) TM modes under oblique incidences up to 40 degrees with a step of 10 degrees.

measurement could originate from the uncertainties in the realized sub-skin-depth metal thickness and the metal properties. The requirement in metal layer thickness is less stringent for typical lossless FSS structures where the performance is not significantly affected as long as their metallic patterns are much thicker than a skin depth. In addition, metal properties are informed by different sets of parameters for the Drude model that are found in the literature due to different metal fabrication techniques and various measurement approaches. To ensure agreement in modeling and experiment, the follow-up tasks will start with testing a series of Salisbury absorbers adopting homogeneous metal layers in sub-skin depth thickness. Based on this information, the

5.3 Conclusion and Validation Progress

proposed terahertz absorber can be designed accordingly assuming that the fabrication process is reproducible. This will be the subject of future work.

Mechanically Reconfigurable Terahertz Bandpass Filter

FREQUENCY tunable filters are in demand for applications requiring high spectral selectivity in a broad bandwidth. To this end, frequency-selective surfaces (FSSs) have been widely applied at microwave frequencies for spatial filtering, and varactors well serve the purpose for electronic reconfiguration. For terahertz applications, however, varactors in micron scale are unavoidably lossy to provide sufficiently small capacitance. In this chapter, we propose a terahertz bandpass multi-layer FSS with a finesse around 20 with 80% power transmission, while its operation frequency is tunable in a 40% frequency range by varying an inter-layer spacer thickness. The filter is insensitive to misalignment and can maintain tunability under oblique angles of incidence. The design has been fabricated and experimentally verified. The measured results closely match the simulated transmission performance, and outperforms a series of notable reconfigurable filters available in the literature. The proposed design is among the first few reconfigurable terahertz filters and the methodology can be readily applied to other FSS-based structures.

6.1 Introduction

Filters are among the most commonly embedded components in communications devices. As opposed to a digital filter, a circuit-based analog filter achieves latency-free response without adopting a powerful chip and, more importantly, it is free from frequency aliasing. FSSs are periodic arrays that can be explicitly analyzed and synthesized via equivalent circuit models with physical insights into their unit-cell geometries. Therefore FSS-based structures have been widely applied for spatial filtering, including but not limited to radar cross-section (RCS) reduction, radio-frequency interference (RFI) mitigation and electromagnetic compatibility (EMC) [67].

FSS filters of high Q-factors, for example, are in demand in high-quality terahertz communications [68], but their frequency band of operation is typically fixed. To adaptively cover a broad terahertz spectrum, a series of narrowband filters can be attached to a rotating wheel [42]. However, such tunability is limited to a number of pre-determined discrete frequencies rather than a continuous frequency sweep. This motivates the design of a continuously reconfigurable bandpass filter in a wide terahertz frequency range with high selectivity. An FSS-based spatial filter interacts with impinging waves from free space. Therefore, its stability to oblique incidence angles and insensitivity to polarizations are essential [69,70]. Desirable filtering performance, such as fast roll-off transitions, can be straightforwardly obtained by stacking multiple FSS layers for high-order frequency response characteristics [32,71,72].

To obtain reconfigurability, a tuning mechanism for the unit-cell characteristics is required [1]. In the microwave frequency range, a well developed approach is by adopting semiconductor elements such as PIN diodes or varactors because of their low cost, high response speed and broad dynamic ranges [43]. However, a dedicated bias network is difficult to realize considering the large number of unit cells, and this additional metallic structure will also unavoidably affect the frequency response of the filter [43,73,74]. At terahertz frequencies, the cross-sectional area of a varactor is extremely small to deliver required capacitance but in turn elevating series resistance. An alternative tuning method is to adopt novel phase-change materials (PCMs) such as vanadium dioxide (VO_2) which comes with a temperature-controlled transition between insulator and metal phases [75]. Although an FSS array can be tuned with a contactless meander loop heater, this approach better suits an on/off operation rather

than a dynamic frequency scanning within the spectrum of interest [34]. Combination of semiconductors and infrared photoexcitation can also provide reconfiguration at THz [76], however the spectral reconfigurability is limited.

This chapter proposes a reconfigurable bandpass filter working in a strategic frequency range between 220 and 330 GHz, envisaged for numerous short-range applications. Its spectral tunability is realized by mechanically changing the distance between a pair of identical double-layer FSS structures. The frequency response is narrowband with sharp out-of-band rejection. Its high selectivity is insensitive to polarization and stable to oblique impinging waves. The power transmitted through the filter is above 80% across the tuning spectrum, which is even higher than the vast majority of existing terahertz bandpass filters without reconfigurability. Fabrication tolerances are considered to ascertain a desired frequency response, and the impact of misalignment of the multiple FSS layers has been examined.

6.2 Frequency Reconfigurable Bandpass Filter Design

A unit cell of the proposed frequency reconfigurable bandpass filter is illustrated in Fig. 6.1(a). The design includes two identical double-layer FSSs separated by an air spacer. A capacitive square patch FSS is on one side of the supporting dielectric, whilst on the other side exists an inductive grid FSS. To minimize power dissipation, gold and cyclic olefin copolymer (COC) are adopted for the metallic patterns and dielectric layers respectively. As shown in Fig. 6.1(b), except for the unit-cell period p , only one single design variable is needed for each FSS layer i.e., the gap width g for the square patch and the aperture length a for the grid FSS layer. The capacitance C and inductance L , as shown in Fig. 6.1(c), can be respectively determined by the geometrical parameters g and a . The in-between supporting dielectric also affects the reactive components and is modeled as a transmission line section.

The optimization begins with an equivalent topology including transmission line sections and circuit branches. For simplicity, the dielectrics and the metallic patterns are firstly considered lossless. Aiming for selective bandpass filtering with high power transmission over a broad tuning spectrum, the reactive components and transmission line attributes are optimized in the circuit analyzer ADSTM. Then, each metallic layer can be synthesized by individually matching the S -parameters obtained from the ADSTM and the full-wave electromagnetic solver HFSSTM.

6.2 Frequency Reconfigurable Bandpass Filter Design

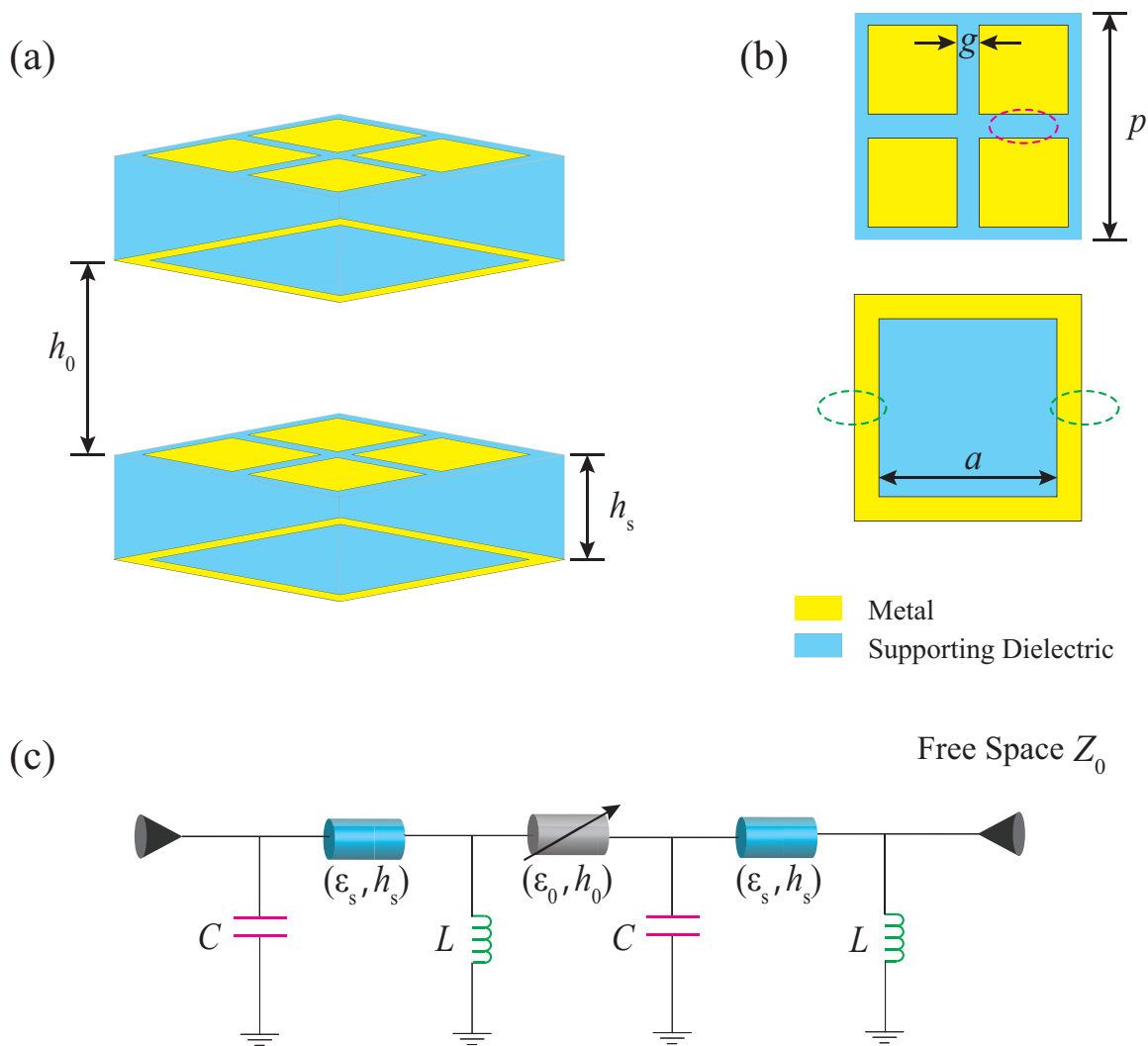


Figure 6.1. Proposed FSS-based frequency reconfigurable bandpass filter. (a) Perspective view of the unit-cell geometry; (b) top view of the FSS patterns; (c) equivalent topology including transmission lines and circuit branches. The optimized inductance L and capacitance C are 31.00 pH and 1.68 fF respectively. Correspondingly, the synthesized dimensional parameters are $p = 246 \mu\text{m}$, $g = 22 \mu\text{m}$, $a = 175 \mu\text{m}$, and $h_s = 120 \mu\text{m}$. Permittivity ϵ_s of the supporting dielectric is 2.34.

As illustrated in Fig. 6.2(a), when the separation h_0 of the paired double-layer FSSs is increased from $h_{\min} = 50 \mu\text{m}$ to $h_{\max} = 400 \mu\text{m}$ with a $50 \mu\text{m}$ step, the transmission coefficients obtained from the ADSTM and the HFSSTM fit closely. Here, h_{\min} is chosen for sufficient clearance between the two layers, whilst h_{\max} is selected to avoid the onset of a higher-order mode. A tiny shift between the circuit and full-wave results can be observed due to the simplification of the circuit models. Specifically, there is a small inductance in series to C for the square patch FSS, as well as a small capacitance in parallel to L for the grid FSS.

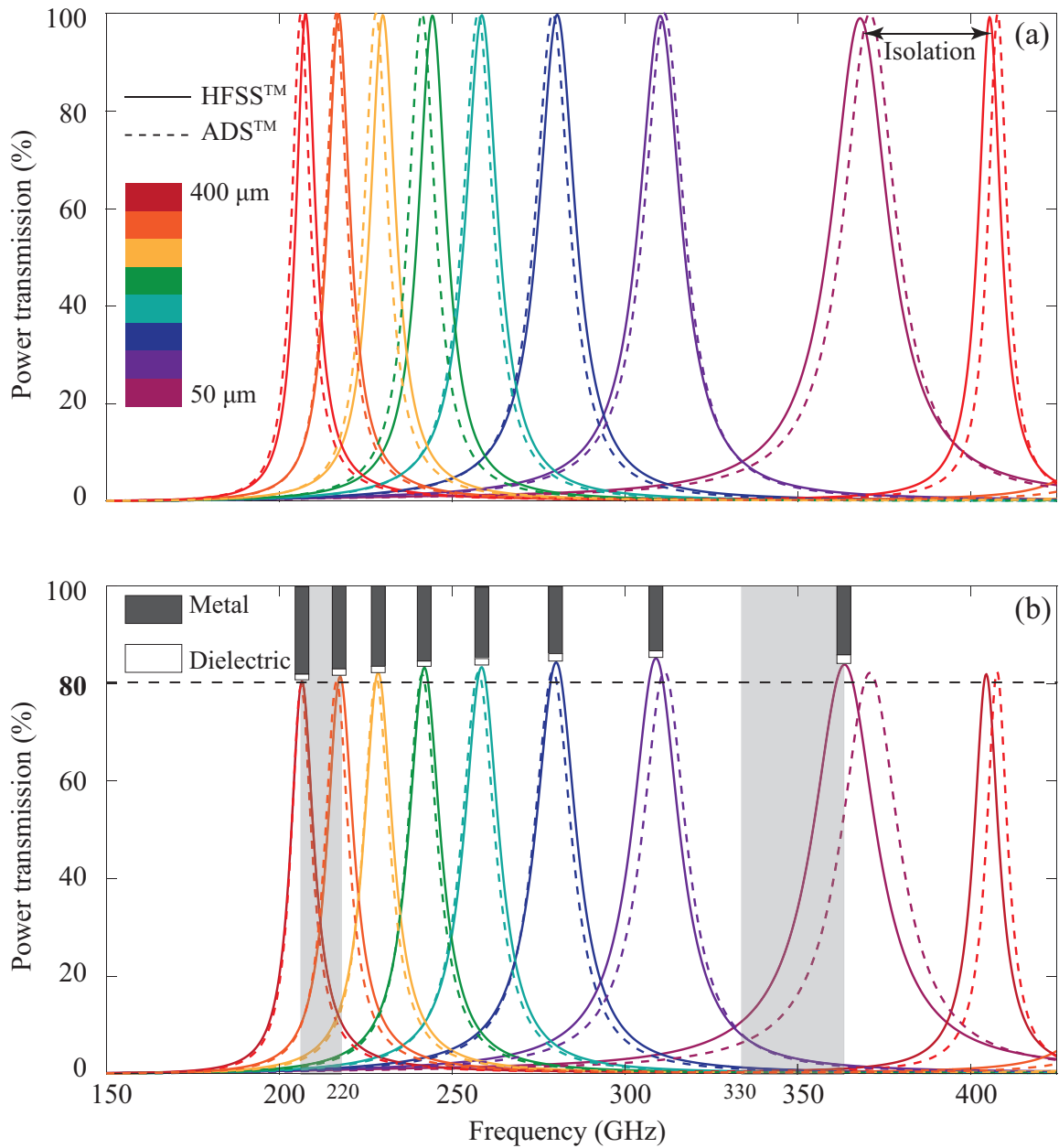


Figure 6.2. Power transmission of the proposed tunable FSS. (a) Initial lossless models; (b) realistic models accounting for material losses. The color shading indicates a variation of air spacing from 50 to 400 μm with a step of 50 μm . The dark and white shades indicate the proportion of loss from the metallic FSS pattern and the dielectric substrate respectively. The objective frequency range is between 220 and 330 GHz, and the buffering bands (grayed out) are reserved at the band edges.

Although 300 nm for the gold FSS patterns is much thicker than the skin depth (161 nm at 220 GHz) within the spectrum of interest, the surface impedance remains complex and cannot be ignored. Also, the loss tangent $\tan\delta_s = 0.0007$ of the COC needs to be taken

6.3 Insights into Selectivity and Reconfigurability

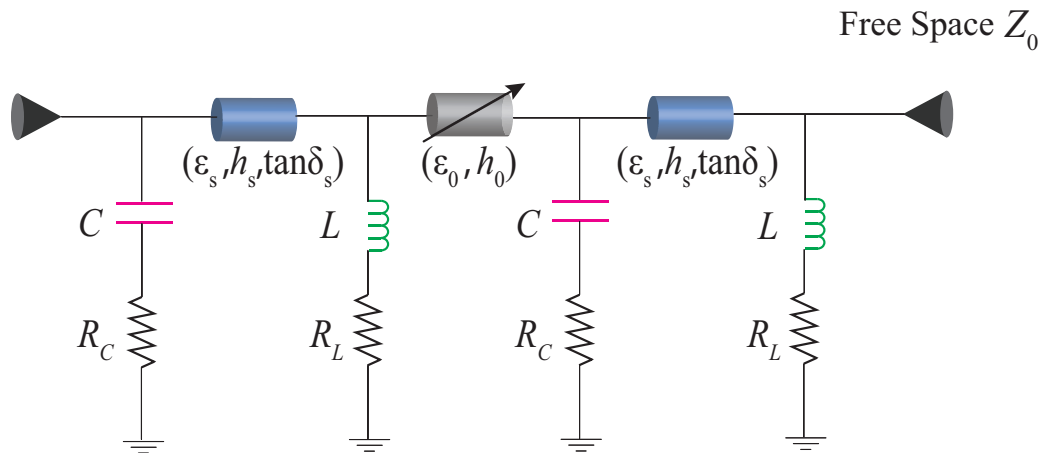


Figure 6.3. Modified equivalent circuit including lossy transmission line sections and RLC branches. R_C and R_L are determined by the surface impedance of gold and the FSS patterning, whilst the loss tangent $\tan\delta_s$ of the COC spacers also contributes to the power attenuation.

into consideration. As demonstrated in Fig. 6.2(b), the final design accounting for material losses reaches 80% power transmission over the frequency tuning range from 220 to 330 GHz. Wide spectrum margins for the reconfiguration spectrum are preserved for any possible imperfections in fabrication and assembly. Figure 6.3 is modified based on Fig. 6.1(c), where the equivalent lumped resistances $R_C = 1.68 \Omega$ and $R_L = 0.58 \Omega$ are included and the transmission line is characterized with attenuation.

6.3 Insights into Selectivity and Reconfigurability

In this section, the physical mechanisms of the highly selective reconfigurable band-pass filter will be explained from the multiple-path interference and impedance matching perspectives. In addition to the equivalent circuit modeling, these techniques can aid understanding and support the design process.

6.3.1 Fabry-Perot Resonance Cavity

The overall structure can be considered as a Fabry-Perot resonance cavity as shown in Fig. 6.4. According to the law of energy conservation, the power transmission can be maximized when the multiple reflected waves result in destructive interference. Unlike a common Fabry-Perot cavity, however, the FSS patterns on both sides of the COC are different, thus the reflectivity of the proposed design is direction dependent. More

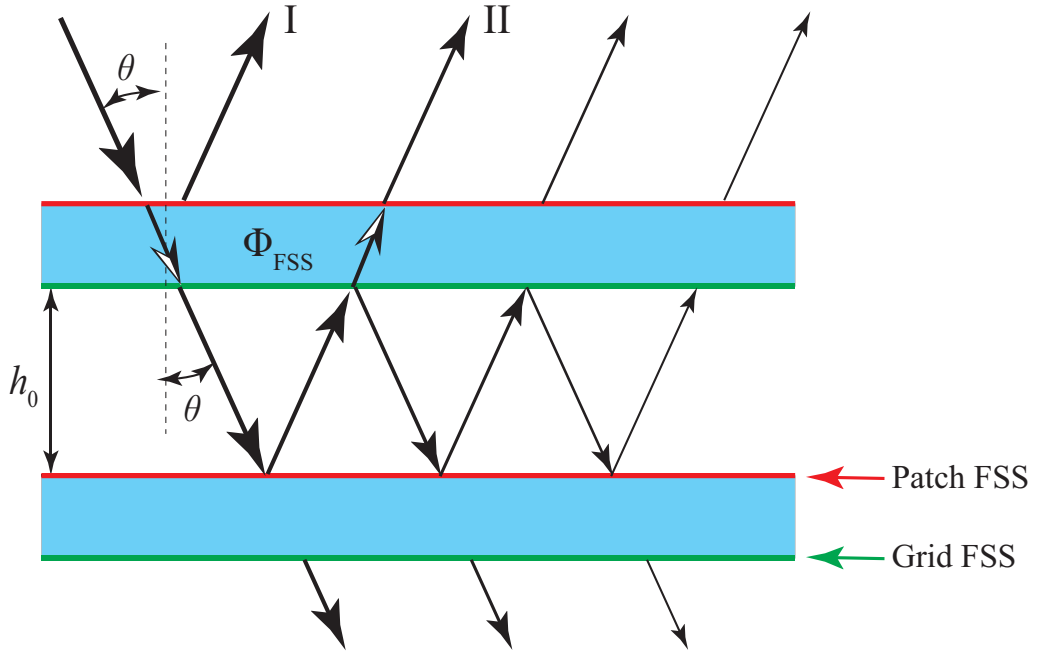


Figure 6.4. Multiple-beam interference in the proposed Fabry-Perot resonance cavity. The proportion of energy conveyed in each beam is visualized by the thickness of arrow. The reflection phase change at the upper patch FSS for path I is balanced out by the reflection phase change at the lower patch FSS for path II thus neither are represented in E.q. (6.1).

importantly, the double-layer FSS can delay or advance the phase of a transmitted wave. For perfectly destructive interference, the phase difference between path I and II must be π rad. Therefore, under normal incidence (i.e., $\theta = 0$):

$$2(\Phi_{FSS} - h_0 k_0) = -\pi, \quad (6.1)$$

where Φ_{FSS} is the total phase change per transmission through the double-layer FSS, h_0 is the thickness of the air spacer, and k_0 is the free-space wavenumber. Thus, the thickness of the air spacer h_0 for an operation frequency f_0 can be therefore calculated as:

$$h_0 = \frac{\pi + 2\Phi_{FSS}}{4\pi} \frac{c}{f_0}. \quad (6.2)$$

By de-embedding the Floquet ports to both side of a double-layer FSS, Φ_{FSS} can be extracted from the full-wave simulation. Figure 6.5 includes a non-linear curve depicting the correspondence between the air spacer thickness h_0 and the operation frequency f_0 . It can be used as a mapping tool to precisely indicate the spatial separation of the paired double-layer FSSs for frequency reconfiguration.

6.3 Insights into Selectivity and Reconfigurability

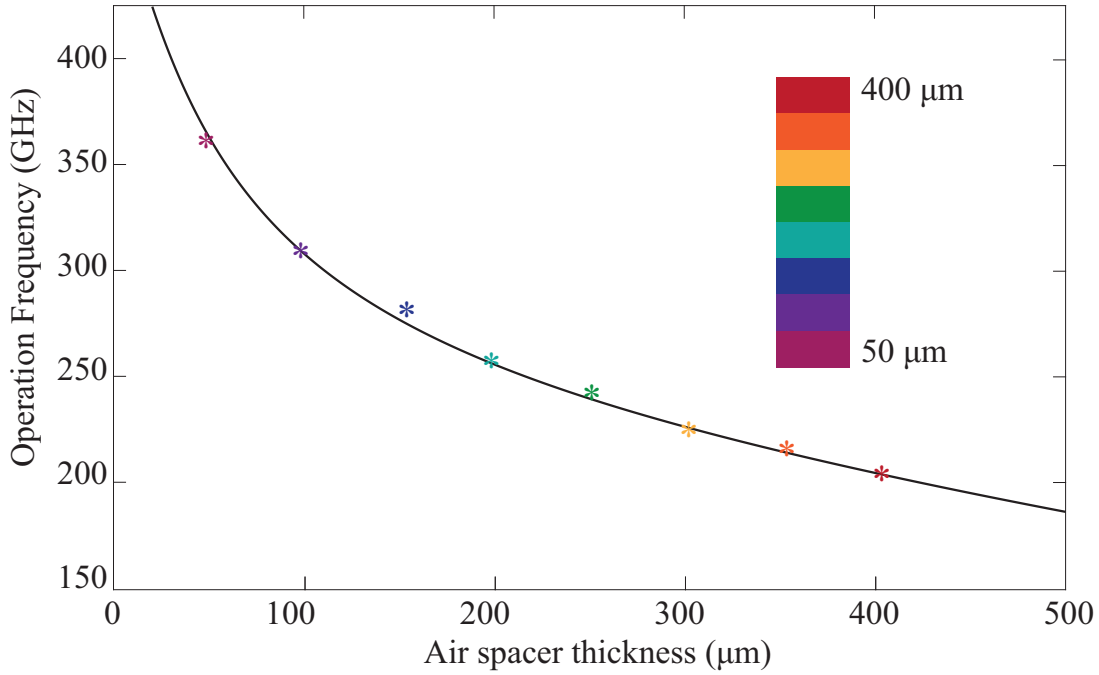


Figure 6.5. Non-linear relationship between the air spacer thickness and the operation frequency. The solid line is from E.q. (6.2). Each scatter point corresponds to an individual curve as shown in Fig. 6.2

The selectivity can be evaluated by adopting the definition of finesse from a Fabry-Perot cavity [77]:

$$\mathcal{F} = \frac{\pi \sqrt{\frac{4\mathcal{R}}{(1-\mathcal{R})^2}}}{2}, \quad (6.3)$$

where \mathcal{R} represents the power reflection of a double-layer FSS from the square patch side. Figure 6.6 includes both \mathcal{R} and \mathcal{F} as functions of the operation frequency. As the double-layer FSS on average attains a high level of reflectivity $\mathcal{R} \geq 0.8$, the selectivity \mathcal{F} of the filter reaches 20 approximately. Because \mathcal{R} of the double-layer FSS remains relatively stable across the operation frequency range, the variation of \mathcal{F} is not significant. Such coherence in selectivity during frequency tuning can be further verified by calculating the full-width at half maximum (FWHM) which slowly varies from 3 to 4% when h_0 increases from 50 to 400 μm .

6.3.2 Impedance Matching with Smith Chart

As mentioned above, to maximize the power transmission in a passband, the reflection needs to be suppressed. In essence, this is an impedance matching problem. The Smith

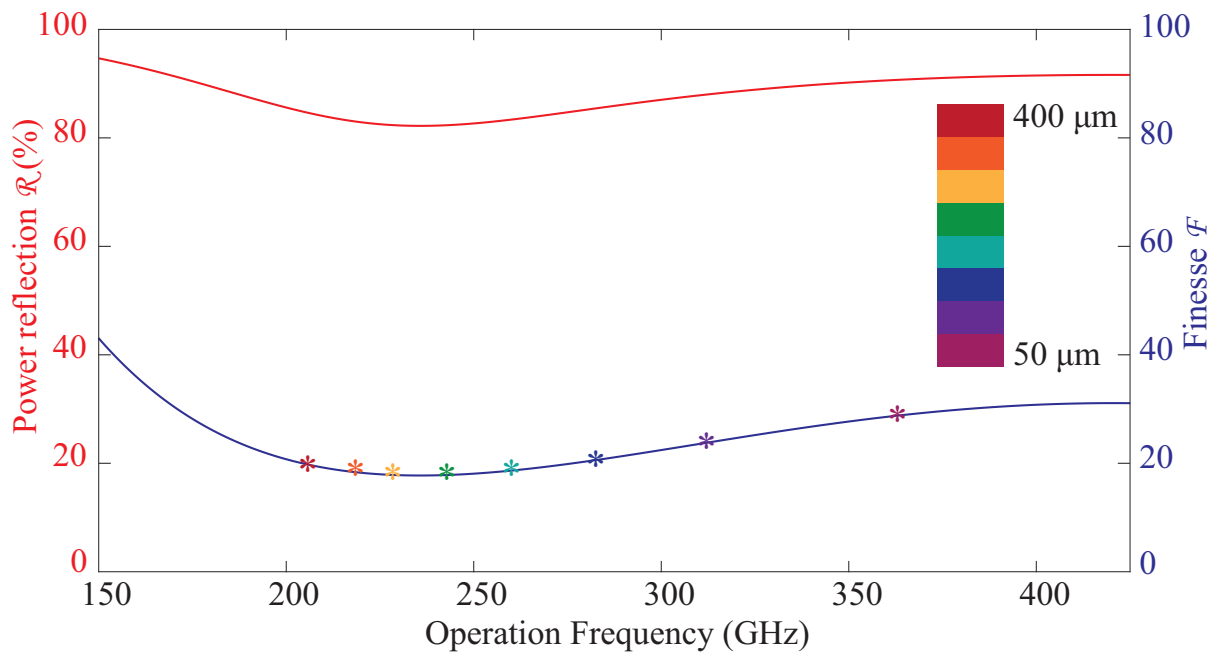


Figure 6.6. Power reflection of the double-layer FSS and finesse of the reconfigurable filter.

The higher power reflection \mathcal{R} results in the higher selectivity \mathcal{F} .

chart provides a visualized solution that allows intuitive manipulation of the locus indicating the reflectivity in the spectrum of interest [1, 21, 22, 25, 36].

As shown in Fig. 6.7(a), the circuit branches are in parallel thus an admittance Smith chart would better fit the demonstration purpose. The loci for input admittance are sequentially obtained at different reference planes as demonstrated from Fig. 6.7(b) to (f). To begin with, the blue locus in Fig. 6.7(b) represents the input admittance of a double-layer FSS plus the semi-infinite free space in the frequency range from 150 to 425 GHz. When adding an air spacer, the power transmission is not affected as shown in Fig. 6.7(c), but however the phase varies and a rotation of the locus can be observed. With an additional grid FSS as shown in Fig. 6.7(d), the locus is rotated anti-clockwise and scaled down to the left half-plane. In Fig. 6.7(e), the COC layer then circulates and stretches the locus to the right half-plane around its normalized admittance $\sqrt{\epsilon_s}$. To achieve a near perfect narrowband impedance matching, the outermost square patch FSS rotates the locus clockwise and precisely makes it just pass through the center of the Smith chart as shown in Fig. 6.7(f). Frequency reconfiguration can be obtained by adjusting the thickness of the air spacer, which is equivalent to a change in the degree of rotation of the locus in Fig. 6.7(c). The ultimate objective is still to ensure that the locus

6.3 Insights into Selectivity and Reconfigurability

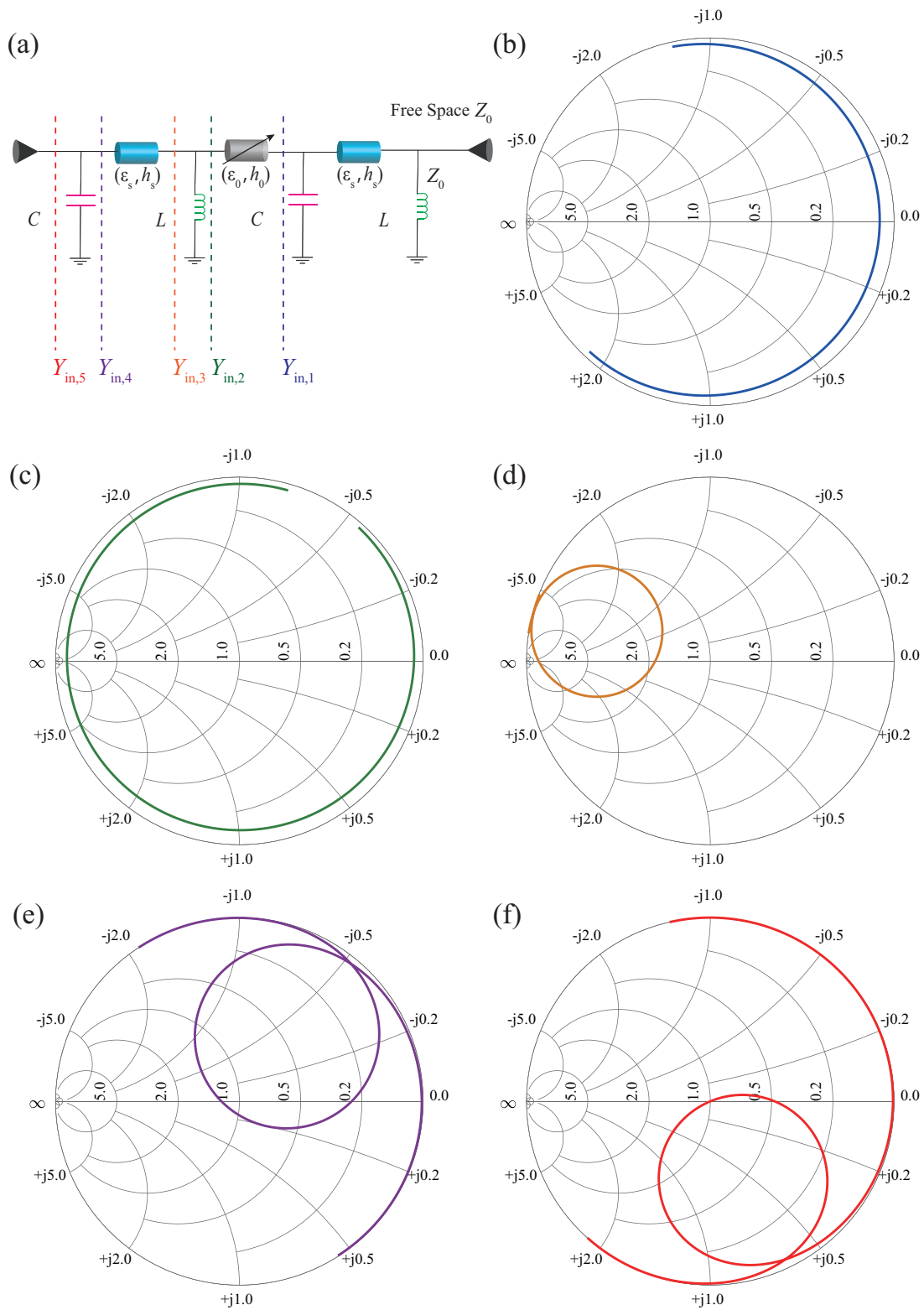


Figure 6.7. Admittance Smith charts for narrowband perfect impedance matching manipulation. The loci span the frequency range from 150 to 425 GHz. Each locus from (b) to (f) corresponds to the input admittance at a different transmission line position, as indicated in subplot (a).

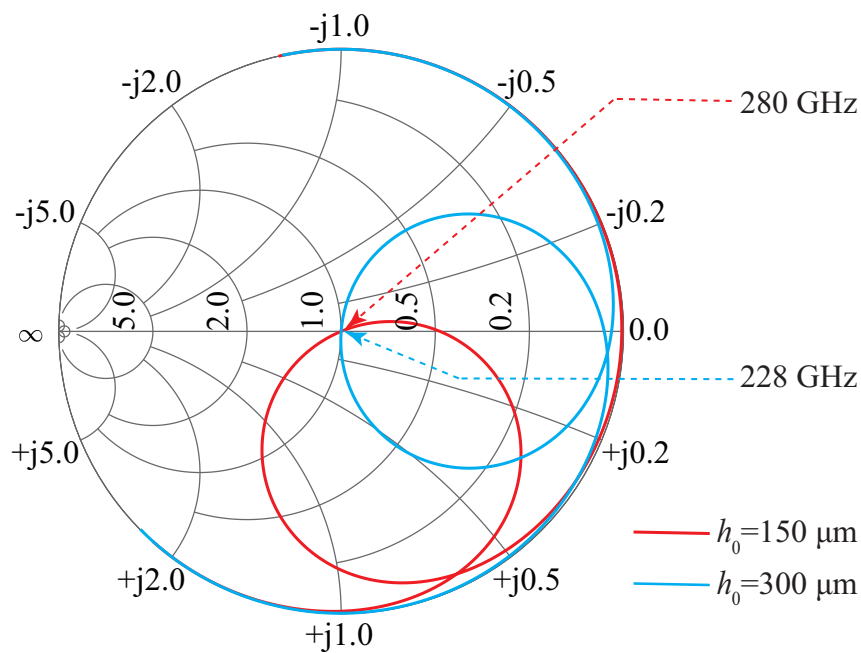


Figure 6.8. Frequency reconfiguration demonstrated with admittance Smith chart. Loci in correspondence to different air spacer thicknesses pass through the center of the Smith chart at different frequencies.

pass through the center of the Smith chart. This tuning results in perfect impedance matching at different frequencies as demonstrated in Fig. 6.8.

Via this interactive approach, a highly selective and frequency reconfigurable band-pass performance can be efficiently obtained for the proposed multilayer FSS-based structure without onerous analytical calculation.

6.4 Robustness and Reliability

6.4.1 Misalignment of Unit-Cell Patterns

In practice, assembly misalignment in multi-layer FSS-based structures is unavoidable, especially when the unit-cell geometries are in the sub-millimeter scale. Without the aid of calibration instruments, it is necessary to examine the robustness of the proposed design by randomly shifting the FSS layers as shown in Fig. 6.9. The impact of rotating the FSSs is negligible as the unit-cell geometries i.e., square patch and grid, are fourfold symmetric thus insensitive to polarization under normal incidence.

Although the corresponding full-wave simulated results in Fig. 6.10 shows a small shift in the transmission peak, the transmission power is still no less than 80% from 220 to

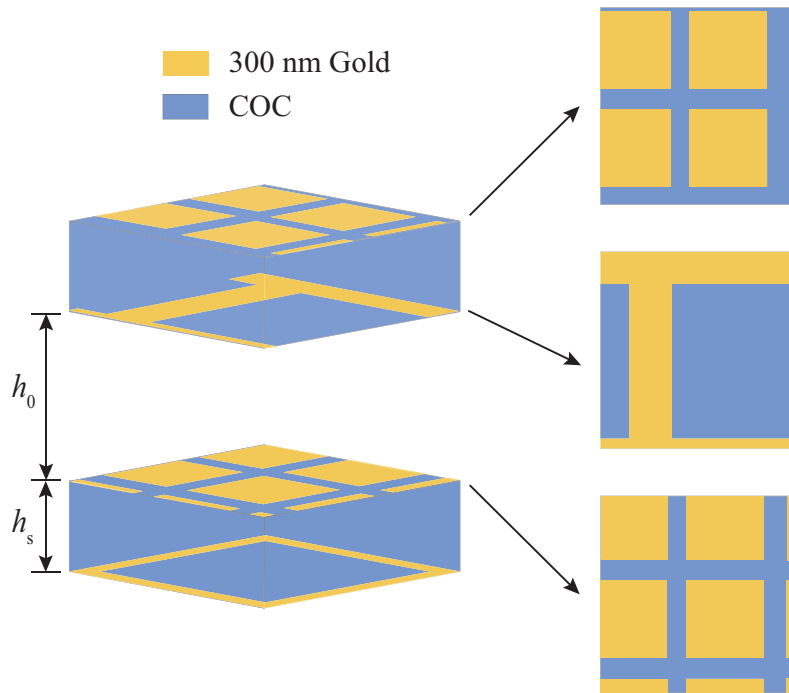


Figure 6.9. Filter assembly with random misalignment of FSSs. The bottommost layer is the reference plane while the other FSSs are horizontally shifted with random two-dimensional vectors.

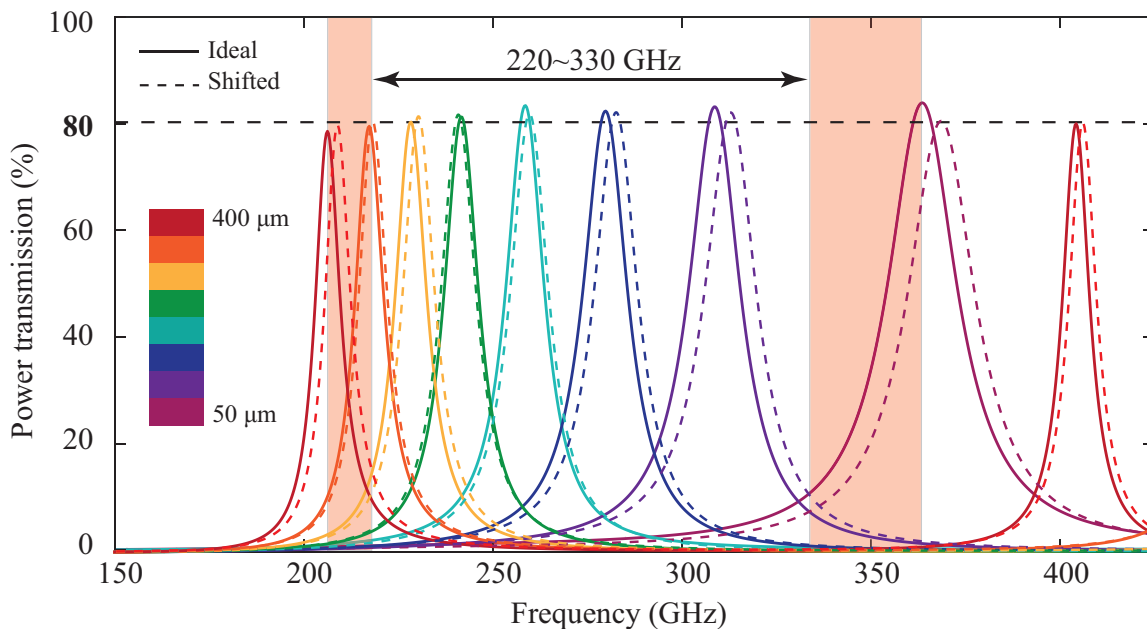


Figure 6.10. Impact of unit-cell misalignment on reconfigurable bandpass filtering. Transmission power is obtained from the full-wave simulator HFSS™ for both the ideal and misaligned assemblies as shown in Fig. 6.9. This outcome is typical because the inter-layer couplings are negligible.

330 GHz. This is not unexpected because the evanescent waves decay quickly away from the periodic arrays [22]. In other words, the FSS layers can be approximated as homogeneous surfaces of complex sheet impedance, where the inter-layer couplings are weak and negligible.

6.4.2 Stability to Oblique Impinging Waves

Under oblique incidence, the lengths of transmission paths for EM waves in the air spacer and the supporting dielectrics will be increased, whilst the equivalent permittivities will be rescaled differently for the TE and TM modes. This prompts the need to verify the stability of the frequency response to oblique impinging waves. The full-wave simulated results, for extreme COC thicknesses h_{\min} and h_{\max} at angles of incidence from 0° to 45° with a 15° step, are illustrated in Fig. 6.11(a) to (d).

Despite the fact that the impact on selectivity is indistinguishable, oblique incidence leads to an upward shift of the operation frequency as commonly seen in FSS-based designs. It also can be observed that the frequency drift is less severe for the TE mode, whilst the level of power transmission for the TM mode remains at least 80%. The proposed design is able to secure the tuning frequency range from 220 to 330 GHz up to 30° . Indeed, by extending the thickness of the air spacer to $500\ \mu\text{m}$ as illustrated in Fig. 6.11(e) to (f), this frequency reconfigurability can be guaranteed up to 45° .

6.5 Experimental Validation

6.5.1 FSS Fabrication and Filter Assembly

Fabrication of the double-layer FSS has been performed by our collaborators at RMIT. The process starts with spin coating a $5\ \mu\text{m}$ COC layer at 3000 rpm on the PMMA (methyl methacrylate)/Si wafer. The grid FSS is patterned on this thin COC base as shown in Fig. 6.12(a). Then, the supporting COC is independently fabricated and bonded to the grid array as shown in Fig. 6.12(b). Lastly, the square patch FSS is added on top of the supporting COC as shown in Fig. 6.12(c), where the grid FSS can be seen in the blurred background. The extra $5\ \mu\text{m}$ COC adopted at the beginning of this process is unavoidable because the sample buildup is one directional and the FSS cannot be free-standing. However, it imposes a negligible effect when attached to the grid FSS side which is inductive thus not sensitive to a change in the adjacent dielectric.

6.5 Experimental Validation

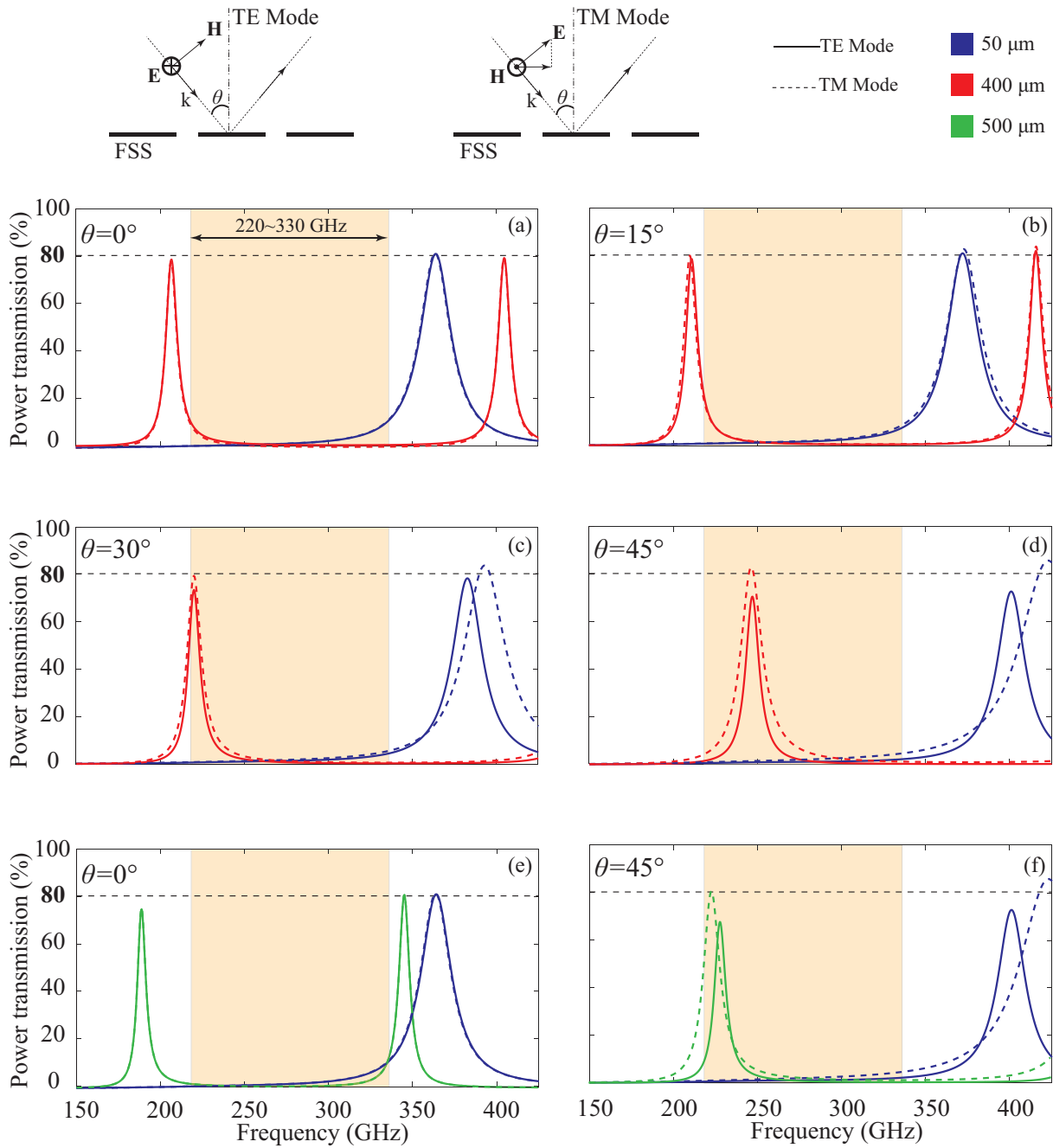


Figure 6.11. Power transmission for TE and TM modes under oblique incidence. different angles of incidence, (a-d) show both modes for $h_{\min}=50 \mu\text{m}$ and $h_{\max}=400 \mu\text{m}$ respectively. Then, the performance for an additional separation $h_0=500 \mu\text{m}$ (black curve) is also included as shown in (e-f), which roughly covers the spectrum of interest.

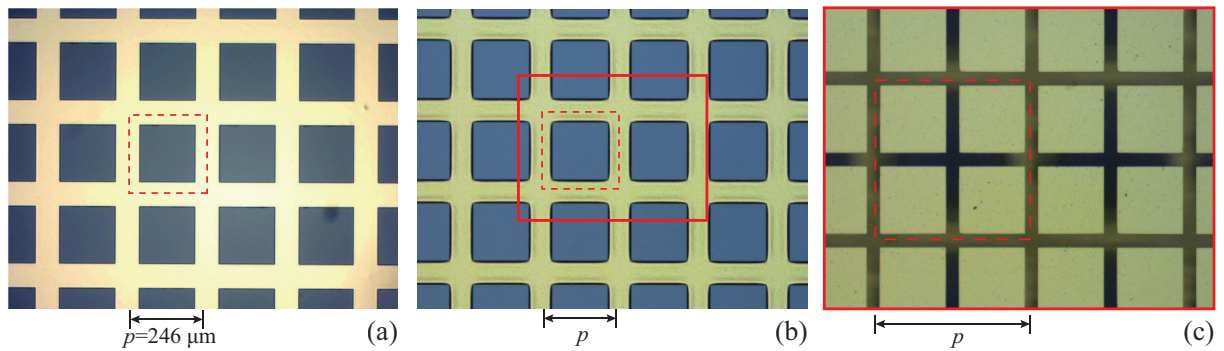


Figure 6.12. Observations under the optical microscope during FSS fabrication process. (a) Grid FSS on a thin COC; (b) thick COC spacer on top of the grid FSS; (c) added square patch FSS. Each dashed red square indicates one unit cell, and (c) corresponds to the solid red rectangular area in (b). All FSSs adopt 300 nm gold as mentioned earlier. Color variation is due to lighting condition.

The schematic diagram for filter assembly is illustrated in Fig. 6.13. The metallic screw holder with etched scales allows a fine tuning of layer separation down to a 10 μm step. However, because of the thickness introduced by the FSS samples, this holder must be carefully calibrated by fitting a pair of measured and full-wave simulated transmission coefficient curves.

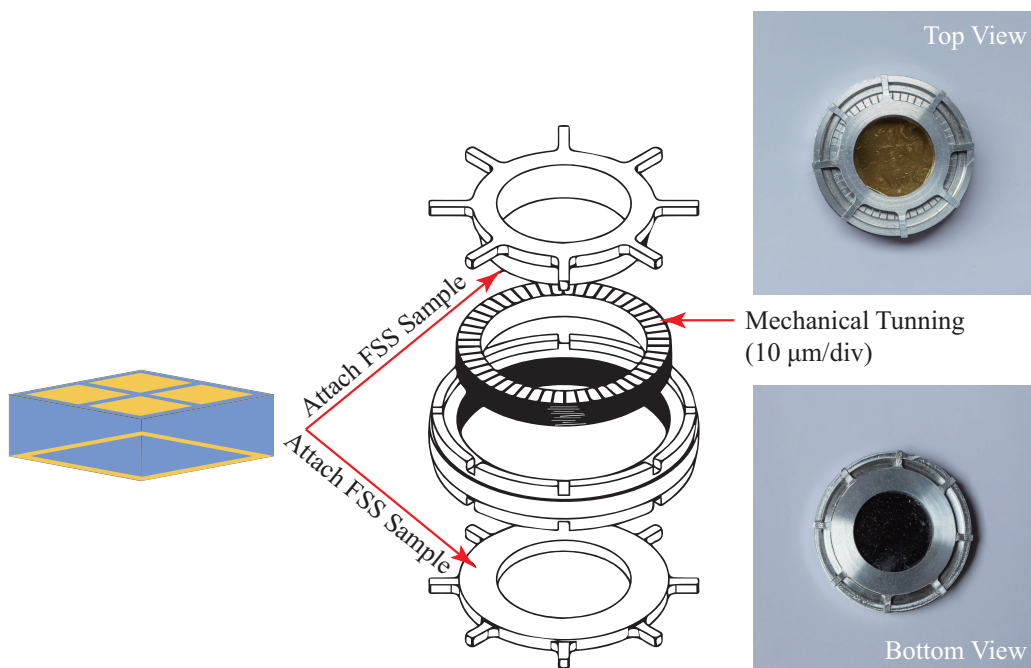


Figure 6.13. Reconfigurable bandpass filter assembly on a mechanically tunable holder. The mechanical holder can be tuned from 50 μm to 500 μm continuously and the resolution is 10 μm per division. The top and bottom views of the filter are also included.

6.5 Experimental Validation

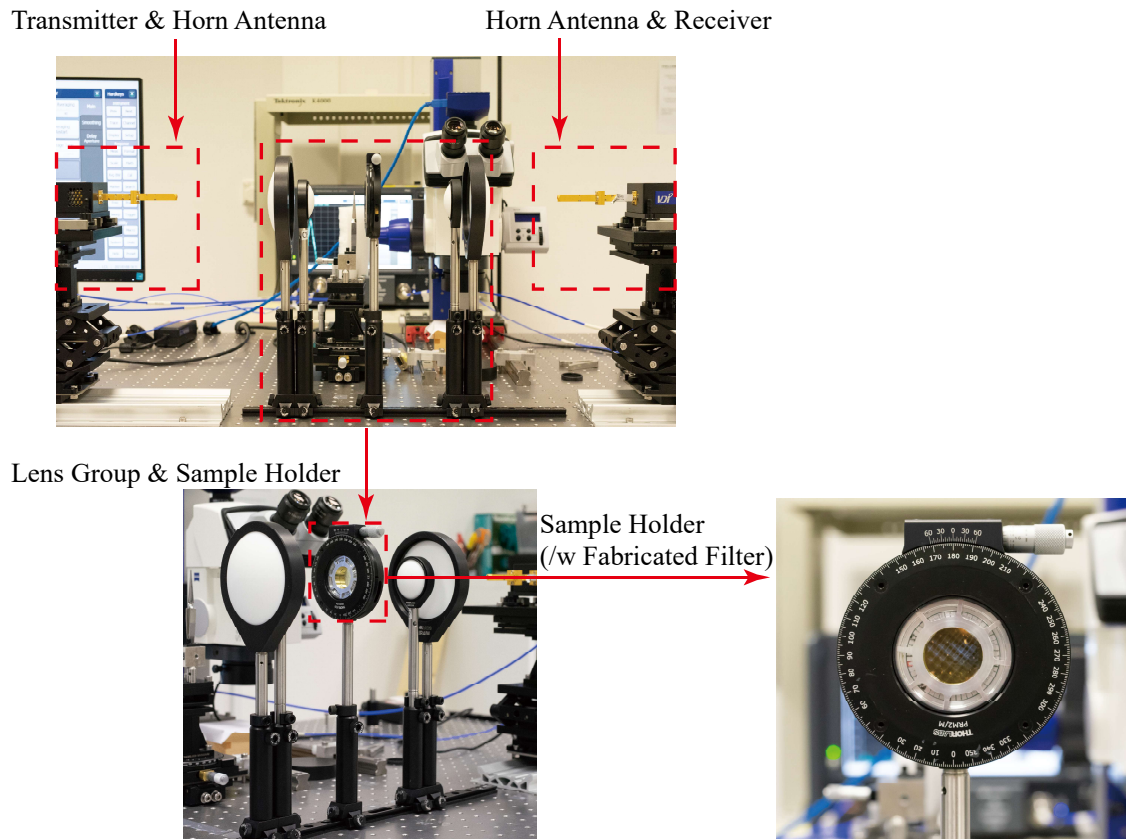


Figure 6.14. Setup for experimental verification of the proposed design. The system works in the frequency range from 220 to 330 GHz.

6.5.2 Equipment Setup and Measurement

The overall setup of the transmission path, as shown in 6.14, includes a vector network analyzer (VNA), two VNA extension modules, transmitting and receiving antennas, and guiding optics. This figure is for illustrating the equipment setup only, which was not taken during the measurement progress. A well focused beam of 2 mm diameter can be obtained by aligning the horn antennas and focusing lenses with the aid of the graded slide rail. All the measured results are normalized to a transmission with the same setup but with the absence of the sample.

The measured results are shown in 6.15 where the double-layer FSSs are separated from 100 to 300 μm with a 50 μm step. The extra 5 μm COC base, due to the restriction in fabrication technique, has been considered in these simulation results. Overall, the measured results well match the simulations. However slight shifts in frequency can

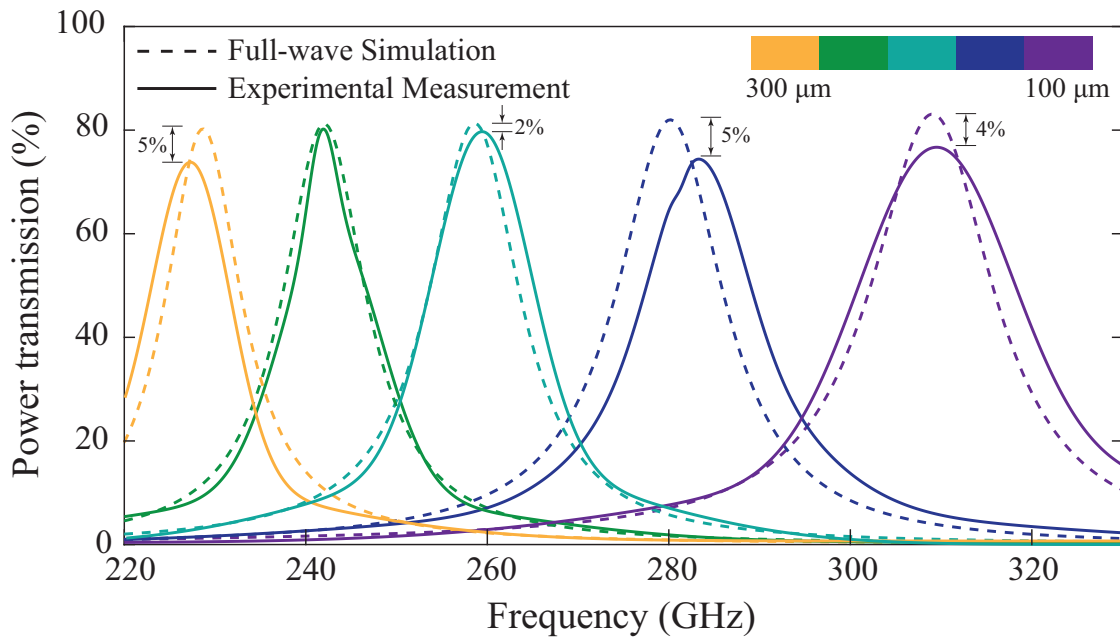


Figure 6.15. Measured power transmission of the proposed reconfigurable bandpass filter.

The mechanical holder is discretely tuned from 100 μm to 300 μm . The measured data are filtered with a time-gating window in the time domain to remove spurious reflections from other optical components.

be observed because of the imperfections of the mechanical tuner. On average, power attenuation from the simulated results is at most 5% of the total incident power, which is mainly caused by the fabrication tolerance in geometric dimensions of the double-layer FSSs. The slightly broadened and attenuated peaks may be also due to the fact that a focused beam is used which has a broader angular spectrum compared to a collimated Gaussian beam [78,79].

A few notable experimentally validated microwave and terahertz reconfigurable filters are listed in Table 6.1 in terms of FSS geometry, tuning mechanism, spectral range, and insertion loss. The proposed design adopts fundamental unit-cell shapes and two identical double-layer FSS without using novel materials such as liquid metal [81]. Its tuning mechanism is mechanical and as such, no bias network is required, which simplifies modeling and implementation. The proposed filter has the widest tuning range, and its insertion loss (IL) is among the lowest, despite its high operation frequencies.

6.6 Conclusion

Table 6.1. Comparison with other frequency reconfigurable filters.

	Geometry	FSS Layers	f_0	Mechanism	Tunability (%)	IL (dB)
[15]	3D Spring	NA	3.5 GHz	Mechanical	17	<1
[43]	Non-Fundamental	3	4.45 GHz	Varactor	34	3-6
[80]	Patch and Grid	5	5.25 GHz	Varactor	10	1.6-7.2
[81]	Patch and Grid	5	10 GHz	Mechanical	32	<1
[42]	Crosses	*	1.25 THz	Mechanical	Discrete	1.4
Proposed	Patch and Grid	4	275 GHz	Mechanical	40	<1

* One layer including 16 different cross FSS samples.

6.6 Conclusion

A multilayer FSS-based reconfigurable bandpass filter has been proposed in this chapter. With high and consistent selectivity, the filter operates in a wide frequency range from 220 to 330 GHz where the power transmission remains at least 80%. This frequency range is equivalent to 40% fractional bandwidth and overlaps with an atmospheric window that allows free-space transmission with low loss.

This design adopts fundamental unit-cell patterns and a pair of identical double-layer FSSs, and thus can be precisely analyzed and synthesized with simple equivalent *RLC* circuit models. From different physical perspectives, namely the multi-path interference and impedance matching, its selectivity and reconfigurability have been explicitly deduced and explained, which in-turn can aid the synthesis. In addition, the robustness against fabrication tolerances and reliability under oblique angles of incidence has been verified by full-wave simulations. The filter is capable of maintaining the full-band reconfigurability up to 45° angle of incidence.

The experimentally validated power transmission shows a close agreement with the simulated results regarding selectivity, tuning range and power efficiency. Compared to the state-of-the-art designs in the literature, this work demonstrates the widest frequency reconfigurable range of 40% and the lowest insertion loss at less than 1 dB. The proposed design can be implemented for multi-band high-quality terahertz telecommunications.

Chapter 7

Summary and Outlook

THE research work presented in this thesis has been divided into two major parts based on the operation frequencies. The first part has focused on design methods for CA absorber in the microwave spectrum. Without exploring complicated FSS shapes, the bandwidth-to-thickness ratio of an absorber can be enhanced either by adding a proper impedance matching superstrate or by exhaustively exploiting a fundamental topology optimized with a semi-analytical algorithm. The second part has firstly demonstrated a realistic approach to controlling surface resistance for broadband absorbers in the terahertz spectrum, then has illustrated and validated a reconfigurable filter design adopting lossless FSSs. This chapter concludes the thesis and suggests possible future research topics.

7.1 Circuit Analog Microwave Absorbers

7.1.1 Chapter 3: Absorber Adopting Impedance Matching Superstrate

Background: For planar absorbers, the trade-off between relative bandwidth and normalized thickness at a specified level of reflectivity is mathematically explained by Rozanov's criterion. In contrast to classic designs such as Jaumann layers, FSS-based circuit analog (CA) absorbers can achieve improved absorption performance without increasing their thickness profile. To further approach the theoretically maximal bandwidth-to-thickness ratio, CA absorbers featured with a variety of complicated unit-cell patterns have been reported in the literature. The supporting dielectrics are indispensable components for CA absorbers, however, their exploitation for optimized designs has been neglected in the literature.

Methodology: From the energy conservation perspective, the absorption performance can be improved if the reflection is suppressed. The design problem hereby becomes the impedance matching to free space. A dielectric superstrate can be regarded as a transformer which is among the simplest impedance matching techniques in the transmission line (TL) theory. A fundamental square-patch FSS is also adopted for simplicity in analysis and synthesis. The Smith chart can be used as a visualization tool that aids the choices of substrate and superstrate.

Results: The experimentally validated single-FSS-layer absorber obtains a relative bandwidth of 1:5.32 at -10 dB level of reflectivity. Defined by the ratio of theoretical minimal thickness to the realized thickness for such absorption performance, its figure of merit (FoM) of 88.26% is superior to the existing designs based on more complicated FSS shapes [22].

Original Contribution: It is firstly demonstrated with circuit models and then verified in the full-wave simulations that bandwidth enhancement and thickness reduction can be simultaneously achieved with a proper impedance transformer. The optimal permittivity and thickness for the superstrate can be systematically obtained from the Smith chart. To maximize the relative bandwidth, it is also proven that an air spacer is the best choice for the substrate.

Future Work: In principle, it can be expected that the dielectric superstrate would be able to improve the bandwidth-to-thickness ratio of existing CA absorbers adopting

any FSS patterns. It should be noted that, however, the equivalent capacitors of the FSS will be affected by the superstrate, thus the absorber structure must always be optimized as a whole. The Smith chart is a qualitative tool with limited accuracy in practice. Therefore, a series of quantitative expressions would be preferable for choosing dielectrics. Moreover, according to Munk [25], a dielectric cover could also be beneficial to absorption stability under oblique incident waves. It would be of interest to further investigate if the superstrate can also contribute to the stability under oblique incidence.

7.1.2 Chapter 4: Design Approach for Circuit-Analog Absorbers

Background: To obtain a broad operation bandwidth, the majority of CA absorber designs focus on exploration of FSS shapes with multiple resonances. However, with larger degrees of freedom (DoF) in the unit-cell geometry, their optimization rapidly become computationally prohibitive. Although there exist a number of analytical formulas adapted from microstrip lines for a few specific FSS shapes, these expressions are sophisticated and generally not sufficiently accurate. Before evolving a fundamental FSS shape into a complex one with more design variables, it is important to ensure that the potential of the existing topology has already been fully exhausted. In addition, when comparing a thin absorber of narrow bandwidth to a thicker wideband design, the FoMs must be calculated based on Rozanov's theory.

Methodology: A CA absorber is investigated with regard to its unit-cell geometry, lossless supporting dielectrics and sheet resistance. Regression functions for each part can be individually developed by matching the Z -parameters of the equivalent circuit calculations to the full-wave simulations, and then combined as a whole based on linearity, scalability and independence. The versatility of this design method is verified by evolving the existing fundamental FSS shape (square patch) with an additional DoF (square ring).

Results: For polarization-independent absorption at 10 dB level, the fabricated CA absorber based on square rings achieves a relative bandwidth of 144.15% despite of its structural simplicity [32]. Such absorption performance is insensitive to oblique incidence up to 50 degrees for both TE and TM modes. It is illustrated that the proposed design outperforms other single-FSS-layer absorbers in the open literature.

7.2 FSS-Based Structures for Terahertz Applications

Original Contribution: An efficient and effective optimization approach for CA absorbers has been developed by systematically integrating analytical, empirical and numerical techniques. With the obtained semi-analytical algorithm, the number of full-wave simulations required for a near global optimum can be dramatically reduced from millions to a few hundreds. On such basis, an absorber topology can be configured for any specified absorption performance within a feasible range, which allows a direct comparison to the state-of-the-art designs. It also suggests that more complicated and calculation-intensive unit-cell geometry may not necessarily guarantees improved larger bandwidth-to-thickness ratio.

Future Work: According to a series of optimized designs aiming for 10 dB absorption with bandwidth ranging from 50% to 150%, the material attributes, including relative permittivities of the supporting dielectrics and surface resistances of the FSS, are conjectured to be monotone functions regardless of the unit-cell patterns. The design parameters may be tabulated to indicate the proper choice of materials for specified absorption performance so that the DoF can be further significantly lowered. Similar to a square ring, a cross is another fundamental FSS shape which can be regarded as an evolved square patch with corners cropped. It would be of interest to compare these two FSS shapes and clarify the differences in the achievable performance.

7.2 FSS-Based Structures for Terahertz Applications

7.2.1 Chapter 5: Terahertz Absorbers with Sub-Skin-Depth Metal

Background: Electromagnetic (EM) absorbers also find wide applications in the terahertz frequency range. The patterned resistive sheets are essential for the CA absorber designs, where the EM power is effectively converted into heat. However, microfabrication technologies applied for THz devices do not well accommodate the commonly used resistive inks for silk-printing lossy FSS patterns, whilst the frequency-dependent material attributes such as conductivity can be significantly different from their values in the microwave range.

Methodology: In terahertz applications, accurate fabrication for of planar metallic structures is mature. Therefore, as an alternative resistive sheet, a piece of noble metal in sub-skin-depth thickness can be used. Based on the frequency-dependent conductivity described by the Drude model, surface resistance can be manipulated by controlling the thickness of metal deposition. To obtain practically large enough equivalent

lumped resistance, noble metals of relatively low conductivity (e.g., titanium, lead, etc.) and FSS shapes with narrow conductive area (e.g., square ring, cross, etc.) are preferable.

Results: At 10 dB level of absorption, the operation spectrum ranges from 165 to 460 GHz which is equivalent to a relative bandwidth of 94% approximately [33]. The proposed absorber is robust to fabrication tolerance and attains a stable absorption performance under oblique impinging waves up to 40 degrees.

Original Contribution: Instead of exploring complicated unit-cell geometries or seeking novel materials, the proposed CA absorber creatively adopts metallic square ring FSS in sub-skin-depth, which satisfies the readily available microfabrication techniques.

Future Work: The first few fabricated samples have been measured, but however, their absorption performances do not closely match the simulated results. The issue is likely related to calibration of metallic deposition for desired sub-skin depth or because of the parameters for the Drude model adopted from the literature that is different from the actual metal in use. In order to bridge the gap between simulation and measurement, a series of homogeneous metal surfaces in different nominated thicknesses can be firstly fabricated. Then, their surface resistances can be deduced based on the measured *S*-parameters. Thus, the relationship between sub-skin-depth metal thickness and surface resistance can be established. The CA absorber can be designed on such basis assuming that these metallic sheets can be accurately reproduced.

7.2.2 Chapter 6: Mechanically Reconfigurable Terahertz Bandpass Filter

Background: FSS-based spatial filters are commonly seen in communications devices. In particular, reconfigurable designs are highly desirable since they may simultaneously achieve high selectivity and wide frequency tuning range. However, for terahertz applications, micro-fabricated varactors incur very high dissipation due to a small PN-junction cross section required by a small capacitance. Even with the aid of novel materials, practical reconfigurable terahertz filters are rarely reported in the literature.

Methodology: A pair of identical double-layer FSSs separated by an air spacer can be regarded as a variant of Fabry-Perot cavity. The power transmission at a specific frequency can be maximized if multiple superposed reflected waves cancel out. This operation frequency can be shifted by changing the spacing in-between these FSSs,

7.3 Concluding Remark

whilst the finesses depends on the transmission coefficient of each double-layer FSS. The underlying mechanism for selectivity and reconfigurability can be intuitively illustrated with an admittance Smith chart which effectively facilitates the optimization.

Results: The proposed reconfigurable filter demonstrates a highly selective and consistent bandpass performance over a broad frequency range. The targeted tuning spectrum can be maintained under oblique impinging waves up to 45 degrees. It has been experimentally verified from 220 to 330 GHz that the power transmission remains above 75%. In comparison to the existing frequency reconfigurable filters, this design achieves the widest operation spectrum and the lowest insertion loss.

Original Contribution: This design is among the first few tunable free-space terahertz bandpass filters reported in the open literature. Two design approaches from analytical and graphical aspects are explicitly demonstrated in parallel for analysis and synthesis.

Future Work: If the proposed design is rescaled for microwave applications, the level of transmission is expected to be higher because the metallic FSSs will be less lossy. Furthermore, when combined with varactors, the tuning range of this prototype may be broadened. It should also be noted that the periodicity for the square patch and grid FSSs are in a ratio of 1:2, which allows more flexibility in synthesizing the equivalent circuit elements. Indeed, the ratio does not necessarily need to be an integer. Although the modeling in a full-wave simulator becomes difficult, the S -parameters can be precisely calculated with the previously obtained semi-analytical functions. With this additional flexibility, the tuning range and selectivity could be improved.

7.3 Concluding Remark

Although FSS-based structures can be analyzed and synthesized with the aid of equivalent circuit models, a number of challenges still exist. Firstly, it is often impossible to explore a complicated unit-cell pattern in a broad spectrum with a simple RLC circuit. In addition, explicitly modeling all the geometric features will elevate the computation cost dramatically for global optimization. Secondly, the FSS shape must be fourfold symmetric to obtain polarization insensitivity, however this also leads to interdependence among equivalent circuit elements. For example, increasing the gap width of a square patch FSS will reduce the equivalent capacitance whilst simultaneously increasing the equivalent inductance. Thus, optimal circuit parameters for a desired frequency response may not be fully realizable. Thirdly, the Floquet ports in the full-wave

simulators limit the ratio of periodicities for multiple FSS layers to rational numbers. Therefore, versatility in synthesizing equivalent circuit elements is restricted. Fourthly, the physical mechanisms for equivalent capacitance or inductance in FSSs differ from those in microstrip lines, as the electromagnetic wave is perpendicularly transmitted through the FSS rather than being guided along it. With regard to the same geometric shapes, the empirical formulas adapted from the microstrip line have been verified to be not sufficiently accurate for FSSs in general. Lastly, the dielectric spacers will have an impact on the equivalent circuit components for FSSs and react differently depending on the angle of oblique incidence for TE and TM modes.

All the above research challenges are crucial and fundamental but not yet fully resolved in the open literature. Furthermore, the built-in optimization tools in the full-wave simulators do not always converge to a global optimum. In contrast, efficiency and reliability of the classic techniques, such as the Smith chart, remain valuable and verified tools for wideband designs.

Besides stealth and interference mitigation, specific industrial applications of wideband planar absorbers need be explored. For example, they can be adapted in compact RF circuit to improve electromagnetic compatibility [18]. The reconfigurable bandpass filter can be modified for high resolution micro-imaging [34] in addition to short range terahertz communications as mentioned.

Bibliography

- [1] B. A. Munk, *Frequency Selective Surfaces: Theory and Design*. John Wiley & Sons, 2000.
- [2] A. Fallahi, M. Mishrikey, C. Hafner, and R. Vahldieck, "Efficient procedures for the optimization of frequency selective surfaces," *IEEE Transactions on Antennas and Propagation*, vol. 56, no. 5, pp. 1340–1349, 2008.
- [3] S. Monni, A. Neto, G. Gerini, F. Nennie, and A. Tijhuis, "Frequency-selective surface to prevent interference between radar and satcom antennas," *IEEE Antennas and Wireless Propagation Letters*, vol. 8, pp. 220–223, 2009.
- [4] L. Li, Q. Chen, Q. Yuan, K. Sawaya, T. Maruyama, T. Furuno, and S. Uebayashi, "Frequency selective reflectarray using crossed-dipole elements with square loops for wireless communication applications," *IEEE Transactions on Antennas and Propagation*, vol. 59, no. 1, pp. 89–99, 2011.
- [5] Y. Ranga, L. Matekovits, K. P. Esselle, and A. R. Weily, "Multioctave frequency selective surface reflector for ultrawideband antennas," *IEEE Antennas and Wireless Propagation Letters*, vol. 10, pp. 219–222, 2011.
- [6] Y. Shang, Z. Shen, and S. Xiao, "Frequency-selective absorber based on square-loop and cross-dipole arrays," *IEEE Transactions on Antennas and Propagation*, vol. 62, no. 11, pp. 5581–5589, 2014.
- [7] S. Jain, A. Yadav, and R. P. Yadav, "Designing of dual band miniaturized frequency selective surfaces for WiMAX/WLAN band," in *2017 International Conference on Wireless Communications, Signal Processing and Networking (WiSPNET)*, 2017, pp. 1473–1477.
- [8] J. Lee, M. Yoo, and S. Lim, "A study of ultra-thin single layer frequency selective surface microwave absorbers with three different bandwidths using double resonance," *IEEE Transactions on Antennas and Propagation*, vol. 63, no. 1, pp. 221–230, 2015.
- [9] M. Yoo and S. Lim, "Polarization-independent and ultrawideband metamaterial absorber using a hexagonal artificial impedance surface and a resistor-capacitor layer," *IEEE Transactions on Antennas and Propagation*, vol. 62, no. 5, pp. 2652–2658, 2014.
- [10] A. H. Panaretos, D. E. Brocker, and D. H. Werner, "Ultra-thin absorbers comprised by cascaded high-impedance and frequency selective surfaces," *IEEE Antennas and Wireless Propagation Letters*, vol. 14, pp. 1089–1092, 2015.
- [11] M. Zhao, X. Yu, Q. Wang, P. Kong, Y. He, L. Miao, and J. Jiang, "Novel absorber based on pixelated frequency selective surface using estimation of distribution algorithm," *IEEE Antennas and Wireless Propagation Letters*, vol. 14, pp. 1467–1470, 2015.
- [12] L. Sun and C. Zhang, "Design of broadband microwave absorber utilizing FSS screen constructed with coupling configurations," *Applied Physics A*, vol. 109, no. 4, pp. 873–875, 2012.

- [13] J. H. Barton, C. R. Garcia, E. A. Berry, R. Salas, and R. C. Rumpf, "3-D printed all-dielectric frequency selective surface with large bandwidth and field of view," *IEEE Transactions on Antennas and Propagation*, vol. 63, no. 3, pp. 1032–1039, 2015.
- [14] B. Li and Z. Shen, "Wideband 3D frequency selective absorber," *IEEE Transactions on Antennas and Propagation*, vol. 62, no. 12, pp. 6536–6541, 2014.
- [15] S. N. Azemi, K. Ghorbani, and W. S. T. Rowe, "A reconfigurable FSS using a spring resonator element," *IEEE Antennas and Wireless Propagation Letters*, vol. 12, pp. 781–784, 2013.
- [16] B. Sanz-Izquierdo and E. A. Parker, "Dual polarized reconfigurable frequency selective surfaces," *IEEE Transactions on Antennas and Propagation*, vol. 62, no. 2, pp. 764–771, 2014.
- [17] A. R. Weily, T. S. Bird, and Y. J. Guo, "A reconfigurable high-gain partially reflecting surface antenna," *IEEE Transactions on Antennas and Propagation*, vol. 56, no. 11, pp. 3382–3390, 2008.
- [18] F. Costa, S. Genovesi, and A. Monorchio, "A chipless RFID based on multiresonant high-impedance surfaces," *IEEE Transactions on Microwave Theory and Techniques*, vol. 61, no. 1, pp. 146–153, 2013.
- [19] S. Keyrouz, G. Perotto, and H. J. Visser, "Frequency selective surface for radio frequency energy harvesting applications," *IET Microwaves, Antennas Propagation*, vol. 8, no. 7, pp. 523–531, 2014.
- [20] B. A. Munk, *Finite Antenna Arrays and FSS*. John Wiley & Sons, 2003.
- [21] F. Costa, A. Monorchio, and G. Manara, "Analysis and design of ultra thin electromagnetic absorbers comprising resistively loaded high impedance surfaces," *IEEE Transactions on Antennas and Propagation*, vol. 58, no. 5, pp. 1551–1558, 2010.
- [22] X. Lv, W. Withayachumnankul, and C. Fumeaux, "Single-FSS-layer absorber with improved bandwidth-thickness tradeoff adopting impedance-matching superstrate," *IEEE Antennas and Wireless Propagation Letters*, vol. 18, no. 5, pp. 916–920, 2019.
- [23] D. Pozar, *Microwave Engineering, 4th Edition*. Wiley, 2011.
- [24] R. Panwar, S. Puthucheri, V. Agarwala, and D. Singh, "Fractal frequency-selective surface embedded thin broadband microwave absorber coatings using heterogeneous composites," *IEEE Transactions on Microwave Theory and Techniques*, vol. 63, pp. 2438–2448, 2015.
- [25] B. A. Munk, P. Munk, and J. Pryor, "On designing Jaumann and circuit analog absorbers (CA absorbers) for oblique angle of incidence," *IEEE Transactions on Antennas and Propagation*, vol. 55, no. 1, pp. 186–193, 2007.
- [26] Y. Shang, Z. Shen, and S. Xiao, "On the design of single-layer circuit analog absorber using double-square-loop array," *IEEE Transactions on Antennas and Propagation*, vol. 61, no. 12, pp. 6022–6029, 2013.
- [27] O. Luukkonen, C. Simovski, G. Granet, G. Goussetis, D. Lioubtchenko, A. V. Raisanen, and S. A. Tretyakov, "Simple and accurate analytical model of planar grids and high-impedance surfaces comprising metal strips or patches," *IEEE Transactions on Antennas and Propagation*, vol. 56, no. 6, pp. 1624–1632, 2008.

-
- [28] R. J. Langley and E. A. Parker, "Equivalent circuit model for arrays of square loops," *Electronics Letters*, vol. 18, no. 7, pp. 294–296, 1982.
- [29] R. Mittra, C. H. Chan, and T. Cwik, "Techniques for analyzing frequency selective surfaces: a review," *Proceedings of the IEEE*, vol. 76, no. 12, pp. 1593–1615, 1988.
- [30] R. T. Ako, A. Upadhyay, W. Withayachumnankul, M. Bhaskaran, and S. Sriram, "Dielectrics for terahertz metasurfaces: Material selection and fabrication techniques," *Advanced Optical Materials*, vol. 8, no. 3, p. 1900750, 2020.
- [31] K. N. Rozanov, "Ultimate thickness to bandwidth ratio of radar absorbers," *IEEE Transactions on Antennas and Propagation*, vol. 48, no. 8, pp. 1230–1234, 2000.
- [32] X. Lv, S. J. Chen, A. Galehdar, W. Withayachumnankul, and C. Fumeaux, "Fast semi-analytical design for single-fss-layer circuit-analog absorbers," *IEEE Open Journal of Antennas and Propagation*, vol. 1, pp. 483–492, 2020.
- [33] X. Lv, W. Withayachumnankul, and C. Fumeaux, "Terahertz absorber design adopting metallic fss in sub-skin-depth thickness," in *2019 IEEE Asia-Pacific Microwave Conference (APMC)*, 2019, pp. 628–630.
- [34] V. Sanphuang, N. Ghalichechian, N. K. Nahar, and J. L. Volakis, "Reconfigurable THz filters using phase-change material and integrated heater," *IEEE Transactions on Terahertz Science and Technology*, vol. 6, no. 4, pp. 583–591, 2016.
- [35] M. Olszewska-Placha, B. Salski, D. Janczak, P. R. Bajurko, W. Gwarek, and M. Jakubowska, "A broadband absorber with a resistive pattern made of ink with graphene nano-platelets," *IEEE Transactions on Antennas and Propagation*, vol. 63, no. 2, pp. 565–572, 2015.
- [36] A. Kazemzadeh and A. Karlsson, "Multilayered wideband absorbers for oblique angle of incidence," *IEEE Transactions on Antennas and Propagation*, vol. 58, no. 11, pp. 3637–3646, 2010.
- [37] D. Kundu, A. Mohan, and A. Chakrabarty, "Single-layer wideband microwave absorber using array of crossed dipoles," *IEEE Antennas and Wireless Propagation Letters*, vol. 15, pp. 1589–1592, 2016.
- [38] J. Yang and Z. Shen, "A thin and broadband absorber using double-square loops," *IEEE Antennas and Wireless Propagation Letters*, vol. 6, pp. 388–391, 2007.
- [39] M. Yoo, H. K. Kim, S. Kim, M. Tentzeris, and S. Lim, "Silver nanoparticle-based inkjet-printed metamaterial absorber on flexible paper," *IEEE Antennas and Wireless Propagation Letters*, vol. 14, pp. 1718–1721, 2015.
- [40] Y. Álvarez, M. E. de Cos, and F. Las-Heras, "RCS measurement setup for periodic-structure prototype characterization," *IEEE Antennas and Propagation Magazine*, vol. 52, no. 3, pp. 100–106, 2010.
- [41] H. F. Alvarez, M. E. de Cos Gomez, and F. Las-Heras, "Angular stability of metasurfaces: Challenges regarding reflectivity measurements [measurements corner]," *IEEE Antennas and Propagation Magazine*, vol. 58, no. 5, pp. 74–81, 2016.
- [42] D. Zhai, Y. Yang, Z. Geng, B. Cui, and R. Zhao, "A high-selectivity THz filter based on a flexible polyimide film," *IEEE Transactions on Terahertz Science and Technology*, vol. 8, no. 6, pp. 719–724, 2018.

- [43] A. Ebrahimi, Z. Shen, W. Withayachumnankul, S. F. Al-Sarawi, and D. Abbott, "Varactor-tunable second-order bandpass frequency-selective surface with embedded bias network," *IEEE Transactions on Antennas and Propagation*, vol. 64, no. 5, pp. 1672–1680, 2016.
- [44] A. Kazemzadeh, "Nonmagnetic ultrawideband absorber with optimal thickness," *IEEE Transactions on Antennas and Propagation*, vol. 59, no. 1, pp. 135–140, 2011.
- [45] R. Panwar, V. Agarwala, and D. Singh, "A cost effective solution for development of broadband radar absorbing material using electronic waste," *Ceramics International*, vol. 41, no. 2, Part B, pp. 2923–2930, 2015.
- [46] J. Chen, Y. Shang, and C. Liao, "Double-layer circuit analog absorbers based on resistor-loaded square-loop arrays," *IEEE Antennas and Wireless Propagation Letters*, vol. 17, no. 4, pp. 591–595, 2018.
- [47] Y. Han, W. Che, C. Christopoulos, Y. Xiong, and Y. Chang, "A fast and efficient design method for circuit analog absorbers consisting of resistive square-loop arrays," *IEEE Transactions on Electromagnetic Compatibility*, vol. 58, no. 3, pp. 747–757, 2016.
- [48] D. Yi, X. C. Wei, and Y. L. Xu, "Transparent microwave absorber based on patterned graphene: Design, measurement, and enhancement," *IEEE Transactions on Nanotechnology*, vol. 16, no. 3, pp. 484–490, 2017.
- [49] H.-T. Chen, "Interference theory of metamaterial perfect absorbers," *Optics Express*, vol. 20, no. 7, pp. 7165–7172, 2012.
- [50] A. J. Chipperfield and P. J. Fleming, "The matlab genetic algorithm toolbox," in *IEE Colloquium on Applied Control Techniques Using MATLAB*, 1995, pp. 10/1–10/4.
- [51] Q. Chen, J. Bai, L. Chen, and Y. Fu, "A miniaturized absorptive frequency selective surface," *IEEE Antennas and Wireless Propagation Letters*, vol. 14, pp. 80–83, 2015.
- [52] H. B. Zhang, P. H. Zhou, H. P. Lu, Y. Q. Xu, D. F. Liang, and L. J. Deng, "Resistance selection of high impedance surface absorbers for perfect and broadband absorption," *IEEE Transactions on Antennas and Propagation*, vol. 61, no. 2, pp. 976–979, 2013.
- [53] J. Wu, Y. Qi, W. Yu, L. Liu, and F. Li, "An absorber-integrated taper slot antenna," *IEEE Transactions on Electromagnetic Compatibility*, vol. 59, no. 6, pp. 1741–1747, 2017.
- [54] S. Piersanti, F. de Paulis, A. Orlandi, S. Connor, Q. Liu, B. Archambeault, P. Dixon, M. Khorrami, and J. L. Drewniak, "Near-field shielding performances of EMI noise suppression absorbers," *IEEE Transactions on Electromagnetic Compatibility*, vol. 59, no. 2, pp. 654–661, 2017.
- [55] F. Costa, S. Genovesi, A. Monorchio, and G. Manara, "A circuit-based model for the interpretation of perfect metamaterial absorbers," *IEEE Transactions on Antennas and Propagation*, vol. 61, no. 3, pp. 1201–1209, 2013.
- [56] M. I. Hossain, N. Nguyen-Trong, K. H. Sayidmarie, and A. M. Abbosh, "Equivalent circuit design method for wideband nonmagnetic absorbers at low microwave frequencies," *IEEE Transactions on Antennas and Propagation*, vol. 68, no. 12, pp. 8215–8220, 2020.

-
- [57] J. W. Bandler, Q. S. Cheng, S. A. Dakroury, A. S. Mohamed, M. H. Bakr, K. Madsen, and J. Sondergaard, "Space mapping: the state of the art," *IEEE Transactions on Microwave Theory and Techniques*, vol. 52, no. 1, pp. 337–361, 2004.
- [58] S. Koziel, Q. S. Cheng, and J. W. Bandler, "Space mapping," *IEEE Microwave Magazine*, vol. 9, no. 6, pp. 105–122, 2008.
- [59] B. Wang, L. Wang, G. Wang, W. Huang, X. Li, and X. Zhai, "Theoretical investigation of broadband and wide-angle terahertz metamaterial absorber," *IEEE Photonics Technology Letters*, vol. 26, no. 2, pp. 111–114, 2014.
- [60] A. Fardoost, F. G. Vanani, A. Amirhosseini, and R. Safian, "Design of a multilayer graphene-based ultrawideband terahertz absorber," *IEEE Transactions on Nanotechnology*, vol. 16, no. 1, pp. 68–74, 2017.
- [61] Z. Song, K. Wang, J. Li, and Q. H. Liu, "Broadband tunable terahertz absorber based on vanadium dioxide metamaterials," *Opt. Express*, vol. 26, no. 6, pp. 7148–7154, 2018.
- [62] A. Andryieuski and A. V. Lavrinenko, "Graphene metamaterials based tunable terahertz absorber: effective surface conductivity approach," *Opt. Express*, vol. 21, no. 7, pp. 9144–9155, 2013.
- [63] J. Min Woo, M.-S. Kim, H. Woong Kim, and J.-H. Jang, "Graphene based salisbury screen for terahertz absorber," *Applied Physics Letters*, vol. 104, no. 8, p. 081106, 2014.
- [64] C. Shi, X. Zang, Y. Wang, L. Chen, B. Cai, and Y. Zhu, "A polarization-independent broadband terahertz absorber," *Applied Physics Letters*, vol. 105, no. 3, p. 031104, 2014.
- [65] L. Zou, W. Withayachumnankul, C. M. Shah, A. Mitchell, M. Klemm, M. Bhaskaran, S. Sriram, and C. Fumeaux, "Efficiency and scalability of dielectric resonator antennas at optical frequencies," *IEEE Photonics Journal*, vol. 6, no. 4, pp. 1–10, 2014.
- [66] R. Singh, E. Smirnova, A. J. Taylor, J. F. O'Hara, and W. Zhang, "Optically thin terahertz metamaterials," *Opt. Express*, vol. 16, no. 9, pp. 6537–6543, 2008.
- [67] A. Ebrahimi, T. Baum, J. Scott, and K. Ghorbani, "Narrowband bandpass frequency selective surface with miniaturized elements," in *2017 IEEE Asia Pacific Microwave Conference (APMC)*, 2017, pp. 196–199.
- [68] "IEEE standard for high data rate wireless multi-media networks—amendment 2: 100 gb/s wireless switched point-to-point physical layer," *IEEE Std 802.15.3d-2017 (Amendment to IEEE Std 802.15.3-2016 as amended by IEEE Std 802.15.3e-2017)*, pp. 1–55, 2017.
- [69] M. Hussein, J. Zhou, Y. Huang, and B. Al-Juboori, "A low-profile miniaturized second-order bandpass frequency selective surface," *IEEE Antennas and Wireless Propagation Letters*, vol. 16, pp. 2791–2794, 2017.
- [70] P. Zhao, Z. Zong, W. Wu, B. Li, and D. Fang, "Miniaturized-element bandpass fss by loading capacitive structures," *IEEE Transactions on Antennas and Propagation*, vol. 67, no. 5, pp. 3539–3544, 2019.

-
- [71] B. Li, X. Huang, L. Zhu, Y. Zhang, Y. Tang, W. Lu, and Y. Bo, "Bandpass frequency selective structure with improved out-of-band rejection using stacked single-layer slotlines," *IEEE Transactions on Antennas and Propagation*, vol. 66, no. 11, pp. 6003–6014, 2018.
- [72] N. Behdad, M. Al-Joumayly, and M. Salehi, "A low-profile third-order bandpass frequency selective surface," *IEEE Transactions on Antennas and Propagation*, vol. 57, no. 2, pp. 460–466, 2009.
- [73] F. Bayatpur and K. Sarabandi, "Design and analysis of a tunable miniaturized-element frequency-selective surface without bias network," *IEEE Transactions on Antennas and Propagation*, vol. 58, no. 4, pp. 1214–1219, 2010.
- [74] —, "A tunable metamaterial frequency-selective surface with variable modes of operation," *IEEE Transactions on Microwave Theory and Techniques*, vol. 57, no. 6, pp. 1433–1438, 2009.
- [75] M. Taha, S. Walia, T. Ahmed, D. Headland, W. Withayachumnankul, S. Sriram, and M. Bhaskaran, "Insulator–metal transition in substrate-independent vo2 thin film for phase-change devices," *Scientific Reports*, vol. 7, no. 17899, 2017.
- [76] M. J. Dicken, K. Aydin, I. M. Pryce, L. A. Sweatlock, E. M. Boyd, S. Walavalkar, J. Ma, and H. A. Atwater, "Frequency tunable near-infrared metamaterials based on vo2 phase transition," *Opt. Express*, vol. 17, no. 20, pp. 18 330–18 339, 2009.
- [77] M. Born, E. Wolf, A. B. Bhatia, P. C. Clemmow, D. Gabor, A. R. Stokes, A. M. Taylor, P. A. Wayman, and W. L. Wilcock, *Principles of Optics: Electromagnetic Theory of Propagation, Interference and Diffraction of Light*, 7th ed. Cambridge University Press, 1999.
- [78] S. Freer, M. Camacho, S. A. Kuznetsov, R. R. Boix, M. Beruete, and M. Navarro-Cía, "Revealing the underlying mechanisms behind TE extraordinary THz transmission," *Photon. Res.*, vol. 8, no. 4, pp. 430–439, 2020.
- [79] M. Navarro-Cía, V. Pacheco-Peña, S. A. Kuznetsov, and M. Beruete, "Extraordinary THz transmission with a small beam spot: The leaky wave mechanism," *Advanced Optical Materials*, vol. 6, no. 8, p. 1701312, 2018.
- [80] W. Pan, C. Huang, P. Chen, M. Pu, X. Ma, and X. Luo, "A beam steering horn antenna using active frequency selective surface," *IEEE Transactions on Antennas and Propagation*, vol. 61, no. 12, pp. 6218–6223, 2013.
- [81] M. Li and N. Behdad, "Fluidically tunable frequency selective/phase shifting surfaces for high-power microwave applications," *IEEE Transactions on Antennas and Propagation*, vol. 60, no. 6, pp. 2748–2759, 2012.